Structure of the Virtual Photon at HERA

Neil Scott Macdonald

Department of Physics & Astronomy
University of Glasgow
Glasgow

Thesis submitted for the degree of
Doctor of Philosophy

November 1999

Abstract

The dependence of the structure of the photon on its virtuality, Q^2, and on the scale of the probing jets, is investigated by measuring the reaction $e^+p \rightarrow e^+ + jet + jet + X$ with the ZEUS detector at HERA. Samples of such events ranging from $Q^2 \approx 0$ GeV^2 to Q^2 of 5000 GeV^2 have been selected from the data taken in 1996 and 1997, corresponding to an integrated luminosity of 38.1 pb^{-1}. The measured inclusive differential dijet cross section $d\sigma/dx_\gamma^{obs}$ is presented as a function of Q^2 and the square of the transverse energy of the jets, E_T^2, where x_γ^{obs} is an estimator of the fraction of the photon's momentum participating in the hard dijet subprocess, and compared with the predictions of leading order Monte Carlo programs for various photon parton distribution functions. The ratio of dijet cross sections with $x_\gamma^{obs} < 0.75$ to $x_\gamma^{obs} > 0.75$ show the number of events exhibiting resolved photonic structure to decrease relative to those events without such structure as the photon virtuality increases, whilst the dependence on the scale of the probing jets is small. In comparing simulated Monte Carlo events with the data, it is found that events which simulate photonic structure are needed up to a virtuality of at least 10.5 GeV^2.

To My Parents

Outline

This thesis extends previous analyses to almost the highest photon virtualities accessible with the ZEUS detector, and compares measured data distributions which are sensitive to photon structure with a number of theoretical models.

Chapter 1 introduces the kinematics specific to HERA physics and describes the specific topic of jet physics in photoproduction. Chapter 2 deals with the idea of photon structure and which theoretical models are presently favoured to explain current measurements. Chapter 3 describes the main components of the ZEUS detector and elaborates on those components which are particularly important to this analysis. Chapter 4 explains the data quality monitoring procedure which I was responsible for coordinating during the 1998 data taking periods. During my time as coordinator I revised the whole procedure and modified much of it. More data distribution plots were added and some were combined, streamlining the old procedure and ultimately improving the quality of the data which is later used in physics analyses. Chapter 5 discusses jet finding algorithms and then the data selection cuts to obtain a clean sample of inclusive dijet events. The following chapters describe the procedure I adopted in the analysis of the data, the comparison with theory and the conclusions I drew from those comparisons. Chapters 6 and 7 describe the Monte Carlo event samples which are used to correct the data for detector mismeasurement and the checks performed to cover any systematic mismeasurements. Finally, chapters 8 and 9 compare corrected data distributions with various theoretical predictions. Appendix A contains tables of reweighting factors by which different Monte Carlo samples were reweighted in order to fit the corrected data. For clarity, the corrected data is also presented in tabular form in appendix B.

Acknowledgements

I would like to thank my parents for their support throughout a sum total of seven years of university education. I hope I have made them proud.

I thank my supervisor David Saxon, who has helped to extract this thesis out of me sooner than it might otherwise have arrived. His overview of particle physics in general has been extremely useful to me in writing up.

Costas Foudas deserves my thanks for being my "proxy" supervisor and good friend during my time at DESY. His guidance on the analysis work has been invaluable.

The UK contingent at DESY have been a family away from home, so many good friends, too many to mention all of them here, but special thanks to those in the Glasgow office there - Rob, Gavin, Sung Won, Laurel and Nick, and also back in Glasgow - Esther, Jane, Tony, Peter and Ian, who have made the three years a lot more interesting than I hoped for.

I thank my flat-mates Steve and Craig who have been good friends to me in my final year and have smoothed my transition back into the Scottish way of life.

Last but not least, my thanks goes out to Catherine McIntyre and Susan Ketels for their ever friendly help, despite what their students needed (or got up to) they were always there for us.

Contents

List of Figures

List of Tables

Chapter 1

Introduction

Particle physics is the study of particles and their interactions. Two such forces of interaction were recognised at the turn of the century: gravity and electromagnetism. The electron had just been discovered, and by 1911, Rutherford showed that the atom consisted of a small nucleus surrounded by electrons by scattering alpha particles off a target made of gold. The resultant distribution of scattered alpha particles was indicative of a small, dense object at the centre of the atom, the nucleus. The idea of firing a probe particle to examine the structure of a target particle is still used today to examine structure on a subatomic level and beyond. The spatial resolution which can be obtained in such experiments is limited by the wavelength of the probing particle, $\lambda = h/p$, where p is the momentum of the probe particle and h is Planck's constant. Thus, the higher the momentum of the probing particle, the more substructure that can be resolved in the target particles.

1.1 Particles and their Interactions

There exist three classes of elementary particles: leptons, quarks and gauge bosons. Bosons are characterised by having integral spin quantum numbers, whereas fermions have half-integral spin quantum numbers. Leptons and quarks

have spin $\hbar/2$ and are therefore fermions. The fermions are grouped into three categories or "generations". For leptons, the first generation is a doublet containing the electron and the electron neutrino. The muon and tau leptons, together with their corresponding neutrinos constitute the second and third generations respectively, and can be written as

$$\begin{pmatrix} \nu_e \\ e^- \end{pmatrix} \quad \begin{pmatrix} \nu_\mu \\ \mu^- \end{pmatrix} \quad \begin{pmatrix} \nu_\tau \\ \tau^- \end{pmatrix}$$

The six quarks are grouped together in a similar fashion

$$\begin{pmatrix} u \\ d \end{pmatrix} \quad \begin{pmatrix} c \\ s \end{pmatrix} \quad \begin{pmatrix} t \\ b \end{pmatrix}$$

Each lepton and quark has a corresponding antiparticle, which has the same mass as its partner, but the isospin component, baryon and lepton numbers, charge and parity are equal and opposite in sign.

The leptons and quarks interact with each other via the exchange of gauge bosons, which are the mediators of forces. The forces that are taken into account in particle physics are the electromagnetic, weak and strong forces. The gravitational force is not included, mainly because no quantum theory of gravity exists as yet. However its strength relative to the other three is so small that its effects in particle physics phenomena are negligible. The electromagnetic force is experienced by all particles that carry an electric charge or magnetic moment and is mediated by photon exchange. The weak force is experienced by all the fermions, being mediated by the massive W and Z bosons, and is responsible for such processes as the beta decay of radioactive nuclei. The strong force binds quarks together into hadrons such as neutrons and protons. Its mediator is the massless gluon.

The four-momentum transferred in an interaction, carried by a boson, is denoted by q. It can be shown that it is kinematically impossible for one particle to absorb a massless second particle, due to consideration of energy and

momentum conservation. The exchanged boson must therefore have a non-zero mass. The virtuality of this boson is defined as $Q^2 = -q^2$. The value of Q^2 must be non-zero if the boson is to be absorbed in an interaction. If $Q^2 = M^2$, where M is the rest mass of the boson, the boson is said to be "on-mass-shell". When considering photons, the rest mass is zero. If the photon has a virtuality of zero, it is termed a "real" photon. Otherwise, it is termed "virtual". The strength of a force is proportional to its coupling constant. At a Q^2 much less than the squared mass of the (on-mass-shell) W or Z bosons, the weak force has a small coupling constant, which is much lower than that of the electromagnetic interaction, $\alpha \approx 1/137$. This arises due to the probability of an interaction being inversely proportional to Q^4. At low momentum transfers, $Q^2 \ll M_{weak}^2$, where M_{weak} is the mass of the W or Z bosons, the probability for exchange of a W or Z is small compared to that of the photon. Conversely, for momentum transfers where $Q^2 \approx M_{weak}^2$, the interaction probability of W, Z and photon exchange converge to similar values. The electromagnetic and weak forces are now understood as a unified force, the electroweak force [3].

Quantum electrodynamics (QED) is a theory of electromagnetic interactions. Its results can be calculated within a perturbative framework by virtue of the fact that the electromagnetic coupling constant, α, is much smaller than unity. In QED an electron is constantly emitting and re-absorbing virtual photons, some of which momentarily fluctuate into electron and antielectron (positron) pairs before being reabsorbed. This creates a screening effect, such that at large distances, the electron appears to have a reduced charge. Conversely, at smaller distances, the screening is reduced, and α becomes larger. It is a "running" coupling constant, and to first order (one boson exchange), depends on the Q^2 of the exchanged photon, according to the relation

$$\alpha(Q^2) \approx \frac{\alpha(\mu^2)}{1 - \frac{\alpha(\mu^2)}{3\pi} \log \frac{Q^2}{\mu^2}} \tag{1.1}$$

for $Q^2 >> \mu^2$ where μ is the mass scale at which α is calculated. α rises as Q^2

increases, but for all presently attainable Q^2, α remains small enough that the perturbative approach is valid.

The strong force is mediated by gluons, the quanta of the "colour" field between coloured partons such as quarks. Quantum Chromodynamics (QCD) is a theory of strong interactions. As well as having an electromagnetic charge, strongly interacting particles also have a colour charge. Unlike photons, gluons carry the charge of the field, and this has different implications for the running of the strong coupling constant, α_s, which (to first order) is given by

$$\alpha_s(Q^2) \approx \frac{12\pi}{(33 - 2N_f)\log\frac{Q^2}{\Lambda^2_{QCD}}} \tag{1.2}$$

where N_f denotes the number of active quark flavours and Λ_{QCD} is a fundamental parameter of QCD, the value of which is not predicted but has been determined experimentally to lie in the range 100-300 MeV [10].

This means that $\alpha_s \to 0$ as $Q^2 \to \infty$, a consequence known as "asymptotic freedom" [5]. Partons which are close together act as if no attraction exists between them. Also, $\alpha_s \to \infty$ as $Q^2 \to \Lambda^2_{QCD}$. This means that at small momentum transfers, or large distances, α_s is so large that the attractive force between partons keeps them confined inside hadrons. As $Q^2 \to 0$ the perturbative expansion for α_s, the leading term of which is shown in equation 1.2, breaks down and is no longer applicable. Again, $\alpha_s \to \infty$. This is termed "infrared slavery" [4], and is thought to explain why free quarks have never been observed. As long as Q^2 is much larger than Λ^2_{QCD}, α_s is smaller than unity and QCD results can be calculated perturbatively.

The existence of nucleonic substructure was discovered using an eN deep inelastic scattering experiment in 1969 by the SLAC-MIT group [6]. The experiment found that the structure function of the nucleons, which can be interpreted in terms of the parton density (see chapter 2), was constant with respect to the momentum transfer from electron to nucleon. This observation led to the model that the proton contains fractionally charged pointlike particles,

which are scattered like free particles [7]. These charged pointlike particles were generally accepted to be the quarks, earlier postulated by Gell-Mann [8], and the model became known as the quark parton model (QPM). If the proton consisted solely of charged quarks, their momenta would be expected to add up to the momentum of the proton. Experimentally it is found that these quarks carry approximately only half of the proton's momentum, implying that the other half is carried by neutral partons. These turned out to be the gluons, which were later directly observed via the observation of three-jet events in e^+e^- annihilation experiments [9].

1.2 HERA Kinematics

The Hadron Elektron Ring Anlage (HERA), the first electron-proton (ep) collider, was built mainly for the purpose of examining the structure of the proton and to explore the region $Q^2 \gg M_Z^2$. In the 1996 and 1997 running period, the HERA machine collided protons with positrons. The protons and positrons were accelerated to energies of 820 GeV and 27.5 GeV respectively in counter-rotating beams and then allowed to collide at an interaction point around which a detector is situated. When they scatter they exchange a virtual boson (a photon, Z^0, or $W^{\pm}$ boson) with a four-momentum transfer, q. The centre of mass energy of these interactions is approximately 300 GeV, leading to a resolution of $\sim 10^{-18}$m, about one thousandth the size of the proton. In elastic scattering, to first order, Q^2 is low enough for the boson not to resolve the quarks in the proton and hence the whole proton scatters as one entity. For Q^2 high enough to resolve partons inside the proton, the event is of the deep inelastic scattering type where one of the quarks is scattered (the struck quark), effectively being knocked out of the proton, when later it will fragment and hadronise, as will the two quarks still left in the proton (see figure 1.1). The struck quark produces a collection of hadrons known as the "current jet", and the other two quarks fragment, hadronise and

form what is known as the proton remnant. The kinematics do not depend on whether an electron or a positron is scattered, and so the terms electron and positron are used interchangeably.

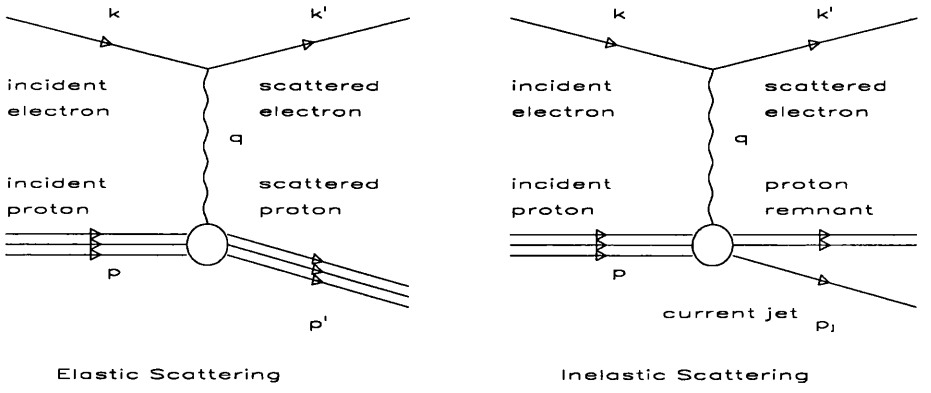

Figure 1.1: Elastic and Deep Inelastic Scattering diagrams.

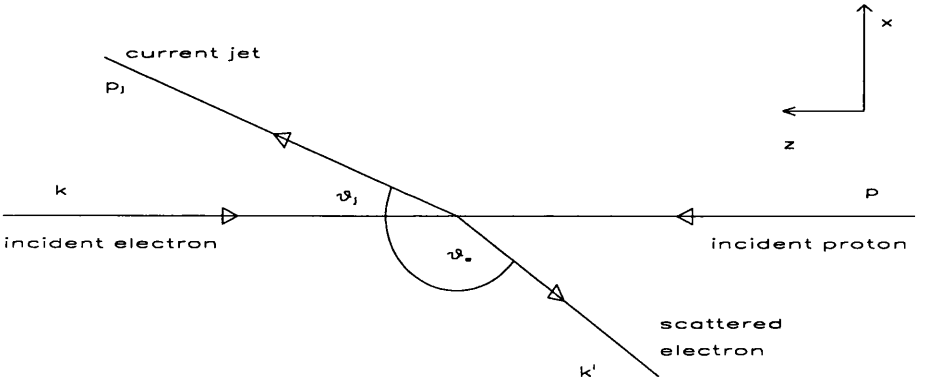

Figure 1.2: Schematic Diagram of an Electron-Proton Collision.

Figure 1.2 is a kinematical diagram of a typical DIS event with a photon as the mediator. Due to the high energies involved, the masses of the electron, the proton, the current jet and the proton remnant jet are negligible, and thus omitted from the following calculations. Four useful Lorentz invariant quantities are constructed to describe the event. These are

$q^2 = (k - k')^2 = (p_j - xp)^2 = -Q^2$ square of the 4-momentum transfer

	(virtuality)
$y = (p \cdot q)/(p \cdot k)$	fractional energy transfer to the proton in the proton rest frame (inelasticity)
$x = Q^2/ys$	Bjorken scaling variable (Bjorken x)
$s = (k+p)^2 = 4E_eE_p$	total centre of mass energy squared

There are a number of ways to determine Q^2, x and y. One method to reconstruct the above variables is the "electron method". In terms of the measured scattered electron,

$$Q^2 = -q^2 = 2k.k' = 2E_eE'_e(1 + \cos\theta_e) \tag{1.3}$$

$$y = 1 - \frac{E'_e}{2E_e}(1 - \cos\theta_e) \tag{1.4}$$

and x follows from $x = Q^2/ys$.

Another method of reconstruction is the Jacquet-Blondel method. This is commonly used to reconstruct y if the outgoing electron is not detected, for example, if it escapes down the beam pipe. The Jacquet-Blondel estimator of y is defined by

$$y_{JB} = \frac{\Sigma_i(E_i - p_{zi})}{2E_e} \tag{1.5}$$

where the sum is over all the hadrons in the event.

The observed structure of the proton depends on Q^2 and x. In the QPM, the proton is assumed to consist of free quarks with no transverse momentum. In the infinite proton momentum limit of this model, Bjorken x is the fraction of the

proton's momentum that the struck parton carries at the point when it interacts with the photon. If the event were an elastic scatter, x would be equal to unity. For DIS events where the proton is broken up, x is less than unity.

1.3 Photoproduction

The probability for a particular interaction to occur is often written in terms of a cross section. The cross section is equal to the probability of a particular interaction occurring per unit time per unit of incoming flux per target particle. At HERA there is a large flux of photons produced by the incoming electron beam. The total ep cross section can be factorised into terms of the photon-proton (γp) cross section, and the flux of incoming photons. The ep cross-section can be written as

$$\frac{d^2\sigma^{ep}}{dydQ^2} = f_\gamma^e(y, Q^2)\sigma_{tot}^{\gamma p}(E_\gamma, Q^2) \tag{1.6}$$

for a given photon flux, $f_\gamma^e(y, Q^2)$, and where E_γ is the energy of the photon. This is known as the equivalent photon approximation (EPA). This can be interpreted as the probability to find a photon in the electron of energy $E_\gamma = yE_e$, which, using the Weizsäcker-Williams Approximation [12], is given by,

$$f_\gamma^e(y, Q^2) = \frac{\alpha}{2\pi Q^2}\left(\frac{1-(1-y)^2}{y} - 2\frac{(1-y)}{y}\frac{Q^2_{min}}{Q^2}\right), \tag{1.7}$$

where Q^2_{min} is the kinematic lower bound, and is equal to $m_e^2y^2/(1-y^2)$ where m_e is the mass of the electron [13].

Hence, the collider can be thought of as a γp collider, since now ep cross sections can be translated into γp cross sections. The large majority of the photons produced are quasireal, that is they are almost real ($Q^2 \approx 0$ GeV^2). This type of real photon-nucleon scattering is classed as photoproduction. The large flux of photons makes HERA an ideal environment to study photonic interactions.

Events with low momentum exchange between photon and proton resemble meson-nucleon scattering. This is soft photoproduction, where both photon and proton behave as objects with spatial extent. Larger momentum exchange events produce high momentum jets of hadrons transverse to the photon-proton beam axis, and the meson-nucleon model of scattering is no longer able to explain the observed final state. It can however be explained in terms of parton-parton scattering, where the partons which collide to produce jets of hadrons are considered to be pointlike. These types of events are termed hard photoproduction.

1.3.1 Hard Photoproduction

Hard photoproduction events are then typically characterised by a quasireal photon, collinear to the electron beam, interacting with the proton to produce two or more jets of hadrons with sizeable transverse momentum (p_T). These jets constitute the hard subprocess. The higher their p_T, the harder is the subprocess. Hard photoproduction is subdivided into two main classes. These are

1. Direct photoproduction. Here the photon interacts directly with the hard subprocess. The fraction of the photon's four momentum entering the hard subprocess, x_γ, is equal to unity. The photon is considered to be pointlike.

2. Resolved photoproduction. Here the photon fluctuates into some hadronic state and behaves as a source of quarks and gluons, one of which takes part in the hard subprocess. One of the main signatures of a resolved process is that of the low transverse momentum photon remnant, the partons produced by the photon which did not take part in the hard scatter. The fraction of the photon's four momentum entering the hard subprocess, x_γ, is now less than unity. The photon is considered to have "structure".

An example of each process is shown in figure 1.3.1. On the left is an example of the diagram corresponding to a direct process, on the right is an example of a

resolved process.

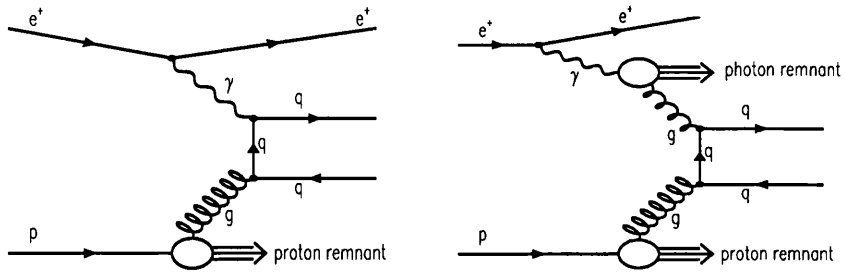

Figure 1.3: Feynman diagrams of direct and resolved processes.

x_γ is the fraction of the photon's four momentum entering the hard dijet subprocess at leading order (LO). It is interpreted in a similar fashion to Bjorken x, except that it provides information on the structure of the photon rather than that of the proton. The distinction between resolved and direct processes becomes blurred at next-to-leading order (NLO). This is because the third jet could be classed as an NLO jet belonging to the hard subprocess, in which case it would be a direct event, or it could be classed as the photon remnant, making it a resolved event. Hence x_γ is only well defined at leading order. It is interesting to note that due to the fact that there is a massive dijet subsystem, Bjorken x now no longer corresponds to the fraction of the proton's momentum carried by the quark or gluon which enters the dijet subprocess [14].

1.4 Jets

As mentioned in the previous section, the quarks and gluons produced in the hard subprocess hadronise into jets of hadrons. Experimentally the partons exiting the hard subprocess cannot be observed directly, rather the jets of hadrons they produce are what is measured. Perturbative QCD calculations are applicable to free partons, but not to bound hadronic states. However, there is a correlation between the initial partonic state exiting the hard subprocess, and the final observable jets of hadrons, and so by measuring jet distributions, using a well

defined procedure, information on the partons can in principle be extracted. This depends on how well the hadronisation is understood. In general, the higher the transverse momentum of a jet, the greater its correlation with the parton that produced it.

The jets are usually defined in terms of their transverse energy, pseudorapidity and azimuthal angle. The transverse energy, E_T, of a jet of hadrons is defined as the component of the jet's momentum transverse to the z-axis (beam axis). The pseudorapidity, η is related to the polar angle, θ, that the jet makes with the positive z-axis (defined to be the direction of the proton beam) as

$$\eta = -\ln\tan(\theta/2) \tag{1.8}$$

The advantage of defining the variable η is that differences in η are Lorentz invariant under boosts along the z-direction.[1] The azimuthal angle, ϕ of the jet then completes the description of the jet. The jets are assumed to have negligible mass with respect to their energy. A fuller and more detailed description of jet definition and measurement is relevant to the analysis presented in this thesis, and so is given later in chapter 5.

1.5 x_γ^{obs}

Experimentally x_γ cannot be measured directly, so the variable x_γ^{obs} is chosen as an estimator of the fraction of the photon's momentum that takes part in the hard scatter. x_γ^{obs} is then the fraction of the photon momentum manifest in the

[1] Rapidity, $y_R = \frac{1}{2}\ln\{(E+p_z)/(E-p_z)\}$, is actually the correct variable to use if differences in the variable are to be Lorentz invariant under boosts along the z-axis. However, if outgoing particle or jet masses can be ignored (their energy is much greater than their mass), then $\eta = y_R$.

two highest E_T jets and is defined by the equation

$$x_\gamma^{obs} = \frac{\sum_{j=1}^{2}(E_j - p_{z_j})}{\sum_{hadrons}(E - p_z)} = \frac{\sum_{j=1}^{2} E_{Tj} e^{-\eta_j}}{2E_e y} \tag{1.9}$$

Since the proton is defined to be travelling in the positive z direction, $(E-p_z)_{proton}$ is zero (assuming the massless approach where the mass of the proton is negligible in comparison with its energy). In photoproduction, the photon is travelling collinear to the electron beam, in the negative z direction, so $(E - p_z)_\gamma = 2E_\gamma = 2E_e y$. This is then the total available $E - p_z$ in the event (as long as the electron is removed from the picture). Measuring the $E - p_z$ manifest in the two jets, and dividing by the total hadronic $E - p_z$ in the event then gives the fraction of the photon's momentum manifest in the two jets.

The fact that jets of hadrons rather than partons are measured, means that the value of x_γ^{obs} is dependent upon the jet finding algorithm used and hadronisation effects. Events with a high value of x_γ^{obs} are mostly direct processes, whilst low x_γ^{obs} events are mostly resolved processes. As a result of this, "direct-enriched" events are classed as being those with $x_\gamma^{obs} > 0.75$, and "resolved-enriched" events as those with $x_\gamma^{obs} < 0.75$. This is an experimental definition, since there are still true resolved events with $x_\gamma^{obs} > 0.75$, and vice versa, but the contamination between the two event classes is minimised by having the cut at this value. This can be seen in figure 1.4 where the histograms come from Monte Carlo generated events. Hence it is possible to access those events generated with an x_γ equal to unity (direct processes only). This is superimposed as the shaded histogram.

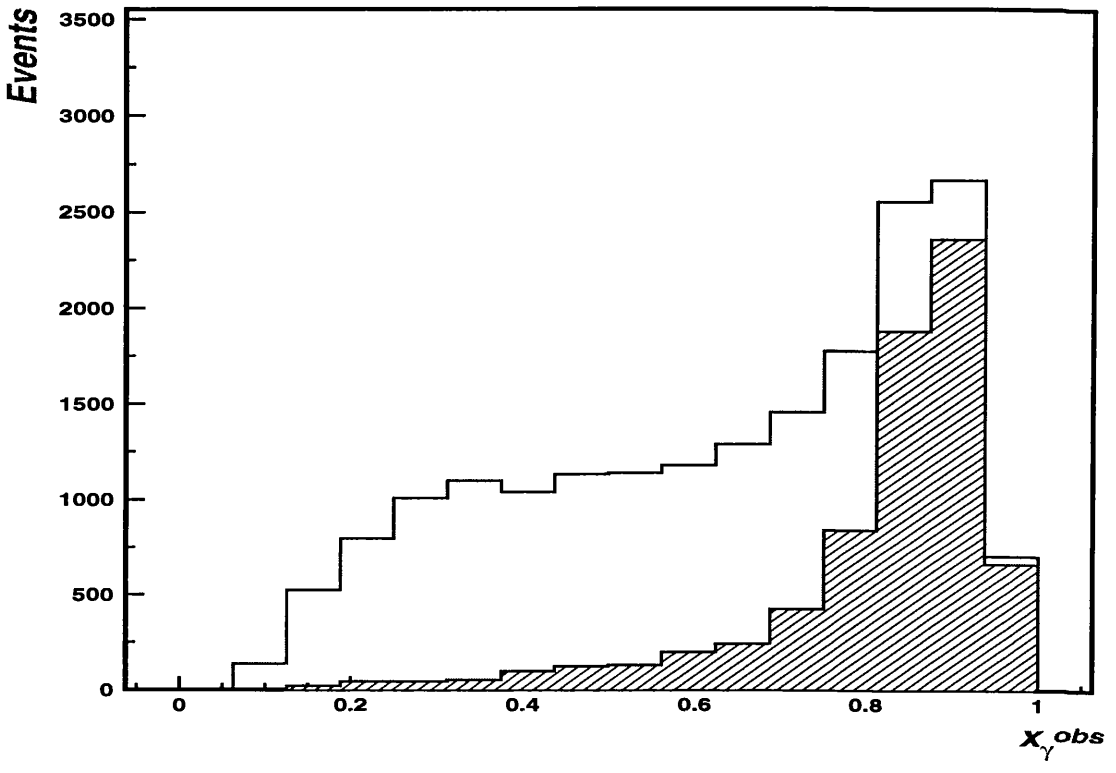

Figure 1.4: Example of an x_γ^{obs} distribution with the direct only process shown as the shaded histogram.

Chapter 2

Photon Structure

Evidence for resolved photon processes was seen in the early stages of HERA operation [11] via the observation of large energy deposits in the rear (electron) direction consistent with a photon remnant. This implies that the photon has some kind of structure, with a final state topology similar to a hadron-hadron like collision. To introduce the language and details of hadronic structure investigation at HERA, the structure of the proton will be discussed first.

2.1 The Structure Function F_2

In the QPM, the inelastic electron-proton scattering cross section is calculated as the incoherent sum of all possible electron-quark scatters. For one such scatter, the lepton-quark differential cross section is given by

$$\frac{d\sigma}{dQ^2} = \frac{4\pi\alpha^2 e_q^2}{Q^4}\left(1 - y + \frac{y^2}{2}\right) \tag{2.1}$$

where all masses are neglected and e_q is the electric charge of the quark. This can now be modified to the cross section for electron-proton scattering by defining the parton distribution function $f_q^p(x)dx$ as the probability of having a quark of type q with momentum fraction x of the proton, to give

$$\frac{d\sigma^{ep}}{dQ^2} = \frac{4\pi\alpha^2}{Q^4} \int \sum_q e_q^2 f_q^p(x) \left(1 - y + \frac{y^2}{2}\right) dx \tag{2.2}$$

This formula can be rewritten in terms of the dimensionless structure functions F_1 and F_2.

2.1.1 F_2^{proton}

In the case of deep inelastic electron-proton scattering, the double differential cross section in terms of two proton structure functions F_1 and F_2 is

$$\frac{d^2\sigma^{ep}}{dxdQ^2} = \frac{4\pi\alpha^2}{xQ^4} \left(xy^2 F_1 + (1-y)F_2\right) \tag{2.3}$$

where the structure function F_2 is given by [19]

$$F_2(x) = \sum_{q,\bar{q}} e_q^2 x f_q(x) \tag{2.4}$$

with the sum being over all quark flavours in the proton, e_q the electromagnetic charge of the quark and $f_q(x)$ the probability of the quark or antiquark, q, carrying a fraction x of the proton's momentum. In the QPM, for scattering off fermions, the two structure functions are related by the Callan-Gross relation [20]

$$F_1(x) = \frac{1}{2x} F_2(x) \tag{2.5}$$

hence cross sections are normally written in terms of F_2 only. The QPM predicts F_2 to have a dependence on x, but not on Q^2. This dependence only on x and not Q^2 is known as scaling [21]. This is a consequence of the QPM regarding the proton as consisting only of free pointlike quarks. An increase in Q^2 is equivalent to an increase in the ability to resolve smaller objects within the proton. Since all the objects are considered to be pointlike and non-interacting, an increase in the resolution will not improve the view of a pointlike object, and thus scaling is expected if the model is to hold good.

A third structure function which is often used is

$$F_L = F_2 - 2xF_1 = \frac{Q^2}{4\pi^2\alpha}\sigma_L \tag{2.6}$$

where σ_L is the longitudinal contribution to the cross section, and the structure function F_L relates only to the absorption of longitudinally polarised photons. The cross section now becomes

$$\frac{d^2\sigma^{ep}}{dxdQ^2} = \frac{2\pi\alpha^2}{xQ^4}\left[(1+(1-y)^2)F_2 + 2(1-y)F_L\right] \tag{2.7}$$

In the QPM, equation 2.5 predicts that F_L should be zero, and the partons in the proton should couple only to transversely polarised photons. However, the QPM fails to account for certain experimental results which led to the need for a new improved model.

2.1.2 The QCD Improved Parton Model

If the proton consisted solely of quarks and antiquarks, then their momenta would sum up to that of the proton. However, experimentally it is found [22] that

$$\sum_q \int_0^1 x f_q^p(x)dx \approx 0.5 \tag{2.8}$$

and since this is not equal to unity, this was the evidence for neutral partons inside the proton, as the photon couples only to charged particles. These neutral partons constitute the sea of gluons inside the proton, radiated from quarks, and in turn splitting into $q\bar{q}$ pairs themselves. This gluon radiation introduces some transverse momentum to the quarks inside the proton, allowing them to couple to both longitudinally as well as transversely polarised photons. The Callan-Gross relation now breaks down, and F_L is no longer zero. Scaling is violated and the structure function F_2 is now a function of both x and Q^2.

In the QCD improved parton model, the proton no longer consists merely of quasifree quarks, but a sea of gluons and virtual $q\bar{q}$ pairs. Within the framework

of perturbative QCD, equation 2.4 is modified (to first order) by calculating the cross section for photon absorption by a quark including all diagrams with a gluon emitted from the quark line to give [23]

$$F_2(x,Q^2) = x\sum_q e_q^2\left(q(x) + \Delta q(x,Q^2)\right) \tag{2.9}$$

where $q(x) = f_q^p(x)$ at some input scale Q_0^2, and

$$\Delta q(x,Q^2) = \frac{\alpha_s}{2\pi}\ln\frac{Q^2}{\mu^2}\int_x^1 \frac{d\xi}{\xi} q(\xi) P_{qq}\left(\frac{x}{\xi}\right), \tag{2.10}$$

μ^2 is a lower limit on Q^2 introduced in order to regulate the singularity as $Q^2 \to 0$ and $P_{qq}(x/\xi)$ is called a splitting function and is the probability that a quark or antiquark with momentum fraction ξ emits a gluon and is left with momentum fraction x. At a scale of $Q^2 \approx Q_0^2$, the valence quarks in the proton are just being resolved by the photon. The structure function at higher values of Q^2 can now be calculated, given a reference value for $q(x,Q_0^2)$ by looking at the change in $\Delta q(x,Q^2)$ for a small change in $\ln Q^2$, using the formula [23]

$$\frac{dq(x,Q^2)}{d\ln Q^2} = \frac{\alpha_s}{2\pi}\int_x^1 \frac{d\xi}{\xi} q(\xi,Q^2) P_{qq}\left(\frac{x}{\xi}\right) \tag{2.11}$$

The emission of a gluon is not the only process to occur inside the proton. The emitted gluon itself can interact with other quarks, antiquarks or gluons. To first order, there are four interactions which can occur, and four splitting functions which give the probability of the initial quark, antiquark or gluon radiating a parton. The same procedure as for determining the evolution of the quark/antiquark density can be applied to the gluon density. The resultant equations are called the Dokshitzer-Gribov-Lipatov-Altarelli-Parisi (DGLAP) equations [23] and predict a logarithmic dependence on Q^2:

$$\frac{dq_S(x,Q^2)}{d\ln Q^2} = \frac{\alpha_s}{2\pi}\int_x^1 \frac{d\xi}{\xi}\left[q_S(\xi,Q^2)P_{qq}\left(\frac{x}{\xi}\right) + g(\xi,Q^2)P_{qg}\left(\frac{x}{\xi}\right)\right] \tag{2.12}$$

$$\frac{dg(x,Q^2)}{d\ln Q^2} = \frac{\alpha_s}{2\pi}\int_x^1 \frac{d\xi}{\xi}\left[q_S(\xi,Q^2)P_{gq}\left(\frac{x}{\xi}\right) + g(\xi,Q^2)P_{gg}\left(\frac{x}{\xi}\right)\right] \tag{2.13}$$

where $q_S(x,Q^2) = \sum_i [q_i(x,Q^2) + \overline{q}_i(x,Q^2)]$ is the singlet quark and antiquark density summed over all quark flavours i, and $g(x,Q^2)$ is the gluon density.

Set 'A' of the Martin, Roberts and Stirling model of the proton (MRSA) [46] is one of many which uses the DGLAP evolution equations, and is the model used later in this thesis in the simulation of photon-proton scattering. The parton densities in the proton are determined from a global fit to a wide range of deep inelastic and related data. These densities are then parametrised at a sufficiently large scale ($Q_0^2 \approx 4$ GeV^2) so that the parton densities can be calculated at higher Q^2 using the DGLAP equations. A graph of the momentum distribution of the up quark from this model, at a Q^2 of 10 GeV^2, is shown in figure 2.1. The falling distribution as x increases is a characteristic of the "sea" quarks in the proton, whereas the peak at $x \approx 0.2$ is due to the valence quarks.

2.1.3 F_2^γ

In a similar fashion to F_2^{proton}, the structure function of the photon, F_2^γ is defined. The measurements of F_2^γ to date come from electron-positron colliders [24], where both leptons emit a photon. One photon is quasireal, and the other is virtual, and probes the quark content of the real photon. Such measurements are reliant on good reconstruction of the hadronic final state in order to correct for detector acceptance effects. The statistics are improving all the time with higher integrated luminosity samples, even though the cross section for such scatters is low compared with the other processes that occur in e^+e^- interactions.

The measurement of F_2^γ is the determination of the quark and antiquark content in the photon. At HERA, there are events where the photon is probed by a dijet system. That is, the dijets have a hard enough scale, or small enough wavelength to resolve structure within the photon. However, the dijet system can

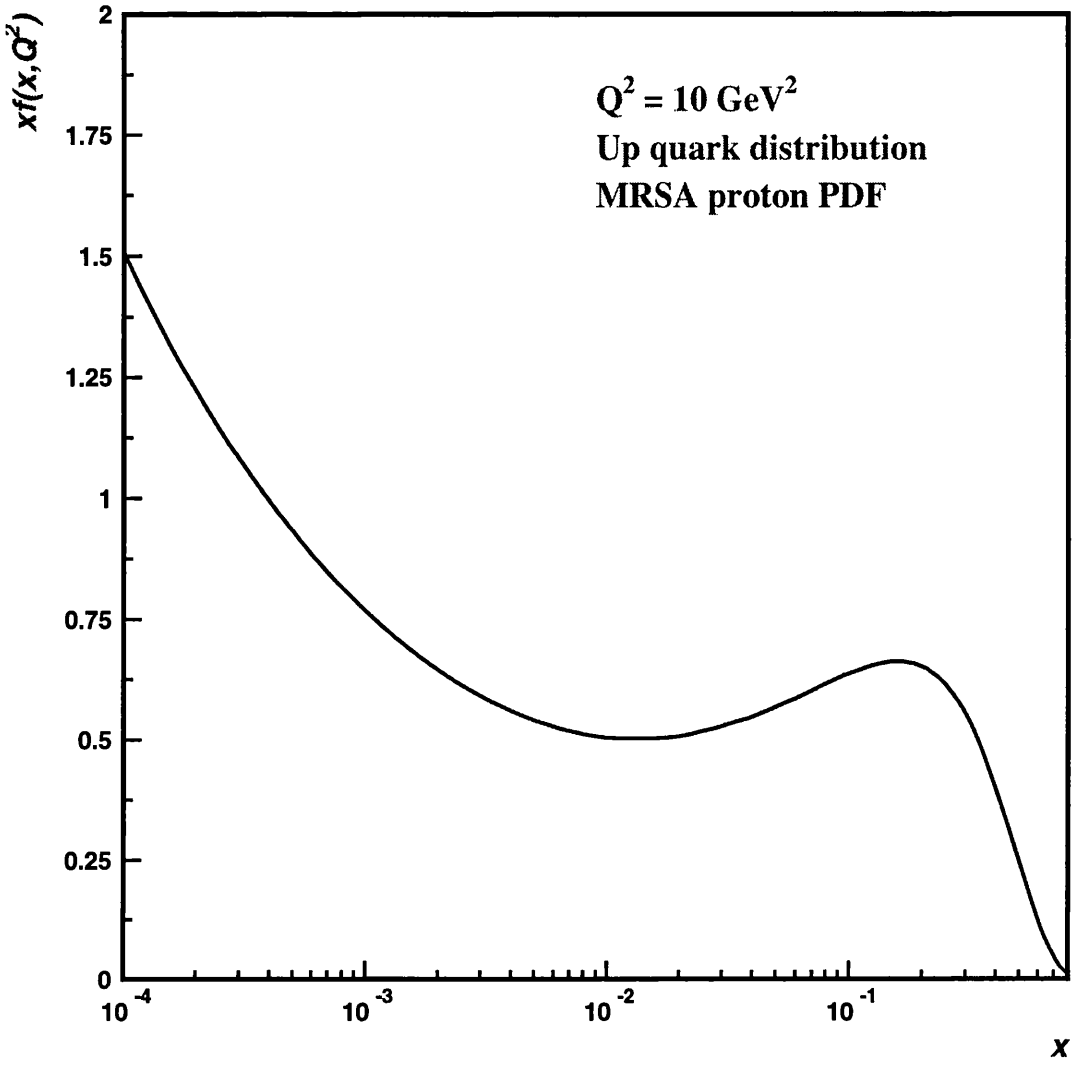

Figure 2.1: MRSA momentum distribution of the up quark in the proton.

couple to gluons as well as quarks in the photon. Consequently, F_2^γ cannot be measured directly at HERA. However, information on the structure can still be extracted, and with the large flux of photons available, statistical limitations are not a problem. Also, the measurement of F_2^γ provides no information on the gluon content of the photon, which is needed if a full picture of the photon structure is to be obtained. In the case of the proton, there is a momentum sum rule which requires $\int xq_S(x)dx + \int xg(x)dx = 1$. Measurements of F_2^{proton} therefore

constrain the gluon density inside the proton as well as the quark density. In the case of the photon, no such sum rule exists, due to its structure coming from an initial $\gamma \to q\bar{q}$ splitting. The direct photon which has no structure then adds a third component to the possible structure of the photon, and this extra degree of freedom means that the structure is not constrained by measuring only F_2^γ.

Analagous to the case of the proton, F_2^γ is defined as

$$F_2^\gamma(x_\gamma, \mu^2) = x_\gamma \sum_{q,\bar{q}} e_q^2 q^\gamma(x_\gamma, \mu^2) \tag{2.14}$$

where μ^2 refers to the scale of the probe originating from the proton, an example of which is a dijet process, where the dijet system provides the hard scale to probe the photon, and x_γ is the fraction of the photon's momentum which takes part in the scatter off the dijet system. The DGLAP equations describing the dependence of the photonic parton densities on μ^2 now has the form [18]

$$\frac{dq_S(x_\gamma, \mu^2)}{d\ln\mu^2} = a(x_\gamma) + \frac{\alpha_s}{2\pi}\int_{x_\gamma}^1 \frac{d\xi}{\xi}\left[q_S(\xi,\mu^2)P_{qq}\left(\frac{x_\gamma}{\xi}\right) + g(\xi,\mu^2)P_{qg}\left(\frac{x_\gamma}{\xi}\right)\right] \tag{2.15}$$

$$\frac{dg(x_\gamma, \mu^2)}{d\ln\mu^2} = \frac{\alpha_s}{2\pi}\int_{x_\gamma}^1 \frac{d\xi}{\xi}\left[q_S(\xi,\mu^2)P_{gq}\left(\frac{x_\gamma}{\xi}\right) + g(\xi,\mu^2)P_{gg}\left(\frac{x_\gamma}{\xi}\right)\right] \tag{2.16}$$

where

$$a(x_\gamma) = \sum_i 3e_i^2 \frac{\alpha}{2\pi}\left[x_\gamma^2 + (1-x_\gamma)^2\right] \tag{2.17}$$

and represents the initial $\gamma \to q\bar{q}$ splitting, the summation being over all quark and antiquark flavours i. The dependence on the scale, which in the case of dijets is typically assumed to be the sum of the transverse momenta squared of the jets, is again a logarithmic dependence.

2.2 Models of Photon Structure

For low photon virtualities, models of the photon structure are often split into three separate contributions. These are the direct, vector meson dominance (VMD) and anomalous contributions.

2.2.1 Direct Photon Interactions

These are the hard interactions where the photon interacts in a pointlike manner. The photon couples directly to a parton from the proton. The dominant leading order Feynman diagrams for direct photons are shown in figure 2.2. In (a) the

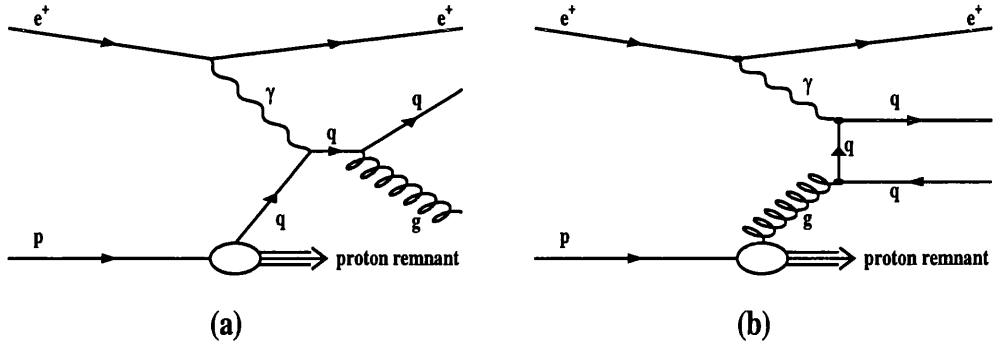

Figure 2.2: Leading order direct processes. (a) QCD Compton (b) Photon gluon fusion.

photon couples to a quark in the proton, which now has a high virtuality, and becomes real again via the emission of a gluon. This type of event is known as QCD Compton scattering. In (b) the photon couples to a quark in a quark-antiquark pair produced by a gluon from the proton. This is known as photon gluon fusion (or one example of boson gluon fusion where the boson exchanged can be a photon, W or Z boson).

2.2.2 Vector Meson Dominance

Given that a photon is a boson with spin one, the hadronic states it can fluctuate into should have the same quantum numbers. These hadronic states are the vector mesons such as the ρ_0, ω and ϕ. In this vector meson dominance (VMD) model [15], the photon-proton cross section is written as [16]

$$\sigma^{\gamma p}_{VMD} = \sum_{V=\rho^0,\omega,\phi} \frac{4\pi\alpha}{f_V^2}\sigma^{Vp} \tag{2.18}$$

where f_V is the specific scaling factor giving the probability that the photon will fluctuate into a vector meson, V. The lifetime of such fluctuations into a vector meson are approximately [17]

$$t_f \approx \frac{2E_\gamma}{m_V^2 + Q^2} \tag{2.19}$$

where E_γ is the energy of the photon and m_V is the mass of the vector meson V. The probability of vector meson interactions is proportional to this lifetime. Hence the probability of such fluctuations in DIS is suppressed as the photon virtuality increases, and is most prevalent in the photoproduction regime.

The vector meson then interacts with the proton and either scatters elastically or inelastically. In the elastic case the vector meson does not break up and is found in the final state. This will generally be found in the direction of the photon, and will be termed the photon remnant. In the inelastic case, a parton from the meson interacts with a parton from the proton, and the remaining partons from the meson form the photon remnant.

2.2.3 Anomalous Photon Interactions

The VMD model is concerned with $q\overline{q}$ pairs which have enough time to form bound states that are the vector mesons. $q\overline{q}$ pairs can also be produced in an unbound state, their relative transverse momenta being too large for the pair to fall into a bound vector mesonic state. This is termed the anomalous photon

interaction [18]. The topology of the final state appears to have a hadronic remnant in the direction of the photon. One of the quarks produced by the photon interacts with the proton, leaving the other quark to continue onwards and form the photon remnant. Due to the high transverse momentum of the quarks at the $\gamma \rightarrow q\bar{q}$ vertex, such processes can be calculated in perturbative QCD.

2.2.4 Resolved Photon Interactions

At leading order the separation of the VMD and anomalous processes is not well defined, rather there is a continuous transition from VMD to anomalous processes. Indeed, as the transverse momentum between the anomalous $q\bar{q}$ pair increases, there is also a continuous transition from anomalous to next-to-leading order direct events where the remnant can now be viewed as a third jet rather than as a remnant. The particular process invoked to model the interaction depends on the cut on the transverse momentum of the $q\bar{q}$ pair that is chosen. These two processes are usually then combined into one, called the resolved photon process. This is a label used for all the cases where the photon acts as a source of partons for the hard scatter, and is characterised by a photon remnant travelling in the direction of the photon for low Q^2 events. It is then possible to write the total photon-proton cross section as

$$\sigma_{tot}^{\gamma p} = \sigma_{VMD}^{\gamma p} + \sigma_{anom}^{\gamma p} + \sigma_{dir}^{\gamma p} \tag{2.20}$$

or if the anomalous and VMD contributions are combined

$$\sigma_{tot}^{\gamma p} = \sigma_{res}^{\gamma p} + \sigma_{dir}^{\gamma p} \tag{2.21}$$

2.2.5 GRV Photon Parton Density Function

The Glück, Reya and Vogt (GRV) model is one example of a parameterisation of the structure of the real photon. It generates the structure of the photon starting

from a very low input scale ($\mu_0^2 = 0.25$ GeV^2) and evolving up to higher scales μ^2 using the equation [47]

$$(f_q^\gamma, f_g^\gamma) = \kappa \frac{4\pi\alpha}{f_\rho^2}(f_q^{\pi^0}, f_g^{\pi^0})(x_\gamma, \mu^2, \mu_0^2) \tag{2.22}$$

It is motivated by VMD ideas, with f_ρ^2 being the transition probability for the photon to fluctuate into a ρ meson, and κ is a free parameter determined from fits to data, which takes into account contributions from the photon fluctuating into heavier vector mesons. It assumes the photon parton density to resemble that of the pion at the starting scale, the pion having a structure similar to that of the proton in figure 2.1. The addition of the anomalous contribution completes the GRV prescription for the real photon. The momentum distribution of the up quark in this model is shown in figure 2.3. The peak at low x_γ is due to the VMD contribution, which dies out at higher values of x_γ. Conversely, the peak at high x_γ is due to the anomalous contribution, and is a typical trait of events where the photon splits into lepton-antilepton or quark-antiquark pairs.

2.3 Multi-parton Interactions

In resolved photon processes, it is possible that the parton source that the photon has become, can have more than one hard interaction with the proton. This will lead to more transverse energy being produced in the event than if there was only the one hard scatter (see figure 2.4). A model that does not include the multi-parton interaction (MI) contribution will typically underestimate the cross section that is measured, if that cross section includes a cut on the transverse energy in the event. Typical cross sections in the photoproduction regime have a requirement of at least two jets above a certain transverse energy threshold, and so these cross sections will contain the MI contribution at some level. Events with direct photons cannot contain MIs. The MIs enhance only the resolved

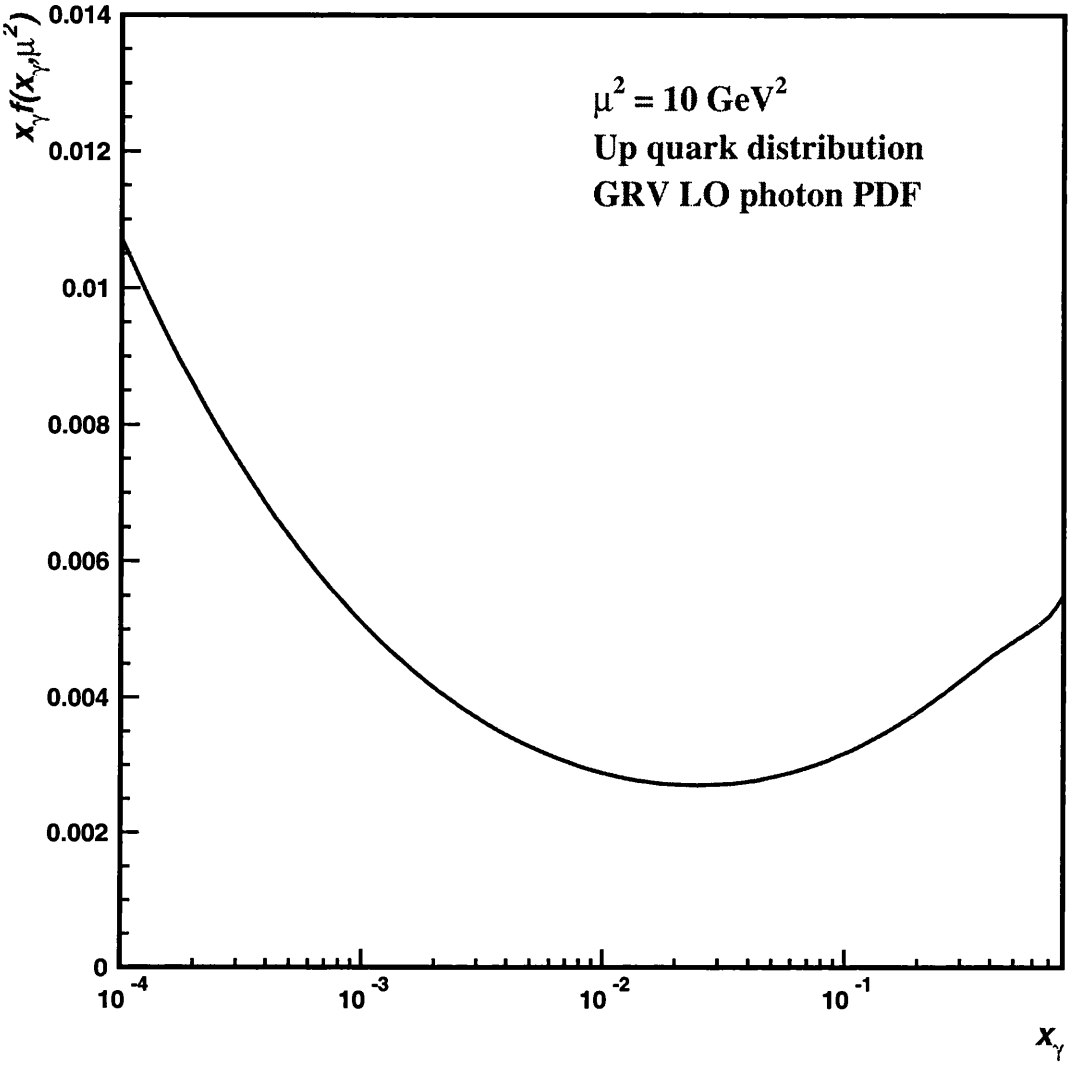

Figure 2.3: GRV LO momentum distribution of the up quark in the photon.

contribution to the cross section.

2.4 Jet Cross Sections in Photoproduction

The expression for a jet cross section can be factorised into two parts. One part pertains to the hard parton-parton (dijet) subprocess, $\hat{\sigma}$, at the hard scale p_T^2 (squared transverse momentum of the jets), and the other part covers the photon

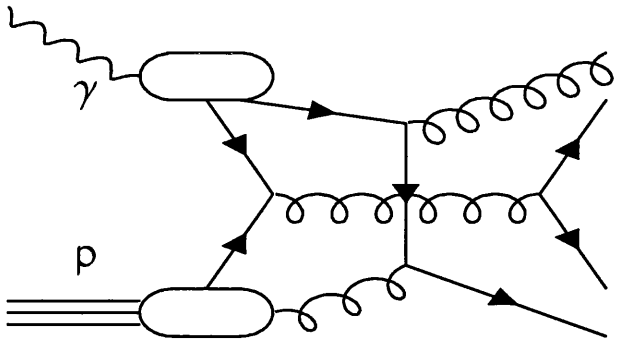

Figure 2.4: Diagram of a multi-parton interaction in a photon-proton collision.

flux, f_γ^e, and the parton density functions (PDFs) of the incoming beam particles, f_γ and f_p

$$\frac{d\sigma_{jet}}{dx_\gamma dx_p dy dp_T} = [f_\gamma^e(y) f_\gamma(x_\gamma, p_T^2) f_p(x_p, p_T^2)] \times \left[\frac{d\hat{\sigma}}{dp_T}\right] \tag{2.23}$$

where x_p is the fraction of the proton's momentum carried by the incoming parton from the proton. Jet photoproduction measurements have been shown to be sensitive to the PDFs within the proton and the photon [25]. These measurements are complementary to those for F_2^{proton} and F_2^γ as they probe the gluonic content as well as the quark content of the proton and photon.

The p_T^2 of the jets provides a hard scale for the event. As long as this scale is much greater than the virtuality of the photon ($p_T^2 \gg Q^2$), then it is the photon that is being probed by the dijet system, rather than the photon probing the proton as is the case in high Q^2 DIS [17]. One might expect that the higher the jet p_T, the more structure that will be resolved in the photon. This is not always the case, as the jet transverse momenta are correlated with x_γ. The higher the p_T, the more energy that is required to produce such jets. This is favoured by direct photon interactions, since all of the photon energy enters the dijet system.

So far, the emphasis has been on photoproduction and the structure of the quasireal photon. The photon can also be virtual and have structure, in which case the PDF of the photon might, and indeed does depend on its virtuality.

This Q^2 dependence will also affect the cross section for jet production, and hence information on the evolution of the partonic density of the virtual photon with respect to Q^2 and the probing scale of the dijet system can be gained from such jet cross section measurements.

2.5 Virtual Photons

In addition to real photons, virtual photons are also expected to exhibit some structure. Whereas the parton density in the photon changes logarithmically with the probing scale, the Q^2 dependence of the anomalous and VMD contributions is expected to be a much more marked effect. The parton density is suppressed with increasing photon virtuality as $\ln(p_T^2/Q^2)$ for the anomalous case, and as $[m_V^2/(m_V^2 + Q^2)]^2$ for the VMD part [26]. The VMD contribution is much more suppressed with photon virtuality than the anomalous contribution, but both become negligible contributions to the cross section for very high Q^2, when the photon behaves in a direct (pointlike) manner only. As long as the photon virtuality does not approach the mass squared of the weak bosons, the contribution of $W^{\pm}$ or Z^0 exchange to the cross section is negligible.

The event now has two variable scales, p_T^2 and Q^2. Recall: if $p_T^2 \gg Q^2$, then it is the virtual photon that is being probed, and not the proton. The absolute value of these two scales does not define the structure that exists in the virtual photon, rather their relative values. Now that Q^2 is not fixed, as it was in the photoproduction case, equation 2.23 can be modified to include the Q^2 dependence to become

$$\frac{d\sigma_{jet}}{dx_\gamma dx_p dy dp_T dQ^2} = [f_\gamma^e(y) f_\gamma(x_\gamma, p_T^2, Q^2) f_p(x_p, p_T^2, Q^2)] \times \left[\frac{d\hat{\sigma}}{dp_T}\right] \qquad (2.24)$$

The dependence of jet cross sections on Q^2, x_γ and p_T^2 provides information on the partonic content of the virtual photon, which could in principle be used to

constrain models of the virtual photon. Very little experimental information exists on PDFs of virtual photons. For a long time the only published data were from the PLUTO collaboration [27], but hampered by low statistics. More recent measurements include those of the L3 and OPAL collaborations [28, 29], but are still statistically limited in comparison with the HERA experiments. Hence, the HERA experiments are in a unique position to contribute their knowledge about the virtual photon PDFs, despite the measurements being averaged over the quark and gluon densities in the virtual photon. Measurements can be performed for a very wide range of Q^2, probing the photon structure at scales, p_T^2, much larger than those of e^+e^- experiments.

2.5.1 SaS1D Virtual Photon Parton Density Function

An example of a parton density function of the virtual photon is one of the models proposed by Schuler and Sjöstrand [26]. The particular PDF used later in this thesis is the SaS1D photon PDF, which starts with a low input scale of 0.6 GeV^2, and proposes a parton density which evolves with Q^2 in a similar fashion to that of the VMD model, hence linking perturbative and non-perturbative contributions and allowing a smooth transition in the limit $Q^2 \to 0$. The resultant parton density in the virtual photon, f_{γ^*}, is given in terms of the density of quarks derived from a $\gamma \to q\bar{q}$ splitting, $f_{\gamma,q\bar{q}}$ by

$$f_{\gamma^*}(x_\gamma, \mu^2, Q^2) = \int_0^{\mu^2} \frac{dk^2}{k^2} \left(\frac{k^2}{k^2+Q^2}\right)^2 \frac{\alpha}{2\pi} \sum_{q\bar{q}} e_q^2 f_{\gamma,q\bar{q}}(x_\gamma, \mu^2, k^2) \qquad (2.25)$$

and separating the equation into two parts, the first corresponding to the VMD contribution, and the second to that of the anomalous case

$$\begin{aligned} f_{\gamma^*}(x_\gamma, \mu^2, Q^2) = &\sum_V \frac{4\pi\alpha}{f_V^2} \left(\frac{m_V^2}{m_V^2+Q^2}\right)^2 f_{\gamma,V}(x_\gamma, \mu^2, \mu_0^2) \\ &+ \frac{\alpha}{2\pi} \sum_{q\bar{q}} e_q^2 \int_{\mu_0^2}^{\mu^2} \frac{dk^2}{k^2} \left(\frac{k^2}{k^2+Q^2}\right)^2 f_{\gamma,q\bar{q}}(x_\gamma, \mu^2, k^2) \end{aligned} \qquad (2.26)$$

where μ_0^2 is the input scale of 0.6 GeV^2, μ^2 is the probing scale at which f_{γ^*} is to be calculated, and the integral is replaced by a sum over the discrete vector meson states which the photon can become. This PDF exhibits the required suppression of partonic density with Q^2 as expected in the case of virtual photons whilst smoothly mixing the VMD and anomalous contributions. The corresponding up quark momentum distributions for a range of different photon virtualities are shown in figure 2.5. The peak at low x_γ which corresponds to the VMD contribution is rapidly suppressed with increasing Q^2, leaving only the anomalous contribution. The anomalous part is also suppressed with increasing Q^2, but at a slower rate. Overall, the total resolved contribution is reduced as Q^2 rises.

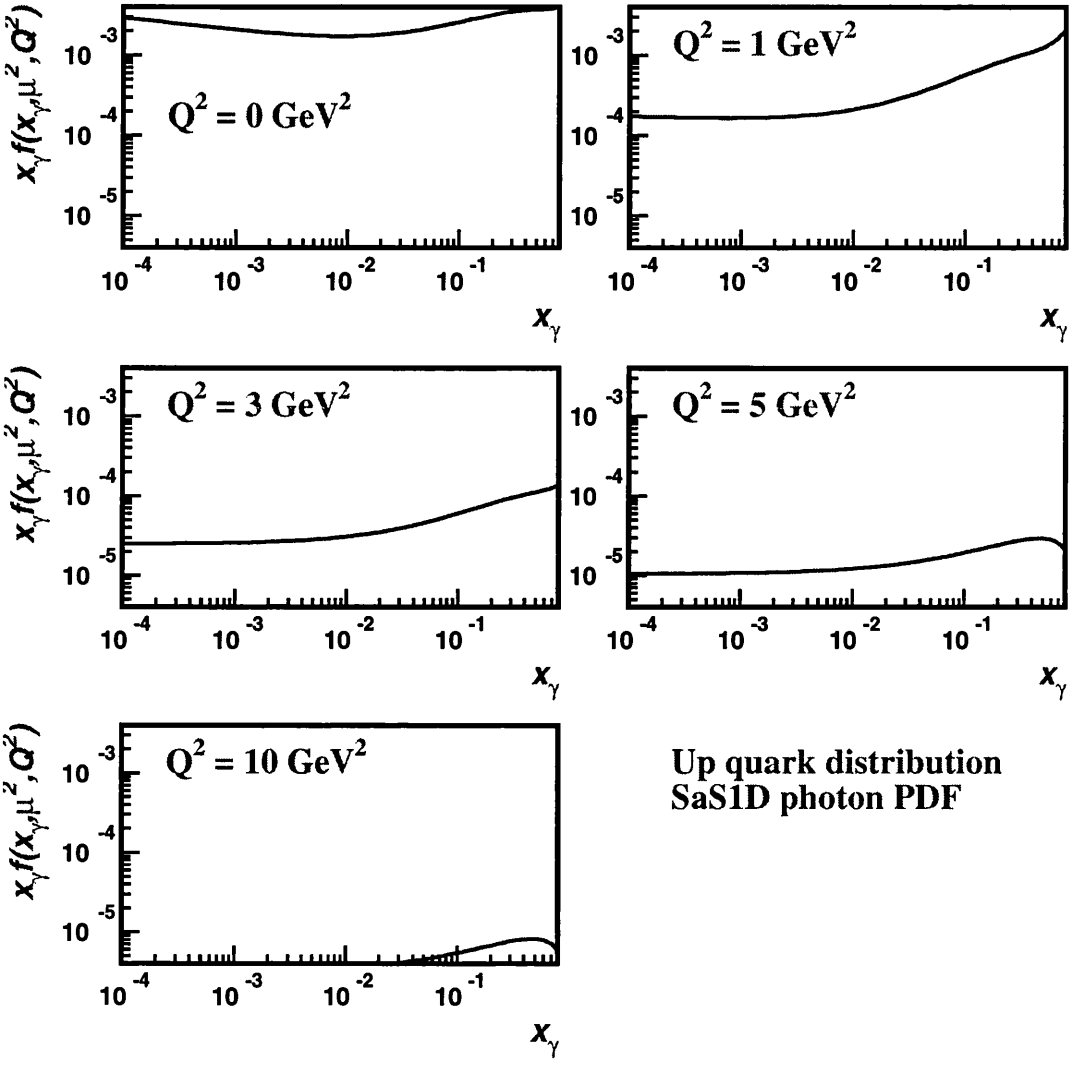

Figure 2.5: SaS1D momentum distribution of the up quark in the photon. The scale, μ^2, is set to 10 GeV^2.

Chapter 3

HERA and the ZEUS Detector

3.1 HERA

The Hadron Elektron Ring Anlage (HERA) is the world's first electron-proton collider, and is situated at the Deutsches Elektronen Synchrotron (DESY) in Hamburg, Germany. During 1996 and 1997 it collided 27.5 GeV positrons with 820 GeV protons, yielding a centre of mass energy of 314 GeV. The two counter-rotating particle beams are brought to collision at one of two sites, around each of which a general purpose detector is situated. The two detectors are H1, located at the north hall, and ZEUS at the south hall. Two fixed target experiments were added after H1 and ZEUS. HERMES makes use of the polarisation of the electron[1] beam together with a polarised gas target in order to study spin structure functions. The HERA-B experiment collides the fringes of the proton beam with a fixed wire target to produce B mesons, and hence studies the physics of the bottom quark. Figure 3.1 shows a schematic of the HERA accelerator complex.

The electrons and protons are accelerated in stages before being injected

[1]HERA is able to produce either electron or positron beams. For technical reasons, positrons have been used since the middle of 1994. In what follows, the term electron will be used to mean electron and/or positron

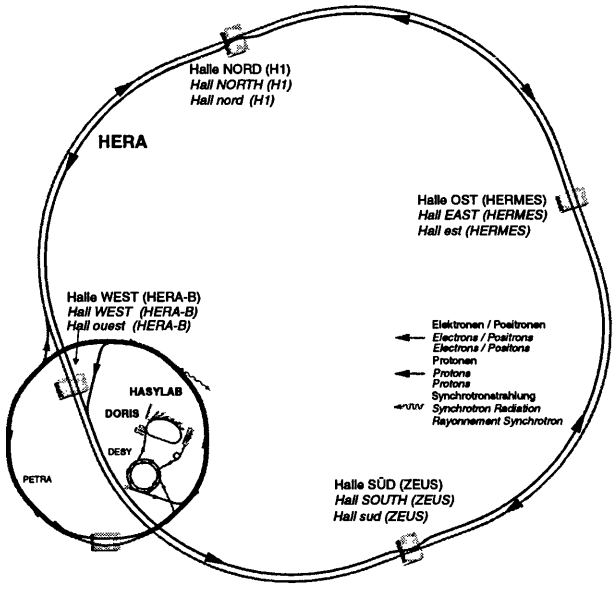

Figure 3.1: Schematic diagram of the HERA accelerator complex.

into the main HERA ring as bunches to be accelerated further to their nominal interaction energies. HERA can hold up to a maximum of 210 electron and proton bunches, each separated by about 30 metres, leading to a bunch crossing at the interaction sites every 96 ns. Not all of the bunch slots are filled. Some are left empty in order to study the effects of background interactions between electrons or protons with residual gas molecules in the accelerator ring.

3.2 ZEUS

3.2.1 Overview

The ZEUS detector is designed as a general purpose experiment, capable of measuring all products of an *ep* collision. The detector is almost hermetic, with just the beam pipes preventing it from having a total 4π solid angle coverage. A brief overview is presented here, with emphasis on some of the main components used in the results presented in this thesis. A more detailed description can be

found in [30].

The standard ZEUS coordinate system is right handed, with the z-axis pointing in the direction of the proton beam, and the x-axis pointing towards the centre of the HERA ring. The origin is defined to be the mechanical centre of the Central Tracking Detector (CTD), which coincides with the nominal position of the ep interaction point.

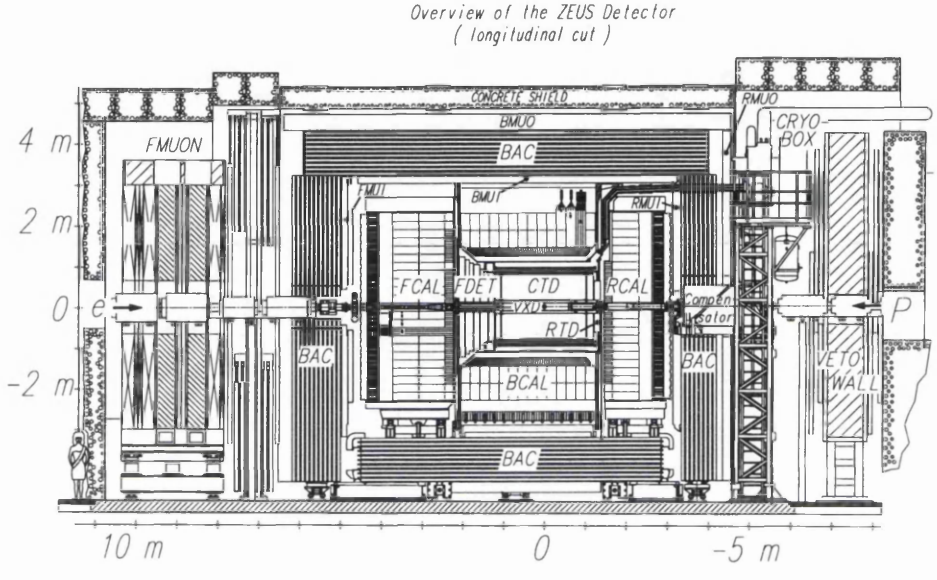

Figure 3.2: Schematic diagram of the ZEUS detector in the yz plane.

Figures 3.2 and 3.3 show a cross section through the ZEUS detector in the yz plane (along the beam direction) and in the xy plane respectively. Starting from the centre outwards, the main components of the ZEUS detector are [2]

- Central tracking detector (CTD): the main tracking detector of ZEUS, it provides momentum measurements of charged tracks in the central region, and is surrounded by a superconducting solenoid magnet which provides a field of 1.43 Tesla.

[2]Vertex detector (VXD): designed to measure charged tracks close to the beam line, but due to technical reasons, this has not been operational since 1995, at the end of which year it was removed, and so will not be discussed further.

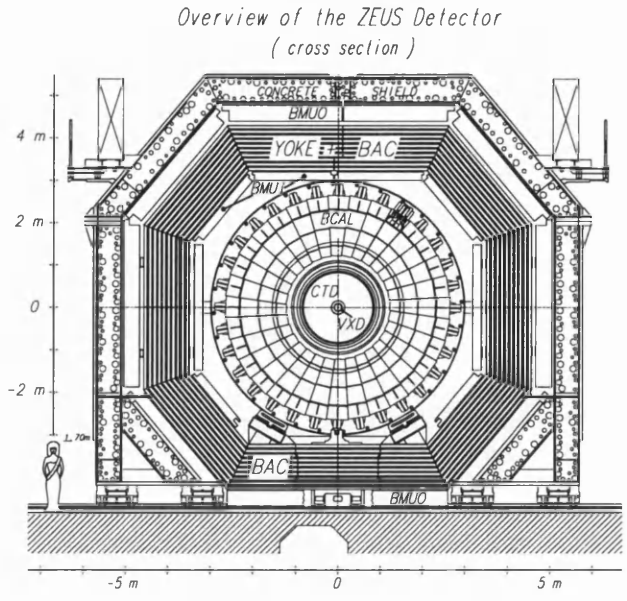

Figure 3.3: Schematic diagram of the ZEUS detector in the xy plane.

- Forward and rear tracking detectors (FDET and RTD): these are drift chambers positioned at both ends of the CTD, and provide additional tracking information for forward and rear charged particles, which are outside the region measurable by the CTD.

- Uranium calorimeter (UCAL): a high resolution depleted uranium scintillator sandwich calorimeter. It is designed to measure the energy and position of charged and neutral particles. It is divided into three sections; the forward calorimeter (FCAL), the barrel calorimeter (BCAL) and the rear calorimeter (RCAL).

- Backing calorimeter (BAC): used as both the return yoke of the central solenoid magnet and as an extra calorimeter for the measurement of any energy leaking from the CAL from extremely energetic particles.

- Muon chambers (F/B/RMUON): these surround the UCAL, both in front of and behind the yoke to measure the trajectory of energetic muons which have traversed the CAL.

- Veto wall (VETO): situated at $z = -750$cm, it absorbs beam halo particles which accompany the proton bunches.

- Luminosity monitor (LUMI): measures the luminosity delivered to ZEUS by measuring the Bethe-Heitler process $ep \rightarrow ep\gamma$. It comprises two separate calorimeters for detecting small angle scatter electrons and photons.

The components of the detector used in this analysis are described in more detail in the following sections.

3.2.2 Central Tracking Detector

The CTD is a cylindrical wire drift chamber with an inner and outer radius of 18.2 cm and 79.4 cm respectively, and a length of 205 cm. The angular coverage is $15° < \theta < 164°$. It is made up nine superlayers (see figure 3.4) containing cells with eight sense wires per cell. Of the nine superlayers, five have sense wires

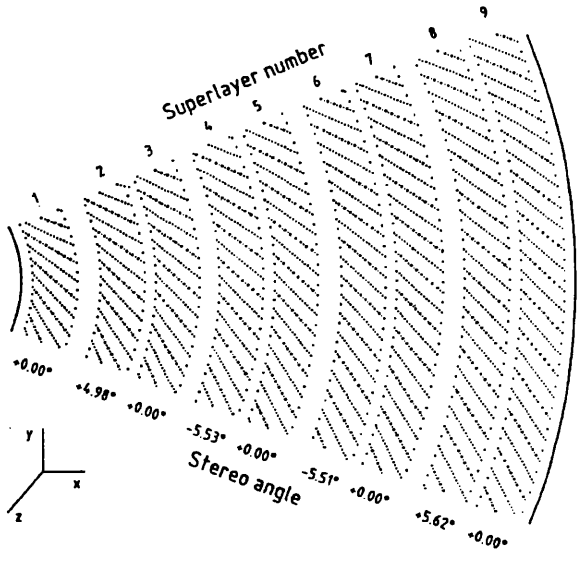

Figure 3.4: Diagram of one octant of the CTD.

parallel to the chamber axis (axial layers) and the rest have their wires at a small

stereo angle ($\theta \approx \pm 5°$), providing information on the z position of track hits. High voltage wires provide a uniform electric field, in addition to the magnetic field of the solenoid magnet, through which ions and electrons produced by charged particles can drift. The CTD chamber is filled with a mixture of argon, carbon dioxide and ethane gas. The nominal resolution for full length tracks in the CTD is 180μm in $r-\phi$ space, and at 90 deg to the z axis it has a momentum resolution of $\sigma(p)/p \approx 0.005p \oplus 0.016$ (GeV/c), where $\oplus$ means addition in quadrature.

3.2.3 Uranium Calorimeter

The ZEUS CAL is a high resolution compensating uranium scintillator sandwich calorimeter. The analysis presented in this thesis measures jets of particles, and these jets are measured in the CAL. The calorimeter is a *compensating* calorimeter, that is it has the same energy response to electromagnetic and hadronic showers. The solid angle coverage is 99.7% of the maximum possible 4π, making it almost completely hermetic. The energy resolution is

$$\frac{\sigma(E)}{E} = \frac{35\%}{\sqrt{E}} \oplus 2\%,$$

for hadrons, and

$$\frac{\sigma(E)}{E} = \frac{18\%}{\sqrt{E}} \oplus 1\%,$$

for electrons where the energy, E, is measured in GeV. The CAL is divided into three main parts, the FCAL, BCAL and RCAL. These are further subdivided into electromagnetic (EMC) and hadronic (HAC) 20×20 cm towers. The EMC towers have a depth of 25 radiation lengths or 1 nuclear interaction length, and the HAC towers have a depth of between 4 and 6 nuclear interaction lengths, such that 90% of all jets should deposit at least 95% of their energy in the CAL. Each EMC tower is further subdivided into 4 cells. Each HAC tower is approximately 20×20 cm and each EMC cell is approximately 5×20 cm. A typical FCAL module can be seen in figure 3.5.

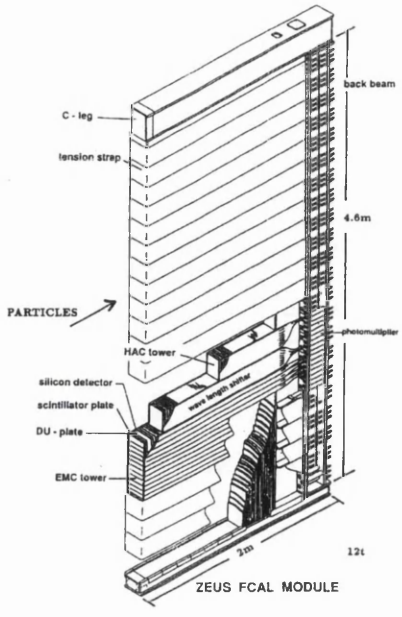

Figure 3.5: Cut-away view of an FCAL module.

Every HAC tower and EMC cell has alternating layers of depleted uranium and scintillator slices, and is read out by two photomultiplier tubes, coupled to the scintillator by wavelength shifters. By summing the energy recorded in the two photomultiplier tubes separately, it is possible to reconstruct the energy deposited in a cell independent of the impact position of the incoming particle.

The jets which are measured in the CAL have a well reconstructed position determination in the pseudorapidity range $-1 < \eta_{jet} < 2$. Given the beam energies, jets with a transverse energy above 5 GeV tend to be produced at high pseudorapidities, very few having $\eta_{jet} < -1$. Although the CAL extends to higher pseudorapidity, the granularity of the cells becomes a more important factor for $\eta_{jet} > 2$. More and more energy is deposited in fewer cells, and the position of that energy deposit is only known to be within the cell boundaries. For a jet which deposits its energy in many cells, the transverse energy weighted average of its position can be determined with good accuracy. This is the reason for an upper cut on η_{jet} which is mentioned later in chapter 5.

3.2.4 Luminosity Monitor

The luminosity measurement is important for all absolute cross section measurements, and is performed at ZEUS from the Bethe-Heitler process [31] $ep \rightarrow ep\gamma$. The electron scatters elastically off the proton, and the scattered electron and photon are produced at very small angles to the beam axis. To determine the luminosity, the scattered electron and photon must be measured. For a particular range of electron and photon energies, the number of such events are counted. Such events consist of an electron and photon detected for the same beam crossing, with measured energies summing up to that of the electron beam energy. The integrated luminosity $\mathcal{L}$ is related to the cross section

$$n = \mathcal{L}\sigma \tag{3.1}$$

where n is the number of events of this type of interaction. σ is calculated in QED, n is counted, and $\mathcal{L}$ is then determined.

Figure 3.6 shows the luminosity monitor. It consists of two small lead scintil-

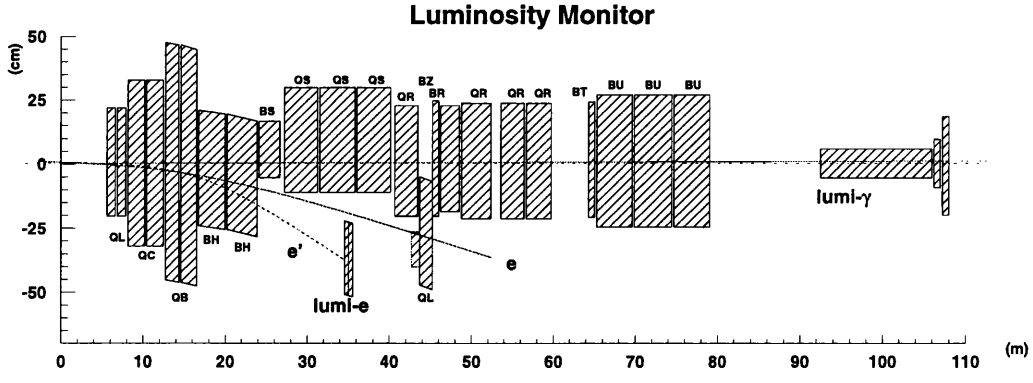

Figure 3.6: The luminosity monitor.

lator calorimeters, the electron calorimeter (LUMI-e) and the photon calorimeter (LUMI-γ). The position of the LUMI-e limits its acceptance to electrons with an energy between 0.2 and 0.8 of the beam energy. The energy resolution (measured in GeV) of this calorimeter is given by

$$\frac{\sigma(E)}{E} = \frac{18\%}{\sqrt{E}}$$

The LUMI-γ is situated at z = -104 m. It is protected from synchrotron radiation by a lead shield, which reduces the energy resolution (again in GeV) with respect to that of the LUMI-e to

$$\frac{\sigma(E)}{E} = \frac{25\%}{\sqrt{E}}$$

3.2.5 Beam Pipe Calorimeter

The beam pipe calorimeter (BPC) is a very small angle tungsten scintillator calorimeter designed to measure electrons. It is situated at the back of the RCAL ($z = -300$ cm), immediately adjacent to the beam pipe. It extends the Q^2 coverage to events with a Q^2 of approximately 0.1 - 0.6 GeV^2. It comprises two modules, north and south, so-called by virtue of their position with respect to the HERA coordinates. The thin tungsten and scintillator plates ensure frequent sampling and an energy resolution (in GeV) of the order of $15\%/\sqrt{E}$. The scintillator plates are segmented in the x and y directions such that the incident electron's position can be determined. To help with rejection of hadronic activity, a scintillator veto tile is positioned behind the BPC. Figure 3.7 shows a drawing of the BPC module and the rear beam pipe (for reference).

3.2.6 Small Angle Rear Tracking Detector

The small angle rear tracking detector (SRTD) is designed to improve the angular resolution on the scattered positron. It is situated on the face of the RCAL (see figure 3.7), covering an area of 68cm $\times$ 68cm around the rear beam pipe hole. It consists of two planes of scintillator strips, and each plane is divided into four 24cm $\times$ 44cm pieces. The strips have a width of 1cm each, and are oriented

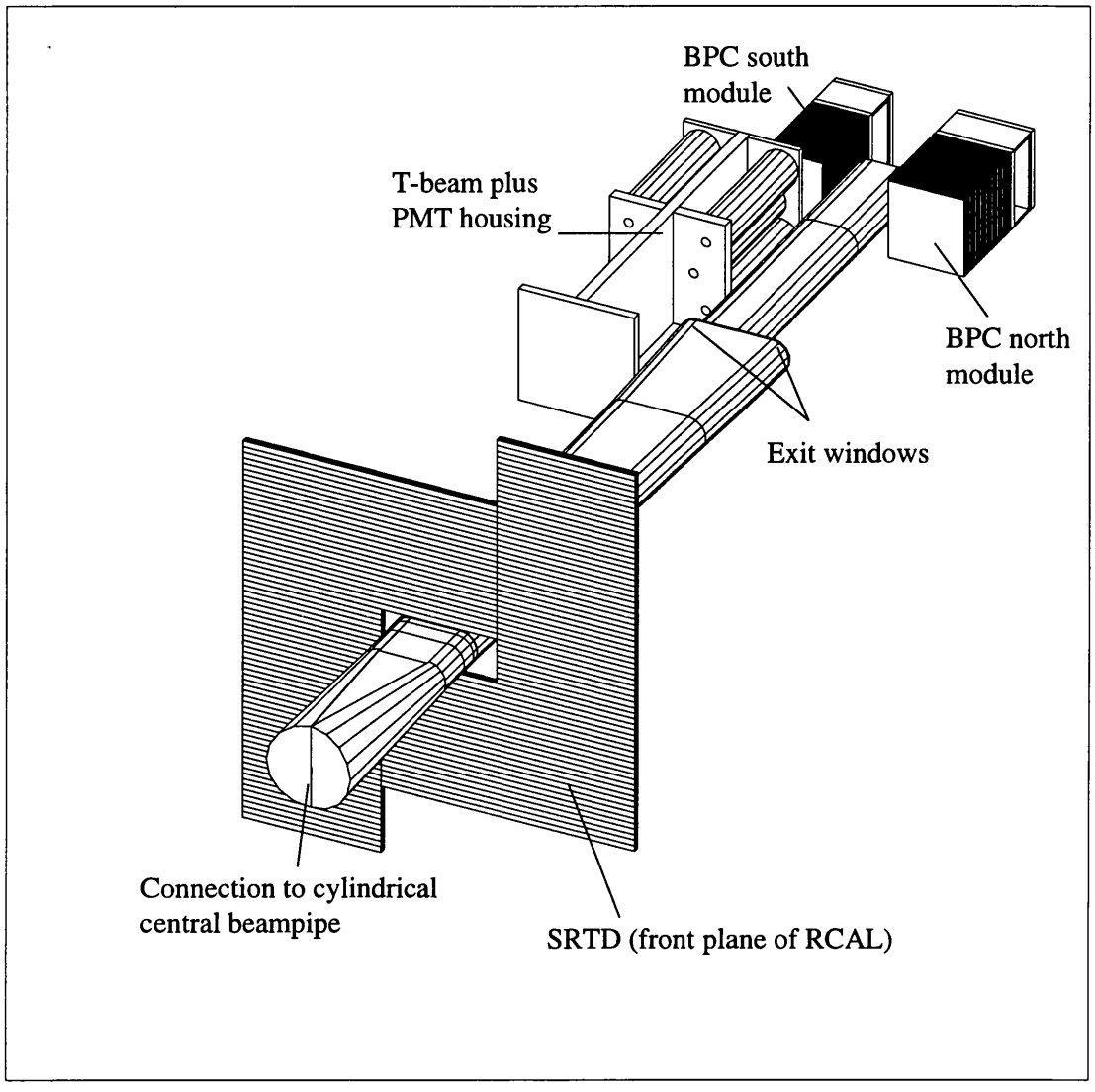

Figure 3.7: The beam pipe calorimeter, small angle rear tracking detector and rear beam pipe together with the exit windows. One example T-beam module, found at the back of the RCAL modules, is shown in front of the south module of the BPC, the others above and below the beam pipe and in front of the north module have been removed for clarity.

alternately along the x and y axes. It can achieve a position resolution of less than 5mm in x and y.

The improved angular resolution for positrons with low scattering angles is

beneficial for measurement of kinematic variables via the double angle method, the resolution being much better than that of the RCAL. If the scattered positron enters the RCAL close to the beam pipe, the energy deposited in the RCAL may not be the full energy of the positron due to leakage from the edges of the RCAL. With the SRTD's better position resolution, more accurate conditions on the scattered position of the positron can be imposed, such that events have a well contained, well measured positron energy. The SRTD can also improve the energy measurement of the scattered positron by measuring any showering of positrons in the inactive material (cables and flanges) in front of the RCAL. Such measurements can be used to calculate the energy lost in the inactive (or dead) material.

3.2.7 The ZEUS Trigger System

The nominal bunch crossing rate for HERA is $\sim$ 10 MHz. The data acquisition (DAQ) system can handle writing out data to tape at a frequency of only a few Hz. Most of the interactions are, however, dominated by non-ep interactions such as the proton beam interacting with residual gas, or cosmic ray interactions. Such events are generally not wanted for physics analysis. There are also unwanted ep processes such as soft photoproduction, which are not considered of interest at present.

In order to reduce the rate to less than $\sim$ 10 Hz, whilst efficiently selecting wanted ep interactions, ZEUS has a three stage trigger system which decides whether or not to write an event to tape. A schematic is shown in figure 3.8.

The trigger system is divided into three stages, each stage requiring more time and information than the previous to make a decision whether to keep the event or not.

- **First Level Trigger (FLT)** The rate is initially reduced to $\sim$ 1 kHz by the FLT, which is a hardware based trigger. Each component has its own

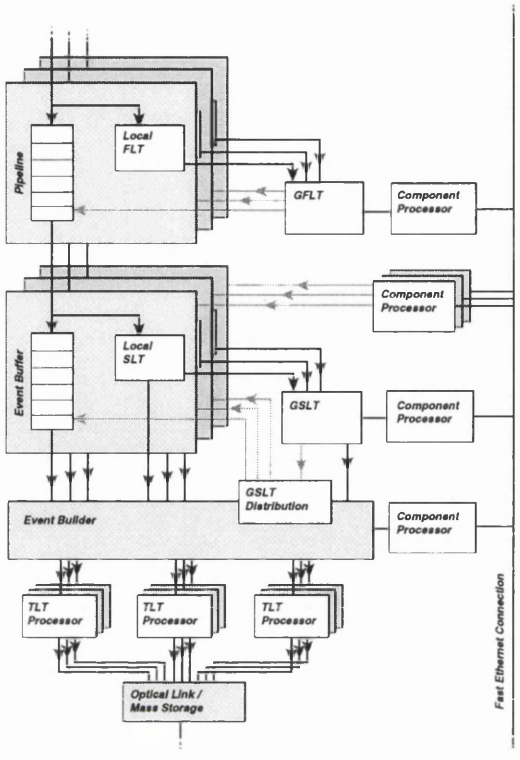

Figure 3.8: A schematic diagram of the ZEUS trigger system.

FLT and stores its data in a pipeline whilst waiting for a decision before passing that decision to the global first level trigger (GFLT) which makes a final decision on whether to pass the event on to the second stage, or ignore the event.

- **Second Level Trigger (SLT)** Events that have passed the FLT proceed to the SLT. This is a software based trigger, and is designed to reduce the rate by approximately a factor of ten. Similar to the FLT, each component has its own SLT, and a decision is made by the global second level trigger (GSLT).

- **Third Level Trigger (TLT)** Events passing the SLT are reconstructed by the event builder, which has access to the full event data taken by all

components, and provides a picture of the event which can be understood in terms of particle four-momenta. This information is passed to the TLT which has selection algorithms such as jet finding and electron finding algorithms. After the TLT selection procedure, the rate is down to less than 10 Hz, and these events are accepted and written to tape.

Figure 3.9 shows the trigger rates for the FLT, SLT and TLT between 1992 and 1997 as a function of luminosity. As the luminosity has increased from year to year, the trigger configuration has been changed in order to keep the end TLT rate below $\approx$ 10 Hz as required.

Final event reconstruction is performed offline using more sophisticated reconstruction routines and optimised calibrations, as compared with the TLT. The TLT is constrained by time, and hence cannot afford the time to implement such time-consuming reconstruction packages. This final reconstruction is the subject of the next chapter.

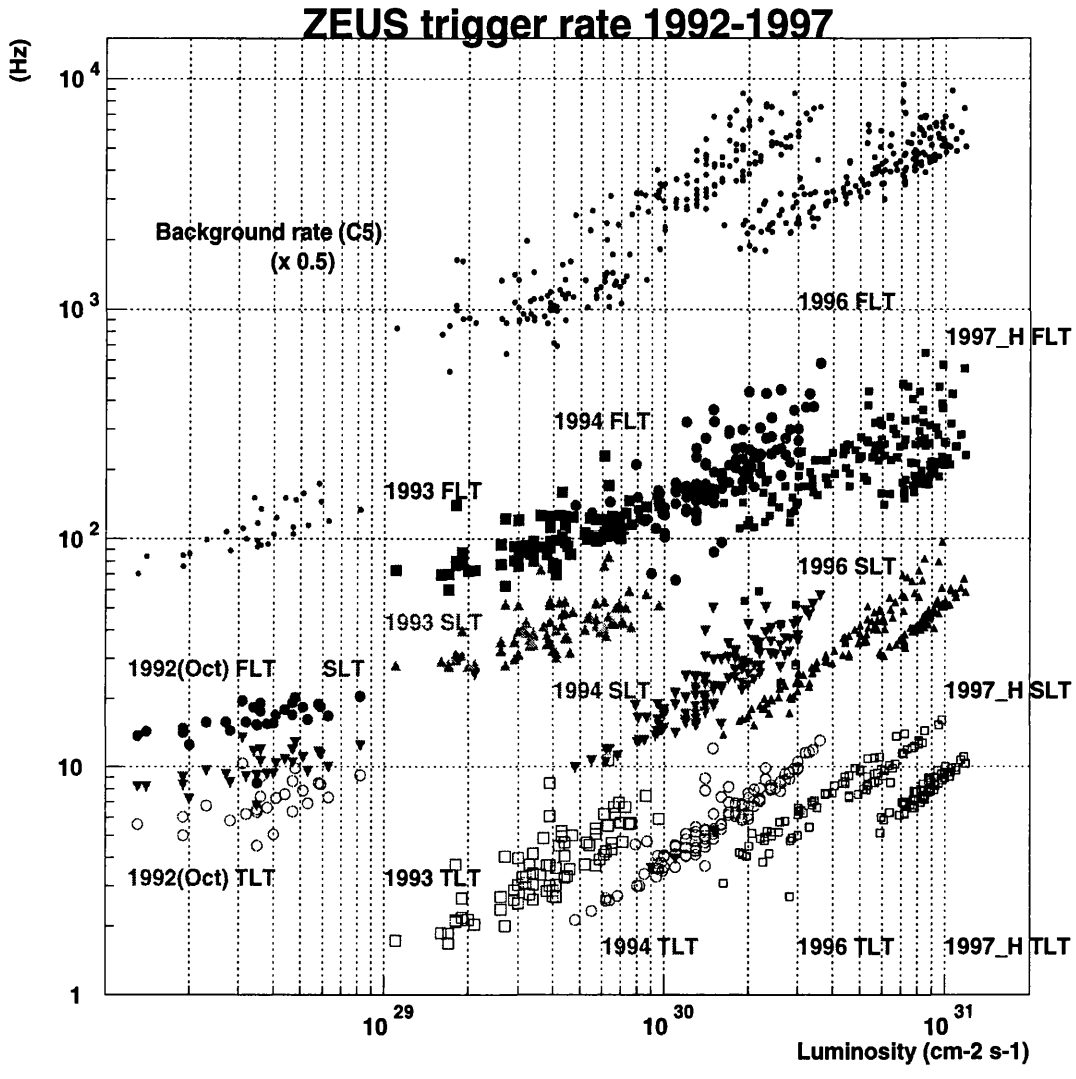

Figure 3.9: Trigger rates from the first, second and third level triggers as a function of luminosity and data-taking period. The different symbols indicate different data-taking periods and hence different trigger configurations.

Chapter 4

Data Reconstruction and Quality Checks

4.1 Offline Data Processing

The set of data that is written to tape after being filtered by the three level trigger system, contains "raw" information on each event. For example, the energies deposited in the calorimeter have no correction applied for any miscalibration of particular cells, the particle hits recorded in the CTD have not been fitted to form particle trajectories. The purpose of the offline data processing package is to reconstruct event quantities which are more useful quantities to work with.

All events that are on tape, having passed the TLT filter are reconstructed to provide event information in terms of the energy and/or momenta of the particles produced. At the same time, events which are deemed to be particularly interesting are flagged by means of a Data Summary Tape (DST) bit. In this way, an analysis can be performed by selecting one or more DST bits, to further refine the event selection with which the analysis is concerned. An example of a DST bit is one which selects events with two jets, with a transverse energy above some threshold, in a particular y range. Selecting only this event sample, is a

faster way to access dijet events, rather than running a jet algorithm on every event on tape.

The analysis and recording of the various physics processes accessible with ZEUS are the responsibility of five physics groups. Each group specialises in a subsample of such processes. The analysis presented in this thesis was carried out in the Hadronic Final States (HFS) group, which focuses on jet physics, photon structure and the QCD evolution of the initial to final event state. During the 1998 running period there were 25 DST bits, most of them having a very similar set of cuts to those of the the 27 TLT filters which the HFS group looked after.

All 27 HFS TLT filters require that each event has a reconstructed vertex, which is to say that the majority of the tracks in the event are required to originate from the same point to within certain parameters. For the HFS filters, the z position of this vertex is required to lie in the range -60cm $< z$ vertex $<$ 60cm. Another requirement is that $E - p_z < 75$ GeV. A brief description of the more important cuts required by these filters follows:

1. **Very High E_T (HPP01)** $E_T^{cone} > 25$ GeV, where E_T^{cone} is the transverse energy measured outside a cone of 10° around the FCAL beampipe.

2. **Inclusive jet (HPP02)** One or more cone jets, or jets of hadrons as defined by a cone-type algorithm (see chapter 5 for a detailed description), with $E_T^{jet} > 10$ GeV, $\eta^{jet} < 2.5$.

3. **High p_T track 1 (HPP03)** One or more vertex fitted tracks, where a vertex fitted track is one which has been associated as originating from the reconstructed vertex.

4. **High p_T track 2 (HPP04)** One or more vertex fitted tracks with $p_T > 2$ GeV, and an electron tagged in the electron LUMI detector with an energy $E_e > 5$ GeV.

5. **FNC Inclusive Jet (HPP05)** A hit in the Forward Neutron Calorimeter (FNC), which measures neutrons travelling in the direction of the proton beam, and one or more cone jets with $E_T^{jet} > 4$ GeV, $\eta^{jet} < 2.5$.

6. **Dijet FNC (HPP06)** A hit in the FNC and two or more cone jets with $E_T^{jet} > 4$ GeV, $\eta^{jet} < 2.5$.

7. **Inclusive Jet BPC (HPP07)** A hit in the BPC and one or more cone jets with $E_T^{jet} > 4$ GeV, $\eta^{jet} < 2.5$.

8. **Dijet BPC (HPP08)** A hit in the BPC and two or more cone jets with $E_T^{jet} > 4$ GeV, $\eta^{jet} < 2.5$. There is no lower limit on η^{jet} as jets tend to be boosted in the forward direction, and the distribution of η^{jet} tails off to approximately zero events with η^{jet} less than 2.0.

9. **Very High LRG (HPP09)** $E_T^{cone} > 11$ GeV and no energy in the region around the FCAL beampipe. This depletion of energy is the large rapidity gap (LRG) which is a signature of certain interesting processes.

10. **Dijet LRG (HPP10)** Two or more cone jets with $E_T^{jet} > 4$ GeV, $\eta^{jet} < 2.5$, and no energy in the region around the FCAL beampipe.

11. **Inclusive Jet LPS (HPP11)** A hit in the Leading Proton Spectrometer (LPS), which measures protons travelling in the forward direction (not beam protons, but those which have undergone a scatter), and one or more cone jets with $E_T^{jet} > 4$ GeV, $\eta^{jet} < 2.5$.

12. **Dijet LPS (HPP12)** A hit in the LPS and two or more cone jets with $E_T^{jet} > 4$ GeV, $\eta^{jet} < 2.5$.

13. **LRI (large rapidity interval) (HPP13)** Two or more cone jets with $E_T^{jet} > 4$ GeV, $\eta^{jet} < 2.5$ and $|\eta_1^{jet} - \eta_2^{jet}| > 3$

14. **(HPP14)** Two or more cone jets with $E_T^{jet} > 4$ GeV, $\eta^{jet} < 2.5$.

15. **Dijet high E_T (HPP15)** Two or more cone jets with $E_T^{jet} > 6$ GeV and $\eta^{jet} < 2.5$, or $E_T^{jet} > 4$ GeV and $\eta^{jet} < 1.5$.

16. **Prompt Photon (HPP16)** $E_T^{cone} > 8$ GeV and an electromagnetic energy cluster with $E_T^{elec} > 4$ GeV.

17. **High p_T track 3 (HPP17)** One or more vertex fitted tracks with $p_T > 4$ GeV.

18. **High p_T track 4 (HPP18)** One or more vertex fitted tracks with $p_T > 5$ GeV.

19. **High p_T track 5 (HPP19)** One or more vertex fitted tracks together with strangeness enhancement.

20. **DIS Forward Jet (HPP20)** One or more cone jets with $E_T^{jet} > 3$ GeV, $0.0 < \eta^{jet} < 3.0$ and an electron with $E_T^{elec} > 8$ GeV.

21. **DIS Dijet High Q2 (HPP21)** Two or more cone jets with $E_T^{jet} > 3$ GeV, $-3.5 < \eta^{jet} < 3.0$ and an electron with $E_T^{elec} > 6$ GeV.

22. **DIS Dijet alphas (HPP22)** Two or more cone jets with $E_T^{jet} > 3$ GeV, $-3.5 < \eta^{jet} < 3.2$ and an electron with $E_T^{elec} > 8$ GeV.

23. **DIS Dijet Low Q2 (HPP23)** Two or more cone jets with $E_T^{jet} > 4$ GeV, $-3.5 < \eta^{jet} < 3.0$ and an electron with $E_T^{elec} > 6$ GeV.

24. **DIS forward jet kt (HPP24)** One or more jets found with a clustering algorithm (kt jets), with $E_T^{jet} > 3$ GeV, $0.0 < \eta^{jet} < 3.0$ and an electron with $E_T^{elec} > 8$ GeV.

25. **DIS dijet kt High Q2 (HPP25)** Two or more kt jets with $E_T^{jet} > 3$ GeV, $-3.5 < \eta^{jet} < 3.0$ and an electron with $E_T^{elec} > 6$ GeV.

26. **DIS dijet kt alphas (HPP26)** Two or more kt jets with $E_T^{jet} > 3$ GeV, $-3.5 < \eta^{jet} < 3.2$ and an electron with $E_T^{elec} > 8$ GeV.

27. **DIS dijet kt low Q2 (HPP27)** Two or more kt jets with $E_T^{jet} > 4$ GeV, $-3.5 < \eta^{jet} < 3.0$ and an electron with $E_T^{elec} > 6$ GeV.

The DST bits mostly have a one to one correspondence with the TLT filters, but there are some exceptions. The mapping of DST bits to TLT bits is shown in table 4.1. Only 25 DST bits were allocated to the HFS group, so there could not be a one to one correspondence with the 27 TLT filters. TLT branches with similar quantities that are cut on, are OR'ed together, such as DST bit 20 which is an OR of the forward cone jet and forward kt jet TLT filters. Any analysis looking at forward jets may well choose this DST bit to select events, until a choice of jet finder is decided upon. Until then, both cone and kt jet finders could be used.

4.2 Data Quality Monitoring

There are a number of data quality checks performed from the moment the data is taken until the data is analysed offline. These serve to check whether all components are functioning properly, that the non-*ep* backgrounds such as beam-gas interactions are low, and the beam conditions are favourable for efficient *ep* interaction data taking. The HFS Data Quality Monitoring (DQM) graphs are produced during the offline reconstruction and are checked for each run. Because the reconstruction has already been carried out, higher level physics quantities (those closer to the actual quantities which one would select on in an analysis) can be checked, and runs with suspect distributions are flagged and can be eliminated from later analysis if necessary.

The plots in figure 4.1 are general plots to examine the beam conditions and response of the calorimeter. The quantities t_{FCAL} and t_{RCAL} are the average

DST Bit	TLT Slot(s)
1	1
2	2
3	3 OR 4
4	21 OR 23 OR 25 OR 27
5	5
6	6
7	7
8	8
9	9
10	10
11	11
12	12
13	13
14	14
15	15
16	16
17	17
18	18
19	19
20	20 OR 24
21	1 AND require $E_T > 50$ GeV
22	15 (prescaled by 100) OR 13
23	6 OR 8 OR 16 OR 17
24	OR of all TLT bits 20 through 27
25	22 OR 26

Table 4.1: The DST to TLT mapping.

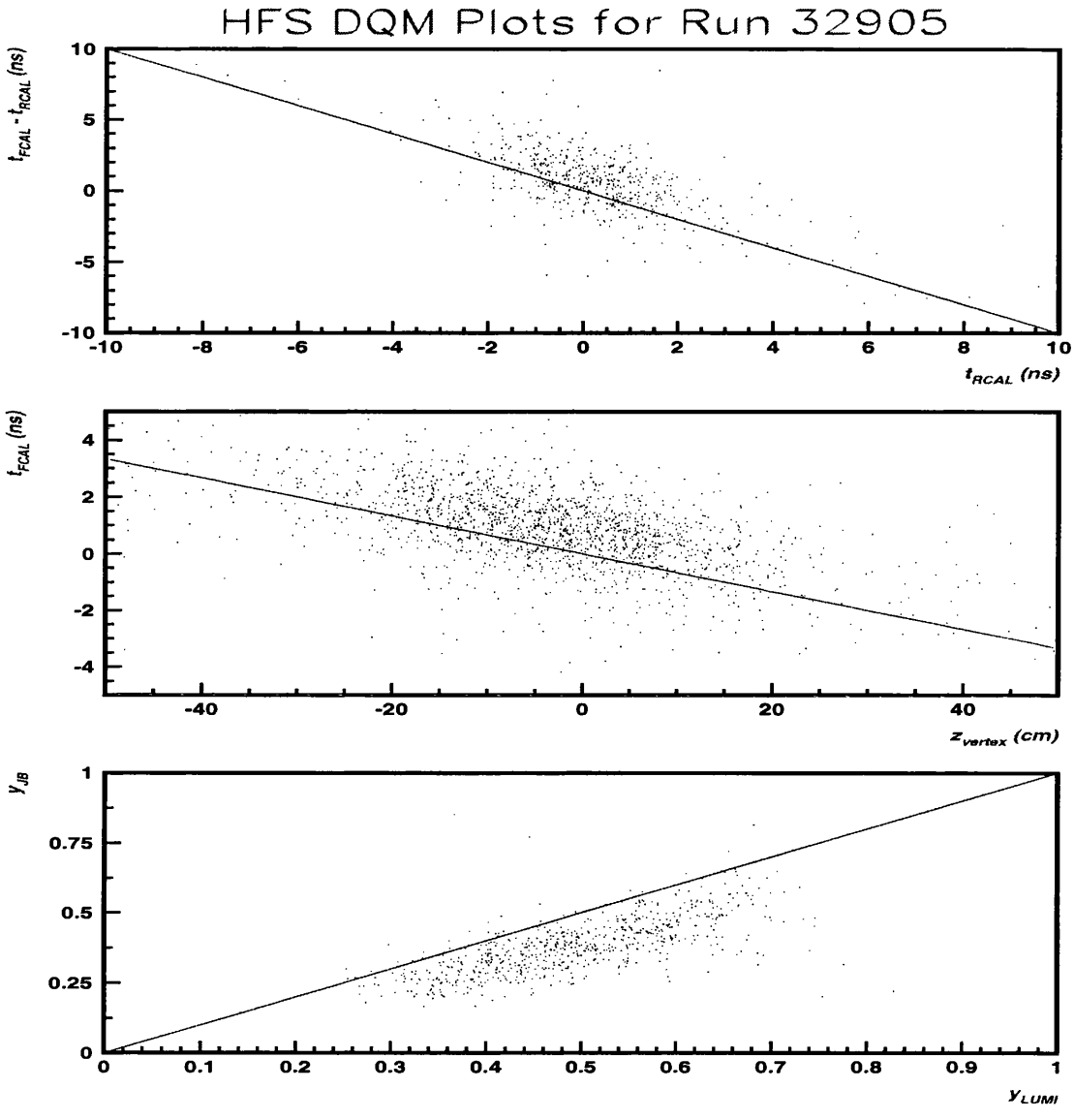

Figure 4.1: General DQM plots of $t_{FCAL} - t_{RCAL}$ vs t_{RCAL}, y_{JB} vs y_{LUMI} and t_{FCAL} vs z vertex.

times for particles to reach the FCAL and RCAL respectively. These times are calibrated such that particles from the nominal interaction point ($z = 0$ cm) hit the FCAL and RCAL at time $t = 0$ ns. The two quantities are correlated, as can be seen from the first plot of figure 4.1, and are expected to lie along the line drawn on the plot. A good run will have most events clustered around the

origin. If there were significant numbers of proton beam gas interactions written to tape, they would show up as a cluster of events at the top left corner of the plot, since such events generally occur upstream of the nominal Interaction Point (IP). If the FCAL and RCAL are well calibrated, then all events, beam gas or good *ep* events should lie on the line. If there is a significant deviation from this line, then the calibrations are off.

The second plot of figure 4.1 is useful as a check of timing versus z vertex. These two quantities are also correlated, again a line is drawn on the plot to show where the correlation is expected to be. If the calibration of t_{FCAL} is off, the points will not lie on the line. The cluster should be centred at the origin. If not, then this implies that the collisions are not occurring at the IP. As long as this is within ± 10 cm of the IP, this is considered acceptable.

There are two methods of measuring y which are shown in the third plot. They are using the electron which is measured in the LUMI detector, y_{LUMI} (see equation 1.4), and the Jacquet-Blondel estimator, y_{JB} (see equation 1.5). Given perfect measurement, these events would lie on the line $y_{JB} = y_{LUMI}$. Due to dead material between the IP and the calorimeter, the hadrons lose energy, and y_{JB} typically underestimates the inelasticity. This plot is a good check to see if such quantities can be calculated using the calorimeter or the LUMI tagger independently. If either component is not functioning properly, it will show up here.

Figure 4.2 shows an example plot of the bunch crossing number (BCN) for a selection of filters. Each bunch crossing is assigned a number, and is plotted here. There are gaps in the number sequence where electron or proton bunches are left unpaired to estimate the contribution from non-*ep* background interactions. The gaps demonstrate that the numbers of such background events is small.

The z vertex distribution shows where the mean interaction occurs, and this is expected to be within ± 10 cm of zero. The width of the distribution provides information on how consistent the vertex is with time. Satellite bunches are

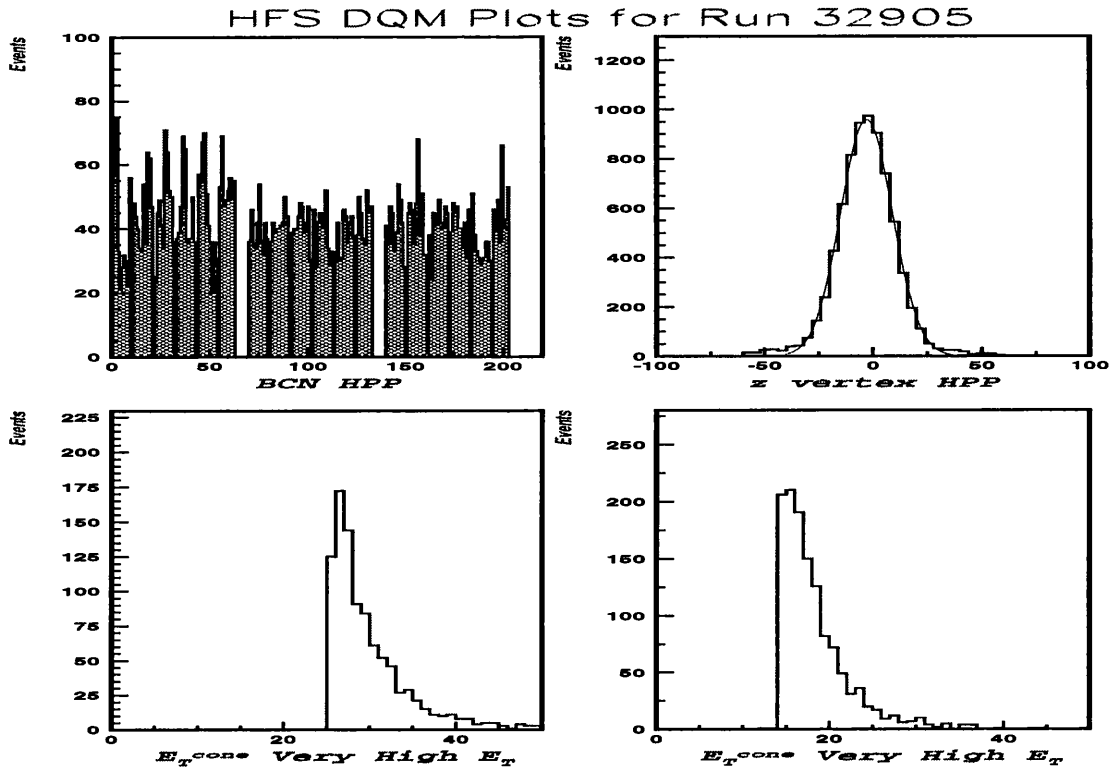

Figure 4.2: Plots of the bunch crossing number (BCN), the z vertex (in cm) for particular filters, and the total E_T (in GeV) measured outside a cone of 10° around the FCAL beampipe for two different DST bits.

bunches of protons which coast with the proton beam, and occur due to not being well confined within their own bunch parameters. They then interact at a different point, typically at a z of about 60 cm. This will show up as a secondary peak at $z \approx 60$ cm. Runs are checked to see whether or not such contributions from satellites are small.

Other plots such as the total E_T measured outside a cone of 10° around the FCAL beampipe are checked for each DST bit. An example of such plots from two different DST bits is shown in figure 4.2. Many of the filters have a cut on this quantity, and so it is advisable to check that the cut is working properly. Similarly for the p_z/E and $E - p_z$ quantities (figure 4.3) the shapes are checked as well as any cut expected.

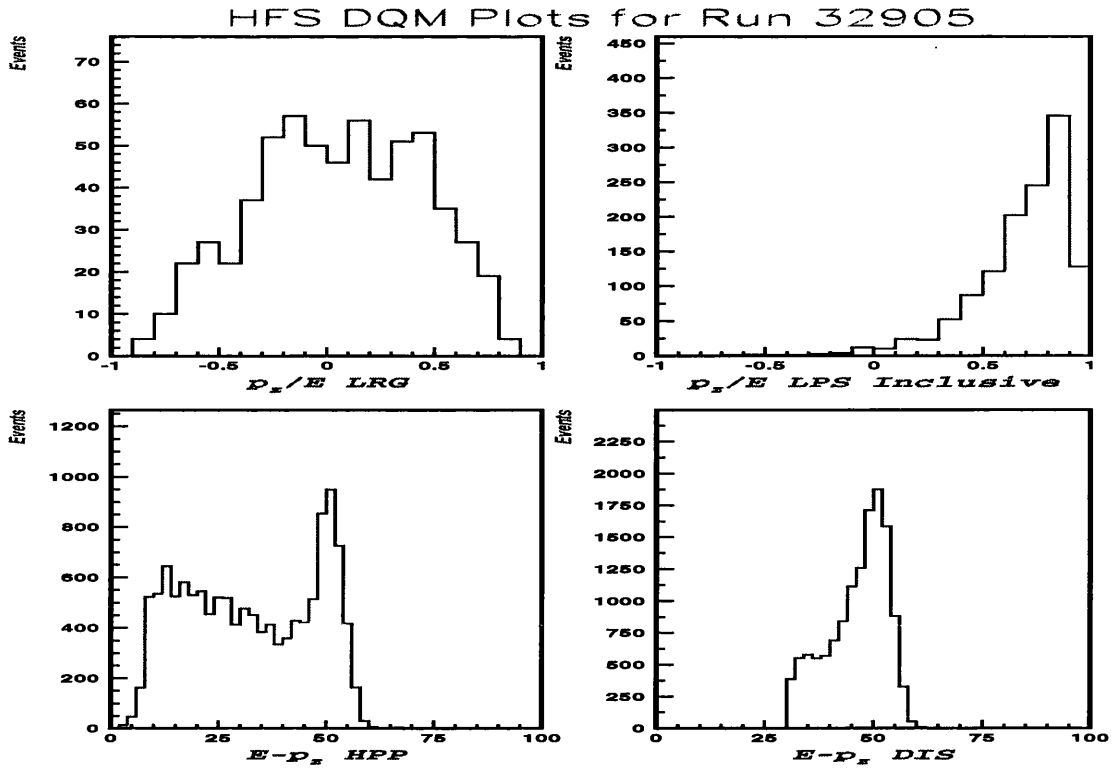

Figure 4.3: Plots of p_z/E and $E - p_z$ (in units of GeV) for particular filters.

As DQM expert for the HFS group, I coordinated and implemented the procedures to monitor the quality of the data to be used by our group. Any problems with runs were reported centrally and listed in the form of a table versus run number. Using this table, members of the group could veto any runs from their analysis which they regarded as having a problem which would affect their results. For my analysis, one of the ZEUS components extensively used is the BPC. If there were problems with the data measured by the BPC, I would have to decide if the problems were serious enough to exclude this run from my data sample. In contrast, those analyses which did not look at any data taken by the BPC would not be affected, and would not exclude a run for this reason.

Runs which were checked by our group had already passed through the offline reconstruction procedure. This meant that most runs which might have had large

problems, such as, for example, if the CTD was not functioning properly, would already have been flagged as a "bad run" and excluded from physics analyses. As a consequence, almost no runs which were checked by our group were flagged as being "unusable" for the HFS group in the period 1996-1997. Every run which has come through the offline reconstruction is checked on the same day as the reconstruction finishes in order to pick out any problems as soon as possible. Any problems which arise are immediately reported such that they can be promptly fixed, and more good quality data can be taken than if these checks were not done.

Such procedures help to ensure that the data that is analysed is not subject to bad beam conditions, or poor detector performance. The analysis presented here selects events based on a dijet filter. This means that the event sample is reasonably clean, that is good *ep* dijet events. Further selection cuts will be applied to access the particular event sample required, and these are discussed in detail in the next chapter.

Chapter 5

Jet Finding and Event Selection

The cross sections measured are defined in terms of Q^2, y, x_γ^{obs}, E_T^{jets} and η^{jets}. The selection criteria are designed to be those which select a relatively pure sample of dijets which lie in that region of phase space defined by the afore-mentioned variables. An event sample having passed the loose DST bit filter cuts, is then further refined by these selection cuts. As mentioned in chapter 1, the cluster of hadrons which is termed a jet is dependent upon the algorithm used to assign such hadrons to be part of that jet, and so this algorithm forms part of the cross section definition.

5.1 Jet Finders

Two types of algorithms are commonly used at ZEUS to determine the jets in an event. These are cone algorithms and cluster algorithms. Cone algorithms are usually faster to implement, and are typically what are used at the TLT filter stage, where speed of event processing is more important. Cluster algorithms are more CPU intensive, but depending on the rate that a TLT filter will accept events, such algorithms can and are used at the online TLT stage. The two most common jet finders used are EUCELL (a cone type algorithm) and KTCLUS [32] (a cluster based algorithm).

A jet finder is used to access information on the outgoing partons from a hard QCD process. These initial partons are not measured, but rather the jet of hadrons they produce is what is detected. There is a correlation between the four-momenta of the partons in the event and the jets of hadrons, but it is not perfect. The hadrons that are measured in the detector come not only from the partons exiting the hard subprocess, but also from the beam remnants. Typically the dijet samples examined have the proton contributing a small fraction of its momentum to the hard subprocess, the rest being carried off by the remnant towards the FCAL and the forward beam pipe. In identifying jets from the hard subprocess, it is preferable to have as little contamination from remnants, and so the jet finders must have some feature which reduces this contamination.

The partons which collide to produce the jets in an event at HERA are generally not of equal and opposite momentum. This means that the jet system which is measured is subject to a variable boost from the centre of mass frame of those jets. A desirable feature of a jet finder is then one of being independent of such a boost. In the photoproduction limit, this is achieved as the boost from the incoming partons' centre of mass frame to the lab frame is one along the z axis. As mentioned in chapter 1, the E_T and ϕ of the jet are invariant under such a boost, whereas the η of the jet is shifted by an additive constant. Hence, the form of the transverse energy distribution in $\eta - \phi$ is the same for all frames. As the photon virtuality is increased, the photon has some initial transverse momentum with respect to the z axis, and the preceding argument starts to break down. This nice boost-invariant feature begins to disappear, and can only be regained by transforming the event to a frame where the photon and proton are incoming along the z axis again. This is true for the Breit frame and the photon-proton centre of mass frame, and such frames could then be more advisable to use for DIS events.

Two other desirable features to have in an algorithm are collinear and infrared safe criteria. The algorithm is collinear safe if no distinction is made between a

single particle with energy E, and two collinear particles whose energies sum to the same value ($E_1 + E_2 = E$). If the results of the jet finder were very sensitive to this, then results would depend largely on the granularity of the calorimeter cells. To be infrared safe, the algorithm's results must not be highly sensitive to the emission of low energy particles.

A more detailed discussion of the advantages and disadvantages of the EUCELL and KTCLUS algorithms and how they deal with the above issues can be found elsewhere [33], so only a brief discussion of both is presented here.

5.1.1 EUCELL - Cone algorithm

EUCELL is a cone algorithm, which conforms to the standards set by the 'Snowmass Convention' [34]. This convention defines the transverse energy and coordinates of the jet to be

$$E_T^{jet} = \sum_i E_{t,i}$$

$$\eta^{jet} = \frac{1}{E_T^{jet}} \sum_i E_{t,i}\eta_i \tag{5.1}$$

$$\phi^{jet} = \frac{1}{E_T^{jet}} \sum_i E_{t,i}\phi_i$$

where the sum runs over all particles (or measured energy deposits in the calorimeter cells in the case of determining measured data jets) within the cone defined by a given prescribed radius, R, in $\eta - \phi$ space. In EUCELL, clusters are determined using a grid in $\eta - \phi$ space. The size of the cells that make up the grid is determined such that $\Delta\eta^{gridcell} \approx \Delta\phi^{gridcell} \approx R/2$. By then sliding a 3×3 cell window over the grid, a potential pre-cluster is formed. To be called a pre-cluster, it must be above some prescribed transverse energy (the seed transverse energy). A cone of radius R is then placed around the pre-cluster. The procedure is iterated until no more pre-clusters satisfying the seed transverse

energy requirement are found. The first jet is defined as the cone with the highest transverse energy. The cells attributed to this cone are then removed from the grid, and successive jets are determined from the remaining objects by the same procedure until there exist no more cones containing transverse energy above a certain energy threshold.

Such an algorithm can be run with an upper pseudorapidity cut on the jets found, so that very little, if any, proton remnant is included in the jets found. The algorithm is collinear safe, but not infrared safe. Low energy radiation between two cone jets could lead to the seed transverse energy threshold being crossed at a different location in $\eta - \phi$ space, and the found jets will then be very different. The starting point for the seed finding (pre-clustering) in $\eta - \phi$ space is user-defined, and not therefore a universal definition, and again jets found will depend on the initial input by the user. For these reasons, this type of algorithm is less favoured with respect to KTCLUS, which does not suffer from such ambiguities.

5.1.2 KTCLUS - Clustering algorithm

KTCLUS finds jets by merging particles together that satisfy some condition. To do this, "distance" parameters are determined, to determine which particles will be merged, together with a recombination scheme which defines how they will be merged. The particular recombination scheme used in this thesis is the inclusive recombination scheme of Ellis and Soper [35] in a mode which is invariant under longitudinal boosts. The algorithm scheme depends on a parameter R and is analagous to a cone radius.

One distance parameter

$$d_i = E_{T,i}^2$$

is defined for each particle, i. Another distance parameter is defined for each pair of particles, i and j as

$$d_{ij} = \min(E_{T,i}^2, E_{T,j}^2) \left[(\eta_i - \eta_j)^2 + (\phi_i - \phi_j)^2\right] / R^2.$$

For particles close to the beam axis, d_i is the limit of the "distance" between particle i and a large mass remnant travelling along the z direction.

If the smallest distance parameter is d_{ij}, then particles i and j are merged into a single particle. If the smallest value is d_i then this particle is considered "complete" and is removed from further clustering. This process is then repeated until all the objects have been removed, producing an E_T ordered list of objects.

This algorithm retains invariance under longitudinal boosts as each quantity E_T, $\Delta\eta$, $\Delta\phi$ in the distance parameters are all invariant under longitudinal boosts. Because d_i is the limit of the distance between particle i and a large mass remnant travelling along the z direction, most proton remnant particles tend to be clustered together and are not included in higher E_T jets. The algorithm is a well defined procedure, which does not depend upon the order in which the algorithm runs through the list of particles. This rigorous definition of which jet each particle belongs to, makes the algorithm infrared and collinear safe [36].

For these reasons, KTCLUS is the preferred jet finding algorithm and the one used for this analysis.

5.2 Event Selection

The event samples used in this analysis are those produced by the 1996 and 1997 HERA running period and collected with the ZEUS detector. The ZEUS detector was reasonably stable for this whole period, no extra components were added or removed that would affect the data relevant to this analysis to any large extent. Hence the whole data set can be treated as one entity, rather than having to split the sample into several parts. The integrated luminosity collected and used in this analysis amounts to 38.1 pb^{-1}.

In order to examine the structure of the virtual photon, cross sections are measured with respect to variables which are sensitive to this structure. These variables are Q^2, y, x_γ^{obs}, E_T^{jets} and η^{jets}. A sample of events must then be selected such that these variables can be accessed, and the measured quantities can be reasonably well measured.

The first requirement is a dijet sample, since without two or more jets, x_γ^{obs} is not defined. The two jets must have a transverse energy above some threshold, and pseudorapidities in a certain range, where the jets can be confidently measured. The inelasticity, y, can be measured using the scattered positron, or via the hadronic system to calculate the estimator y_{JB}. If the scattered positron is not tagged, and travels down the rear beam-pipe, having scattered at a very small scattering angle with respect to its original direction, then it becomes necessary to use y_{JB} to estimate the inelasticity. In such a case the photon produced that enters the hard subprocess is quasireal, $Q^2 \approx 0$ GeV^2. If the scattered positron is measured in the BPC or in the calorimeter, then Q^2 can be calculated from the positron measurements.

For consistency, y_{JB} is always used to estimate the inelasticity, even though its resolution is worse than using the scattered positron information, when it is measured in a subcomponent. The inelasticity also enters into the x_γ^{obs} definition (see equation 1.9). The resolution of y_{JB} is similar to that for the jet measurements, since both rely on the hadronic system as measured in the calorimeter. Any systematic mismeasurement due to the hadronic bias of the calorimeter (see for example figure 7.1 in chapter 7) tends to cancel in this ratio of $(E - p_z)_{jets}$ to $(E - p_z)_{hadrons}$ in the x_γ^{obs} calculation. If the scattered positron were used to calculate y, the ratio would suffer from not being consistently mismeasured in both numerator and denominator.

To examine how the photon structure changes with photon virtuality, the event selection is separated into three parts. First, a photoproduction (or untagged) sample of quasireal photons, where the scattered positron is not

detected and assumed to have travelled down the rear beam-pipe. Second, a BPC sample, where the scattered positron is measured in the BPC. The range of virtualities accessible using this sample is $0.1 < Q^2 < 0.55$ GeV^2. Third, a DIS sample, where the scattered positron is measured in the main calorimeter. In this sample the range has a lower limit of $Q^2 > 1.5$ GeV^2.

Some of the selection cuts are common to all three samples, and these are outlined below. The more specialised cuts concerning the different Q^2 samples will be described later. To begin with, all data which are available on tape have been accepted by the ZEUS trigger system. This constitutes the initial online selection cut. The triggers in use are optimised for various physics processes, and the events required here are good dijet events, whether the scattered positron is detected or not. Hence, a particular trigger path is chosen, which should accept such events. Given this well-defined path, the efficiency of the trigger can be corrected for, if it is not 100% efficient, although it is desirable to have a trigger path which *is* 100% efficient for the selection cuts imposed. As an example, most of the dijet filters at the TLT accept dijets found using a EUCELL type algorithm. This does not mean that it will be totally efficient at accepting dijet events as defined by KTCLUS. This must be corrected for, and can only be done so if a well-defined trigger path is imposed. The particular triggers used in this analysis were stable for the data-taking period which constitutes the data sample used and are described in the following sections.

5.2.1 First Level Trigger

The First Level Trigger (FLT) choice is a particular trigger which is based on the requirement of a minimum amount of calorimeter energy to be present. To this end, at least one of the following conditions must be met

- The total calorimeter energy excluding the three innermost rings of cells in the FCAL and the innermost ring of the RCAL is greater than 15.0 GeV.

- The total EMC energy excluding the three innermost rings of cells in the FCAL and the innermost ring of the RCAL is greater than 10.1 GeV.
- The BCAL EMC energy is greater than 3.4 GeV.
- The RCAL EMC energy excluding the innermost ring is greater than 2.0 GeV.

Additional timing information from the C5 counter and Veto Wall detectors (situated upstream with respect to the proton beam direction) is used to reject events where the timing is not consistent with having come from an *ep* interaction. The number of beam gas interactions written to tape are reduced in this way.

5.2.2 Second Level Trigger

The Second Level Trigger (SLT) has more time to make a decision on whether to accept an event than the FLT, and so finer selection cuts using more complex algorithms are applied here. The analysis requires two high transverse energy jets, and this trigger is based on a transverse energy cut of at least 8 GeV, measured in the calorimeter, excluding the innermost ring in the FCAL. At this stage some vertex information is required from the CTD. If no such information exists, the vertex is assumed to be at the nominal vertex of $(x, y, z) = (0, 0, 0)$. Further selection cuts are now imposed here, these being

- The total energy minus total z momentum [1], both summed over all calorimeter cells, $E - p_z > 8.0$ GeV. Beam gas events typically deposit energy mainly in the forward direction, giving a low value for $E - p_z$. Fewer such events are accepted to tape by virtue of this cut.

[1]The particles measured in the calorimeter are assumed to be massless, since their mass is negligible in comparison with their energy. Hence $E - p_z = E(1 - \cos\theta)$ where θ is the angle the particle trajectory makes with the positive z axis.

- -60 cm < z (vertex) < 60 cm. Good ep interactions are centred about $z = 0$, unlike beam gas interactions which can occur anywhere.

- The average RCAL time is required to be within ± 8 ns of the nominal interaction time, and the difference between the average FCAL time and RCAL time must be also be within ± 8 ns. Such timing requirements are imposed for similar reasons as the z (vertex) requirement. Particularly when there is no vertex information, the timing cuts are effectively performing a vertex cut, since the vertex and timing are correlated quantities.

- The time at the top of the BCAL minus the time at the bottom of the BCAL must be greater than -10 ns. This rejects downward travelling cosmic muon events which leave energy behind in the calorimeter.

5.2.3 Third Level Trigger

The Third Level Trigger (TLT) is based on selecting dijets. It does this by applying a modified EUCELL jet finding algorithm to select events with two or more jets of transverse energy greater than 4 GeV and pseudorapidity less than 2.5. At this point there is some track reconstruction, although not as refined as the offline track reconstruction, due to speed requirements. As well as the dijet requirement, there are yet further refining selection cuts.

- The average RCAL time is required to be within ± 6 ns, the difference between the average FCAL time and RCAL time must be be within ± 8 ns, and the average global time must be within ± 8 ns. This reduces beam gas interactions contaminating the dijet sample.

- The average FCAL time must be within ± 8 ns to remove cosmic muon events in the FCAL, and positron interactions with beam gas.

- -60 cm < z (vertex) < 60 cm. This is a tighter cut than the SLT cut, as there is more tracking information now available.

- The number of bad tracks must be less than 6. A bad track is defined to be a well reconstructed track which points forward and extrapolates back to an origin at $z < -75$ cm. Such tracks are consistent with beam gas interactions.

- The total $E - p_z$ must be less than 75 GeV. A well contained event should have an $E - p_z$ of around twice the positron's initial energy. For 27.5 GeV positron beams, this means an $E - p_z$ of approximately 55 GeV. There is of course a resolution on this value, leading to some events being measured to have an $E - p_z$ of more than 55 GeV. Looking at figure 5.1, most of the events are not well contained, and this is due to the scattered positron going down the beam pipe, and not therefore contributing to the total $E - p_z$. Those events which are found to contain the scattered positron then form the secondary peak at ≈ 55 GeV, the spread to values other than 55 GeV being due to mismeasurement effects. The cut at 75 GeV does not remove any of these events, which all have an $E - p_z$ of less than 65 GeV, so no good events are wasted, yet the cut is sufficient to remove any event which is clearly an overlay of two or more different events (two or more events occurring at the same time).

5.2.4 General Selection Cuts

Given the trigger selection procedure, a sample of dijets with loose selection cuts has been obtained. Further offline cuts are now applied to increase the purity of the sample, such that most events are good dijet events and have as few beam gas or non-*ep* events as possible. Online the decisions are made within the time restrictions for writing data to tape. The finer calibrations that are performed during the offline reconstruction are not available for the trigger selection. Hence the further offline cuts are more accurate, and so increase the purity.

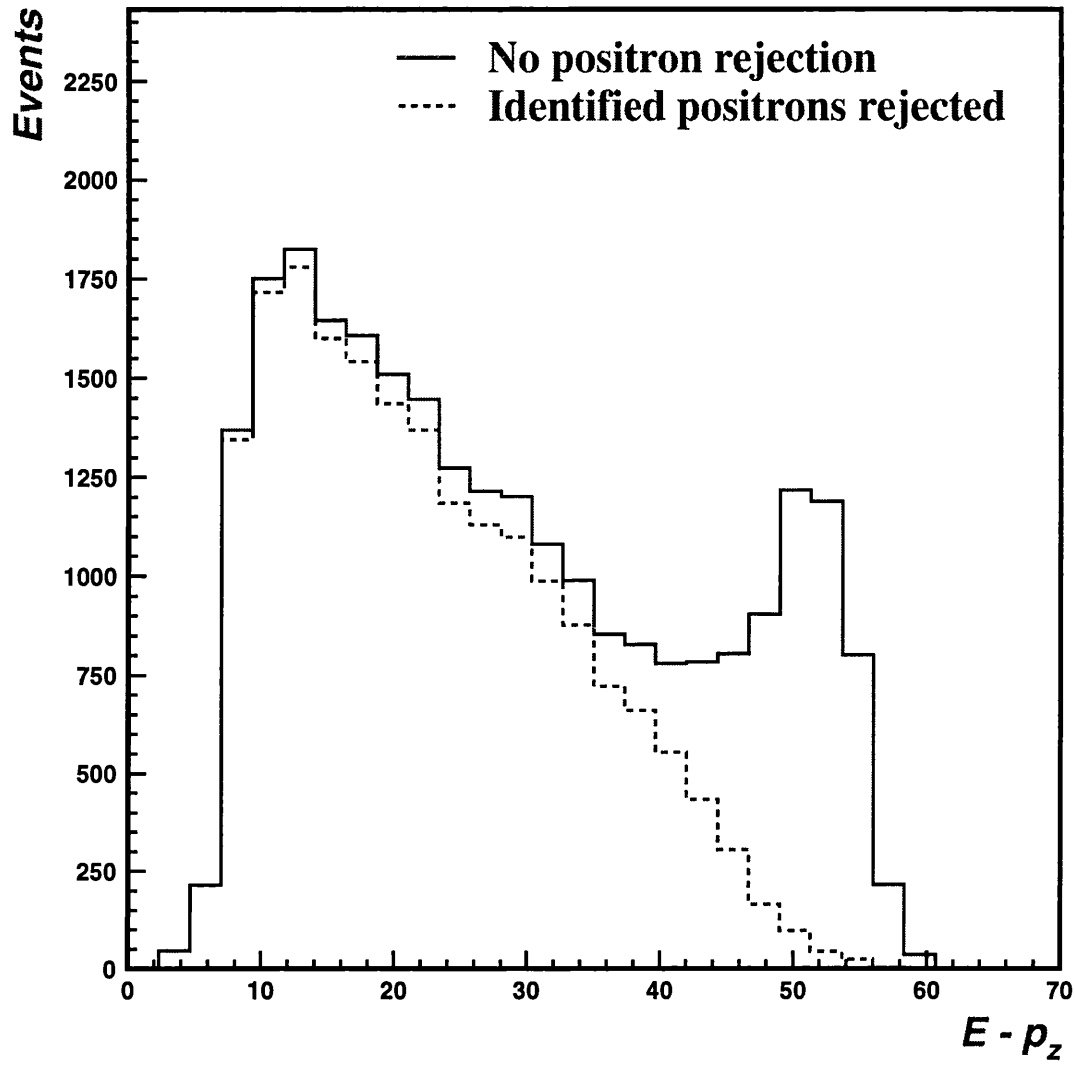

Figure 5.1: $E - p_z$ (in GeV) as measured with the ZEUS detector for a sample of events passing the third level trigger. The dashed histogram has any identified positrons removed.

Stricter timing cuts and vertex cuts are applied to remove cosmic events and beam gas interactions. The difference between the average FCAL time and RCAL time must be within ± 6 ns and the average RCAL time must be within ± 6 ns. The z (vertex) is restricted to be within ± 40 cm of the nominal interaction point. Before cuts are made on calorimeter quantities, corrections for noise and energy scale are made. The calorimeter has a number of cells which are known to be

"noisy", and produce signals even when no energy has been deposited in the cell. This is corrected for by standard year-dependent routines which remove noisy cells from the energy deposit records [37]. There are differences between the absolute energy scale as measured using the data, and Monte Carlo simulated events. This is corrected for by a standard routine [38] which scales all BCAL energies in the data up by 5% and scales the RCAL energies in the data depending on where the cell is located within the RCAL. The average RCAL scaling factor is 2.5%. The FCAL is consistent with the Monte Carlo and is therefore not scaled at all. The inelasticity, y, is restricted to be in the range $0.2 < y < 0.55$. Due to the measurement performance of the detector, this corresponds to a y_{JB} range, as measured by the detector, of $0.15 < y_{JB} < 0.45$ (recall figure 4.1 and the accompanying discussion). Beam gas interactions typically have a lot of hadronic activity in the forward direction (near the FCAL beam pipe). Such an event will have a low value for y_{JB} and the lower cut at 0.15 helps remove such events from the sample. The upper cut at 0.45 is based on detector acceptance for the BPC sample, and will be discussed more fully later.

To obtain two well measured jets of hadrons, the jets found are required to have a pseudorapidity between -1 and 2. The highest transverse energy jet must have a transverse energy greater than 6.5 GeV and the second highest greater than 5.5 GeV (as measured by the detector). Due to loss of energy in dead material inside the detector, these jets generally lose approximately 1 GeV of transverse energy before being measured in the calorimeter, hence their actual energies are greater than 7.5 GeV and 6.5 GeV respectively. The pseudorapidity is, however, largely unaffected. Having asymmetric transverse energy cuts, rather than two jets with the same cuts, is based on theoretical grounds. When calculating cross sections which contain two jets of the same E_T, soft gluon emission which accompanies jets leads to singularities, and cannot therefore be calculated [41]. For this reason, an asymmetric cut is made such that theory can compare to the measured cross sections.

A further cut on x_γ^{obs} is made such that $0.0625 < x_\gamma^{obs} < 1.0$. The reason for this is that after the above cuts, there are no events found in the data below an x_γ^{obs} of 0.0625. There must be a lower limit which is not zero, since an x_γ^{obs} of zero would imply that the photon had not input any energy into the dijet system. Without that, the dijets would not have any transverse energy and fail the E_T cut. Quoting a cross section in a region of phase space outside kinematical limits brings down the average cross section. Hence the cut ensures that cross sections are not underestimated.

The remaining cuts that are applied are specific to the Q^2 range that is accessed with the event selection. Since Q^2 is measured with respect to the scattered positron, the final selection cuts pertain to the positron measurements.

5.2.5 Photoproduction Sample

The photoproduction sample requires no scattered positron to be found in the main calorimeter, so as to eliminate DIS candidate events. This ensures that $Q^2 < 1.0$ GeV^2, and due to the form of the Q^2 distribution the bulk of such events are at $Q^2 \approx 0$ GeV^2. The electron finding routine used in this analysis to identify positrons is SINISTRA [39], which is a neural network trained to identify positrons or electrons. It uses calorimeter information and tracking information from the CTD when possible. The electromagnetic energy deposit expected in the calorimeter from a scattered positron should also have a charged track pointing to it, if the track falls within the acceptance of the CTD. Similar looking objects such as photons which also deposit electromagnetic energy into the calorimeter, would not produce a track in the CTD since they are not charged particles. Studies have been performed to check the efficiency of positron identification, and the efficiency for finding positrons with an energy above 10 GeV is almost perfect [40]. If no positrons are found, the event is kept. If a positron is found, it must be decided whether or not it is the scattered positron which produced the initial

photon.

Positrons and electrons can be produced in the hadronic system, and can be identified by the neural network. Photons, having a similar signature to that of electrons and positrons, are also sometimes identified as such. These events are good photoproduction events since the scattered positron has gone down the RCAL beam pipe, and not been scattered into the calorimeter. The found "electron" is not the scattered one. Such events should be kept. In contrast, if a scattered positron is found in the calorimeter, it is a DIS event and must be rejected. The decision to keep the event is based on a cut on y using the electron method, such that the event is kept if $y_e > 0.7$. These "electrons" are soft, that is they are of low energy and less likely to be the scattered positron. Events with $y_e < 0.7$ are considered to be DIS events and are rejected.

5.2.6 BPC Sample

The BPC sample accesses events where the photon has a virtuality $0.1 < Q^2 < 0.55$ GeV^2. The same cut on y_e is applied as for the photoproduction sample to remove DIS events. The scattered positron must be well measured in the BPC.

Only information from the north module is used here. The exit window in front of the south module is substantially smaller than that for the north module. Hence, at the module faces, the available area for good measurement of positron energy and position is much greater in the case of the north module. Also, bremsstrahlung photons are more likely to enter the south module, because of its location on the outside of the HERA ring. For these reasons, the south module is not used to measure positrons in this analysis. It is used however, as a calibration tool. Using elastic QED Compton scattering events, and detecting a positron in one module, and a photon in the other, the BPC group can calibrate the modules to readout correctly the energies deposited in them.

From now on, references to measurements made with the BPC will refer only

to measurements using the north module. The criteria for the scattered positron to be well measured are

- Energy in the BPC must be greater than 12.5 GeV. This is related to the upper cut on the y range of 0.55 which translates to the scattered positron having an energy greater than 12.5 GeV. The cut also removes events where energy is deposited, but from non-positron particles, since such energies tend to be much lower than this threshold.

- The energy shower in the BPC is reconstructed to give information on the path of the positron track which entered it. The position extrapolated to the face of the BPC is required to be within the area shown in figure 5.2. Superimposed on this picture as points are the impact position of positrons satisfying the BPC energy cut. The shape of the distribution is due to the shape of the beam pipe exit window. The fiducial area is constructed to lie within this distribution as well as requiring that the positron shower is reasonably contained and the impact position can be reasonably reconstructed. This requirement also ensures that any positron coming from the interaction point has passed through less than 0.02 radiation lengths of material, leading to very little energy loss before its energy is measured in the BPC. This requirement also ensures a well contained electromagnetic shower from which no energy has leaked out of the sides of the BPC.

- The shower width must be less than 0.7 cm. This reduces the probability of accepting hadronic activity, since hadronic showers hitting the BPC generally have wider shower profiles.

- The BPC time (the time at which the energy deposit arrives) must be within 3 ns of the average BPC time of that run. This helps to ensure the positron came from a good ep interaction.

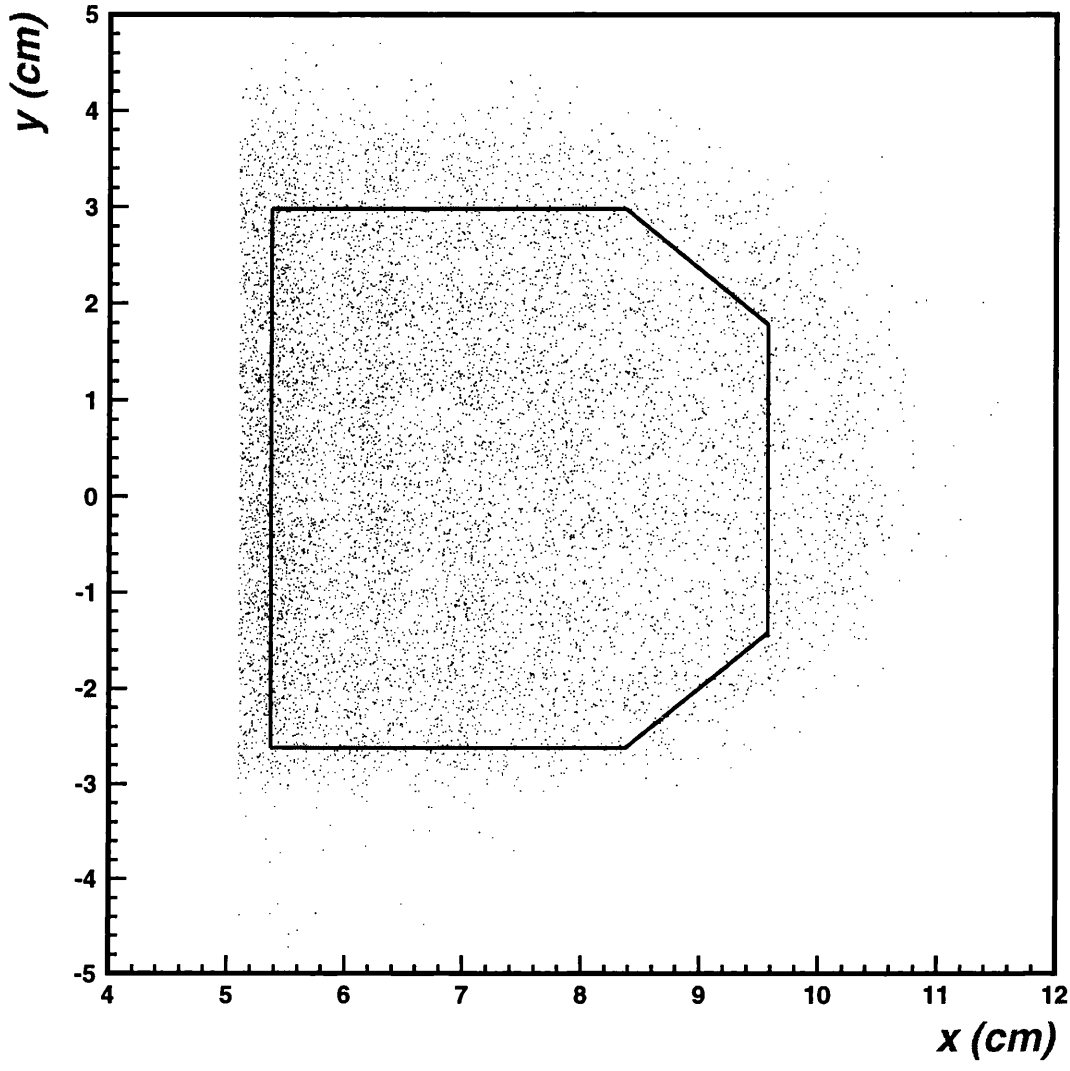

Figure 5.2: Diagram of the fiducial area cuts for the BPC.

As mentioned earlier the inelasticity, y, ranges from 0.2 to 0.55, the upper cut being made due to detector acceptance of this sample. The available phase space for measurement is shown in figure 5.3. Inside the box is the region of phase space for which the measurement is made. The other lines are the limits of measurement given the geometry of where the BPC and its fiducial area are placed in the ZEUS detector. The box is slightly larger than the area of phase space which is accessible. Superimposed are Monte Carlo events which fall inside

the region in Q^2 and y that we wish to measure, shown as dots.

Monte Carlo events are used to simulate the physics processes and detector performance. Given this Monte Carlo sample of simulated events, mismeasurement due to detector effects can be corrected for. This will be further discussed in chapter 7. For those regions of phase space outside the BPC acceptance, there is a small extrapolation to the full cross section which is dependent upon the Monte Carlo used to simulate the data. To determine if such an extrapolation is reasonable, it is noted that the numbers of events which fall into those regions outside the box form approximately 10% of the total sample, so if the extrapolation was considerably off, it would be an effect of the order of 10%. However, as shall be seen later, the Monte Carlo simulates the data well, so the extrapolation is indeed reasonable.

5.2.7 DIS Sample

The DIS sample accesses events where the photon has a virtuality $Q^2 > 1.5$ GeV^2. Here no such y_e cut is made since the DIS events must be accepted. The positron is now measured in the calorimeter. To have a well measured positron, the SINISTRA electron finding algorithm is applied, and positrons are accepted if their energy is greater than 10 GeV, and their position is outside a box cut around the RCAL beam pipe of $-14 < x_{pos} < 14$ cm, and $-9 < y_{pos} < 9$ cm. The higher the energy of the positron found, the better the position is reconstructed. This cut is also linked to the y cut at 0.55, since events with electrons with a lower energy than 10 GeV cannot (due to the kinematics) have a y less than 0.55. The box cut ensures that the positron is well contained inside the calorimeter, and that all its energy has been measured, and that none has leaked out of the edge of the calorimeter.

When y_{JB} is calculated, the calorimeter cells associated with the scattered positron are removed from the calculation, since the sum over cells should be

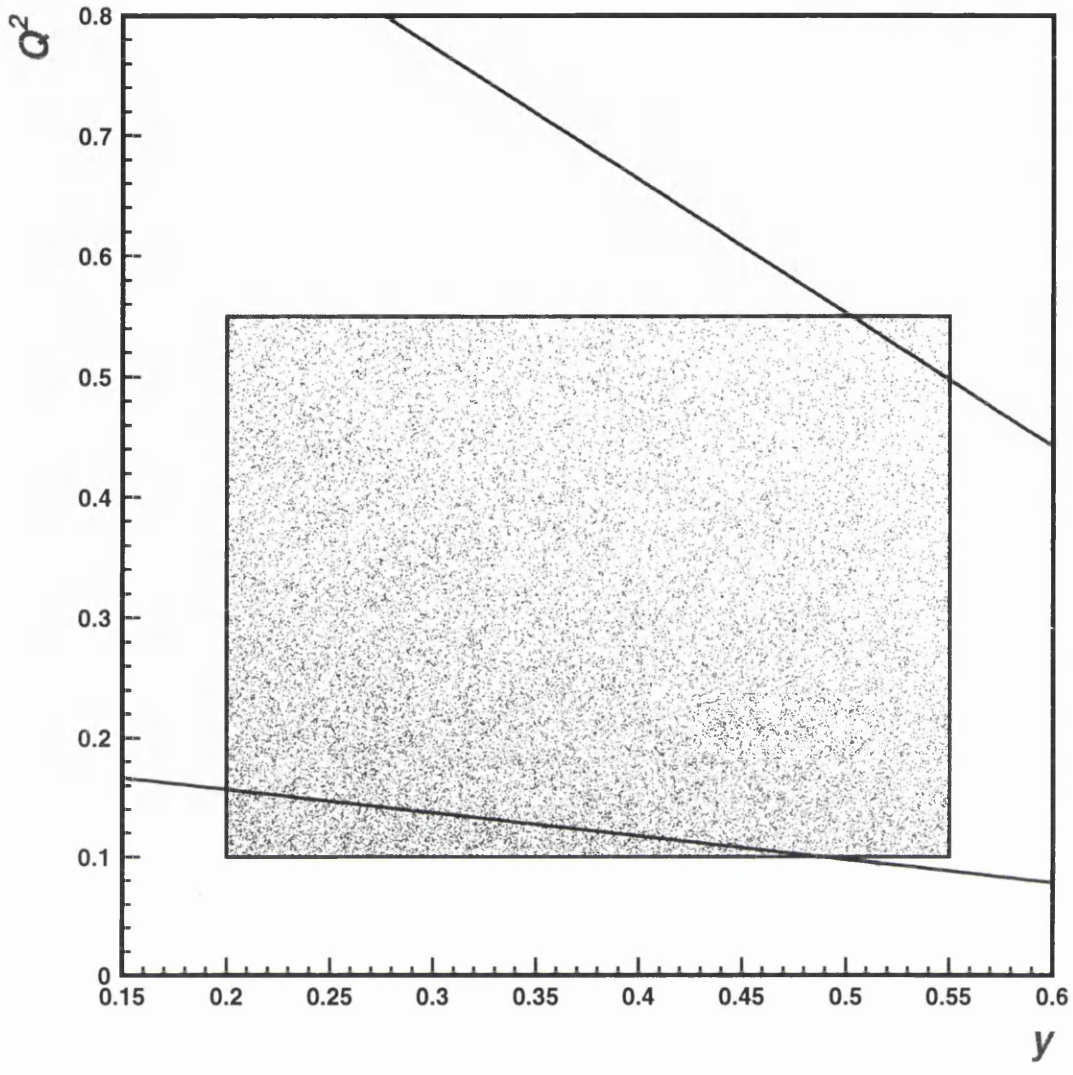

Figure 5.3: Diagram of the phase space available for the BPC in the Q^2 (measured in GeV^2) and y plane.

over those cells which contain activity from the hadronic system, and not the scattered positron. Similarly, when the jet finding algorithm is performed, the positron cells are removed from the procedure. At the online trigger stage, often a jet is found which is not a jet originating from a quark or gluon, but rather from the cells where the positron has scattered into, due to the large energies deposited there. The jets required are those of a hadronic nature, and so it is

possible to perform a more careful jet finding procedure offline, and obtain a sample of hadronic jets only.

Chapter 6

Event and Detector Simulation

Monte Carlo simulated events are generated primarily to correct the measured data distributions for detector mismeasurement effects. The Monte Carlo can be used to correct the data if it models the data well. It simulates the processes in which we are interested in stages. Using the principles of perturbative QCD, the leading order hard subprocesses are generated (in this analysis this means the two quarks or gluons which will ultimately form the dijet system). These then produce showers of partons. The partons are then passed through models of non-perturbative phenomena to simulate the soft physics processes of fragmentation and hadronisation. By this stage, the event now consists of a set of stable hadrons and leptons. This stage will be referred to as the "hadron level".

Once generated, the hadrons are put through a GEANT [42] based simulation of the ZEUS detector and a simulation of the trigger decision procedure. Finally, the events are passed through the offline reconstruction package, such that the events are now directly comparable with the data. This stage will be referred to as the "detector level".

Two Monte Carlo samples are used in this analysis to correct the data for detector effects. These are HERWIG 5.9 [43] and PYTHIA 6.1 (which is a recently updated version of PYTHIA 5.7 [44]). For this analysis, HERWIG 5.9 is used as the principal Monte Carlo package to correct the data for detector

effects. The statistics on the HERWIG sample amounts to at least twice as many events as in the data for all samples. The PYTHIA 6.1 is a relatively new version of the PYTHIA generator. Previous versions of this generator did not include a Q^2 spectrum for resolved and direct processes at low Q^2, rather the scattered positron was assumed to travel down the beam pipe as in the photoproduction limit. This would have been useless for simulation of events whose positrons could be measured in the BPC. Consequently, the number of PYTHIA 6.1 events generated and put through the detector simulation since this new generator became available, has amounted to a sample approximately equal in number of events to that of the data in all samples, and is therefore used to determine the systematic effect of correcting the data with a Monte Carlo which implements a different hadronisation scheme.

6.1 HERWIG 5.9

HERWIG uses exact matrix elements to calculate the flux of photons emitted from the incoming positron. The hard subprocess parton scattering is simulated using leading order QCD diagrams. The hadronisation process is performed using a cluster algorithm. There is a cut on the minimum transverse momentum p_T^{min} which the hard subprocess produces. This is set to 2.5 GeV, which is the value that produces the best description of the data.

Events can also have secondary, or multi-parton interactions (MIs). A second sample of events with MIs are simulated for the photoproduction sample only, since this is where such interactions have the largest effect. As in the case of the PYTHIA sample, this sample with MIs is used to estimate the systematic effect of correcting the data with a Monte Carlo which contains this extra process. To generate a HERWIG sample with MIs, HERWIG is interfaced to the JIMMY library [45], specifically written to generate MIs within HERWIG. The parton density functions used for the proton and resolved photon are MRSA [46] and

GRV LO [47] respectively.

6.2 PYTHIA 6.1

PYTHIA uses the Weizsäcker-Williams Approximation [12] to calculate the flux of photons emitted from the incoming positron. The sample of PYTHIA generated contains MIs to better approximate the data. The hard subprocess parton scatter is calculated using leading order QCD diagrams and the hadronisation is modelled using the LUND string fragmentation model as implemented in JETSET [44]. The parton density functions used for the proton and resolved photon are MRSA [46] and SaS1D [26] respectively. PYTHIA 6.1 includes options to have the resolved cross section suppressed relative to the direct as Q^2 increases. This was not implemented since the SaS1D PDF already includes such suppression.

6.3 Description of data by Monte Carlo events

The Monte Carlo simulated events used to correct the data for detector effects should describe the data distributions which are cut on to produce the event samples to be studied. If the Monte Carlo fails to describe the data significantly, the correction for detector effects will be miscalculated. The following distributions are comparisons of the measured data with Monte Carlo events which have undergone the ZEUS detector simulation. Demonstration of good agreement is necessary to be confident that the correction procedure is valid.

All the Monte Carlo samples generated are constrained by certain parameters to be defined by the user. These include the photon PDF, proton PDF, Q^2 and y ranges of events. Another parameter which should be mentioned is the minimum transverse momentum cut, p_T^{min}, which is set at 2.5 GeV for best fit to the data. This parameter defines whether or not the event generated will be allowed into the sample based on the sum of the transverse momenta of the two partons (which

will proceed later to form jets) in the rest frame of the dijet system. It also removes any singularity that occurs in the calculation of the cross section when the sum of the transverse momenta of the two partons tends to zero.

In the following plots, the relative contributions of the resolved and direct processes have been reweighted to fit the measured $d\sigma/dx_\gamma^{obs}$ differential cross sections. This is done because the cross section evaluation of the two processes typically does not match data measurements. The cross sections which the Monte Carlo calculates should not determine the correction factors to correct the data, rather it is the mapping between measured distributions and the generated ones which should matter. Hence, such a reweighting procedure serves to correct the cross sections from the Monte Carlo to be what they should be. It then follows that, after reweighting, the x_γ^{obs} distribution should have very good agreement between data and Monte Carlo. The reweighting procedure is done for each bin in Q^2. The reweighting factors for the resolved and direct Monte Carlo samples as a function of Q^2 for HERWIG (with and without MIs) and PYTHIA are shown in tables 6.1, 6.2 and 6.3.

The reweighting factors in table 6.1 decrease for both resolved and direct processes as Q^2 increases. The resolved factors decrease more rapidly than the direct due to the fact that the PDF used in this HERWIG sample for the resolved photon is that of a real photon, and does not include suppression of the resolved cross section with increasing photon virtuality. The PYTHIA sample (table 6.3) has a PDF which does include such a suppression, and so this sample matches the data better, indicated by the fact that the reweighting factors do not vary as much as those of the HERWIG sample over most of the range in Q^2. Indeed the direct process cross sections match the data very well, and the resolved process appears to be only slightly over-suppressed as can be deduced from the slow rise in the resolved reweighting factors with increasing Q^2.

The Monte Carlo having been reweighted it should now match the data distributions better than without reweighting. This serves to improve the

HERWIG 5.9 (no MIs and GRV LO photon PDF)		
Q^2 (GeV^2)	Reweight Factor (Resolved)	Reweight Factor (Direct)
≈ 0	1.93	1.72
0.1 - 0.55	1.26	1.64
1.5 - 4.5	0.43	1.29
4.5 - 10.5	0.26	1.22
10.5 - 49.0	0.18	1.19
49.0 - 5000.0	0.17	0.86

Table 6.1: The reweighting factors applied to the HERWIG 5.9 (no MIs) sample in order to match the data.

HERWIG 5.9 (with MIs and GRV LO photon PDF)		
Q^2 (GeV^2)	Reweight Factor (Resolved)	Reweight Factor (Direct)
≈ 0	1.54	1.73

Table 6.2: The reweighting factors applied to the HERWIG 5.9 (with MIs) sample in order to match the data. This sample only has photoproduction events simulated.

correction of the data for any mismeasurements due to the imperfections in the detector, such as particles losing energy in dead material before being measured in the calorimeter. As long as the relative resolved and direct cross sections are reweighted to match the data distributions in shape, the correction procedure should be fine. It does not depend upon the absolute cross sections as produced by the various Monte Carlo generators.

The jet distributions for the photoproduction sample are shown in figure 6.1, and similarly for the BPC and DIS samples in figures 6.2 and 6.3 respectively. These jet distributions all have reasonable agreement between data and Monte Carlo for all samples. Some do better than others, depending on the Q^2 range examined, but there is no clear Monte Carlo which excels above the others in its

PYTHIA 6.1 (with MIs and SaS1D photon PDF)		
Q^2 (GeV^2)	Reweight Factor (Resolved)	Reweight Factor (Direct)
≈ 0	1.14	1.06
0.1 - 0.55	1.06	1.14
1.5 - 4.5	1.45	1.13
4.5 - 10.5	1.36	1.10
10.5 - 49.0	1.86	0.98
49.0 - 5000.0	9.09	0.19

Table 6.3: The reweighting factors applied to the PYTHIA 6.1 (with MIs) sample in order to match the data.

description of the data across the whole range in Q^2.

These jet distributions are averaged over all events which are selected to be in each sample. Since a jet is a complex object composed of many final state hadrons, it is instructive to look more closely at the jets themselves.

Models including multi-parton interactions tend to describe the data better for low transverse energy jets and/or very forward jets (high pseudorapidity). The effect of having multi-parton interactions (MIs) in the event sample is to increase the number of measured events in the low x_γ^{obs} region (the "resolved-enriched" $x_\gamma^{obs} < 0.75$ region). There are a number of effects which enter the x_γ^{obs} distribution, not just the effects of MIs. It is therefore instructive to examine the event topology in order to see if there is energy flow consistent with that of an event with a secondary interaction. This is checked by means of examining jet profiles.

Figure 6.4 shows such a jet profile plot. All following jet profile plots are for the photoproduction sample only, since this is where the effect of MIs is the largest. The transverse energy of a jet as a function of $\Delta\eta$ is plotted, where $\Delta\eta$ is the difference in pseudorapidity between the centre of the jet and the transverse energy which is measured there. There is also a cut made such that the transverse

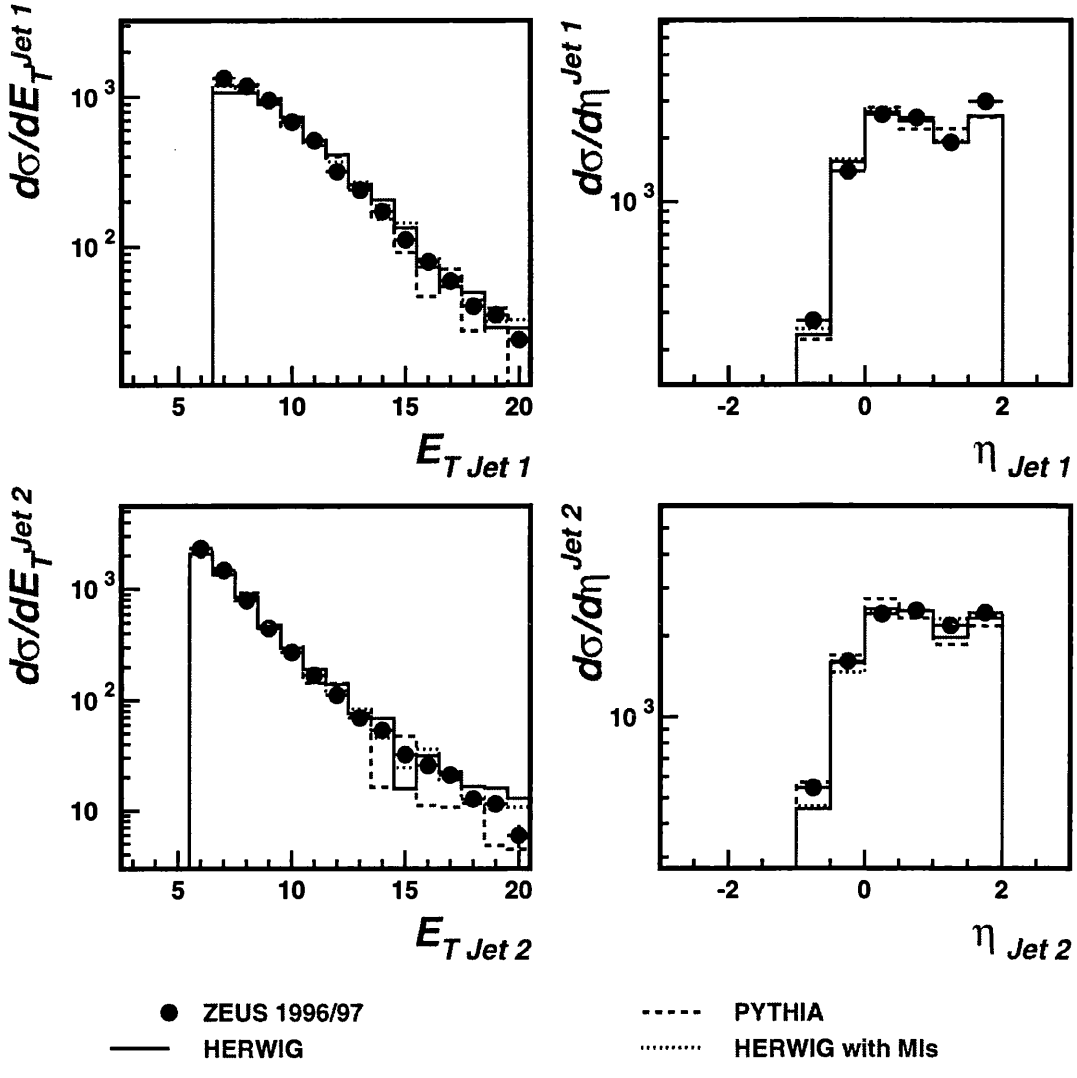

Figure 6.1: Jet transverse energy and pseudorapidity distributions for the photoproduction sample. The dots are the measured data and the line histograms are the Monte Carlo events after detector simulation. The cross sections are measured in pb and the energies in GeV.

energy measured is only that within $\pm$ 1 radian in azimuthal angle from the jet centre. This serves to isolate the jet from its partner, the second jet of the dijet system, which is generally opposite the first jet in azimuthal angle.

This profile plot shows that most of the transverse energy of these jets is found to lie within ± 0.7 units of pseudorapidity around the jet axis. There

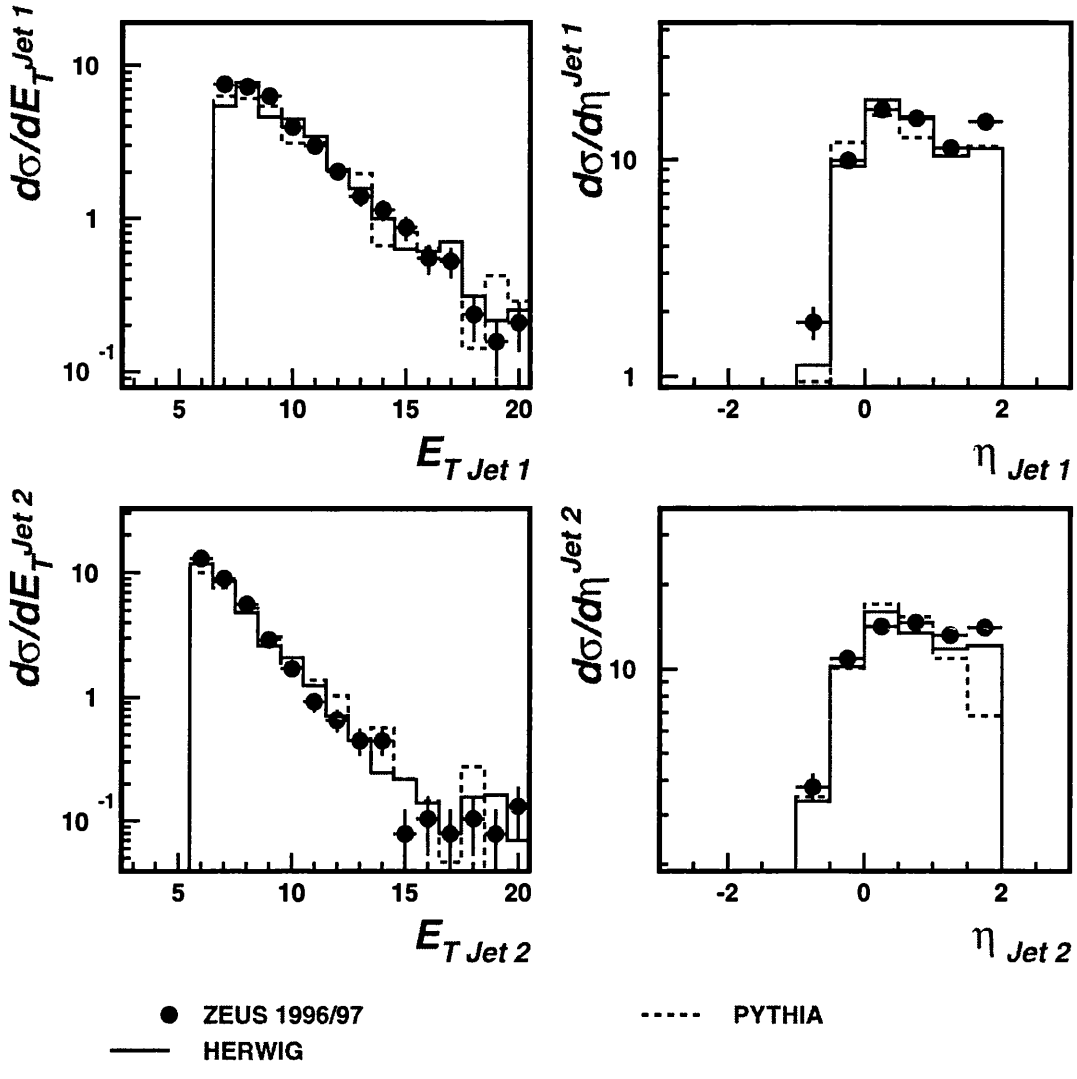

Figure 6.2: Jet transverse energy and pseudorapidity distributions for the BPC sample. The dots are the measured data and the line histograms are the Monte Carlo events after detector simulation. The cross sections are measured in pb and the energies in GeV.

is also a "pedestal" on which the jet is superimposed, this pedestal becoming larger in the more forward (higher pseudorapidity or higher $\Delta\eta$) region. This pedestal is due to other energy in the event which has originated from softer interactions than the hard jet, or events with more than two jets, where the cut in azimuthal angle no longer isolates the jet as well as it does for the dijet case.

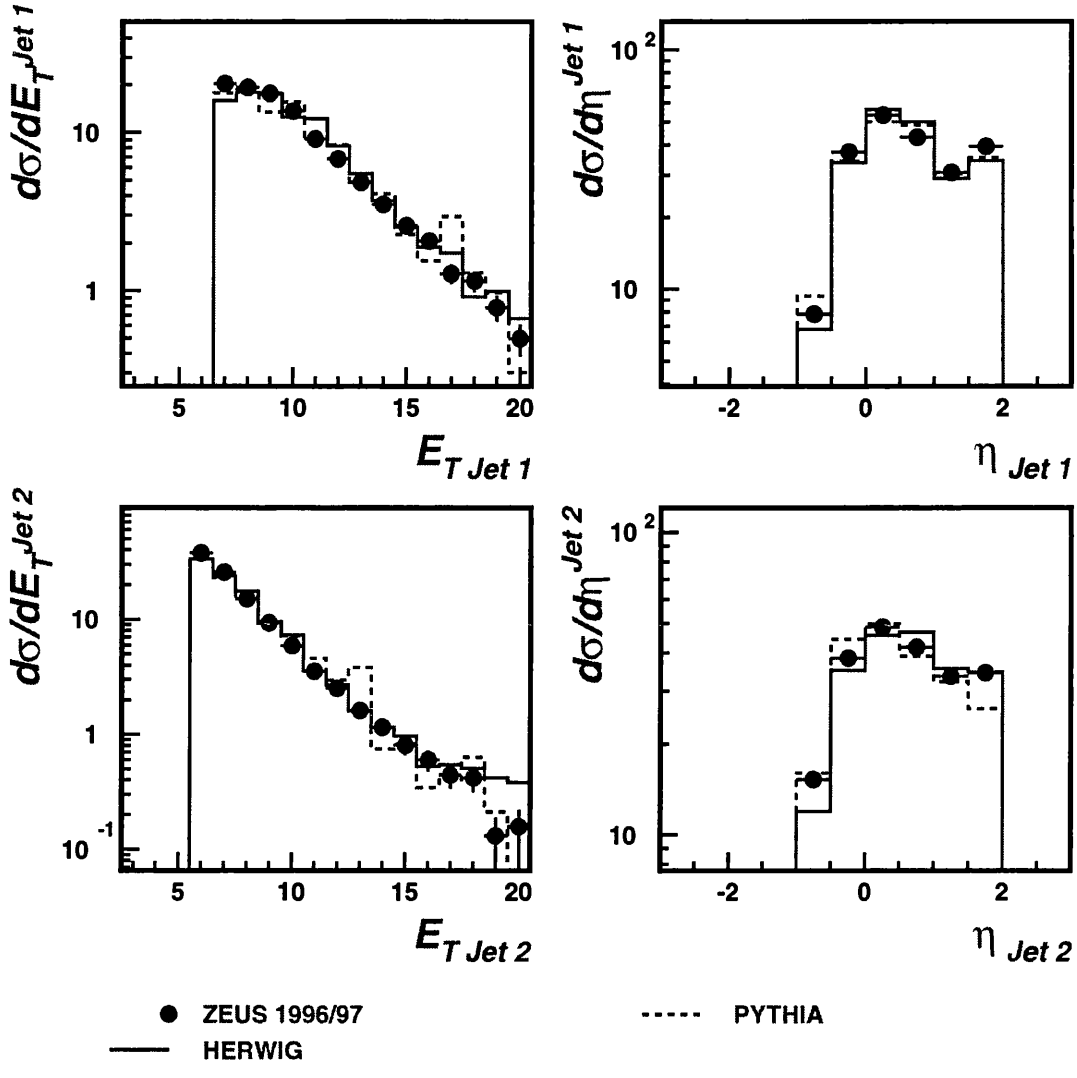

Figure 6.3: Jet transverse energy and pseudorapidity distributions for the DIS sample. The dots are the measured data and the line histograms are the Monte Carlo events after detector simulation. The cross sections are measured in pb and the energies in GeV.

The Monte Carlo overestimates the transverse energy at the centre of the jet, and underestimates the pedestal. If MIs are present in the sample, the pedestal is higher in the forward region, which is typical of such secondary interactions, where the transverse energy is lower, and deposited in the forward region. The MI model assumes that such interactions occur for the resolved process only. By

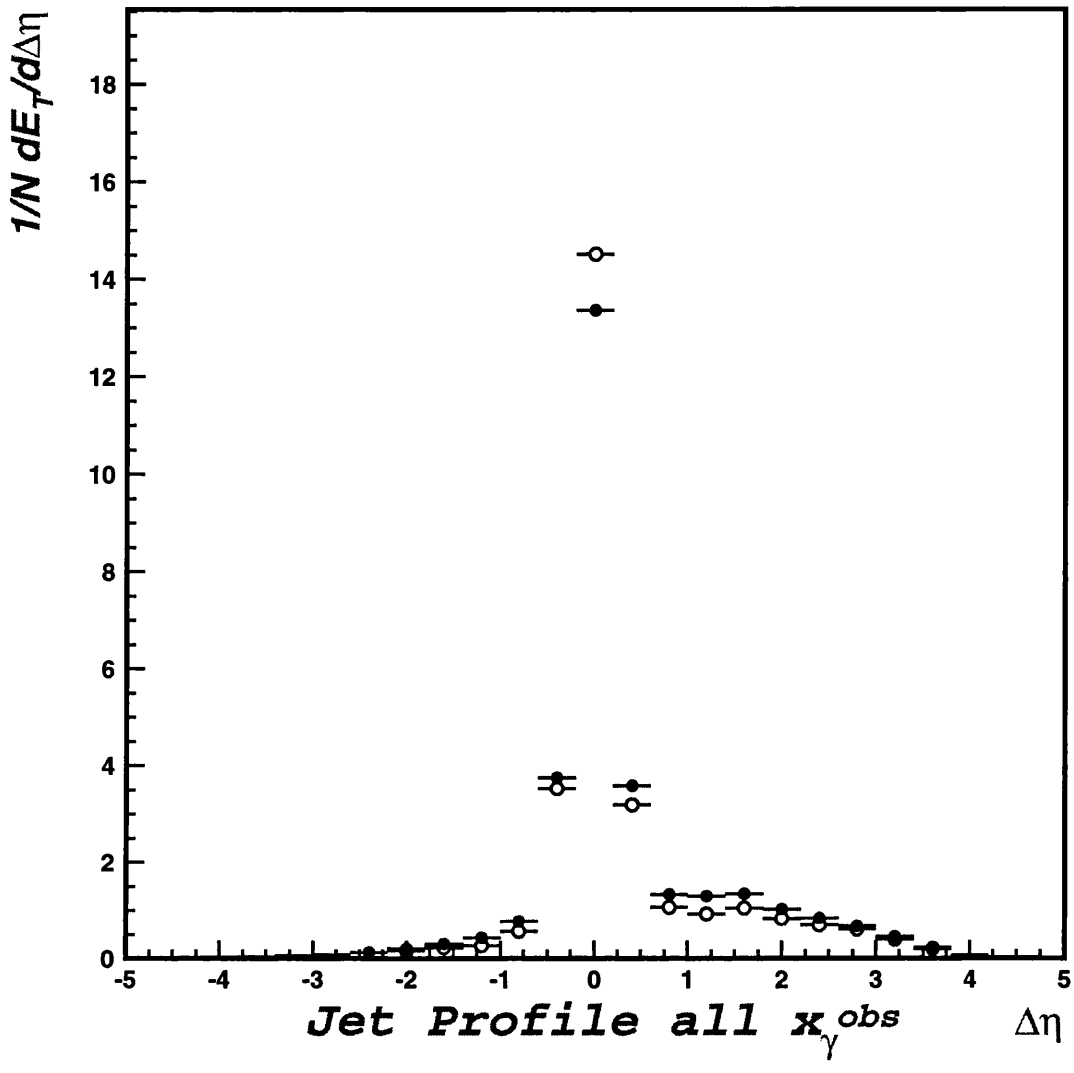

Figure 6.4: Jet profile plot examining the transverse energy flow (in GeV) around the jet centre for the photoproduction sample. The filled circles are the measured data and the open circles are the HERWIG Monte Carlo events after detector simulation.

examining jet profiles for $x_\gamma^{obs} < 0.75$ (resolved-enriched) and $x_\gamma^{obs} > 0.75$ (direct-enriched), it is possible to see whether discrepancies are more pronounced for the resolved-enriched region, as expected if MIs are present in the sample.

Figure 6.5 is the profile plot for jets from a "direct-enriched" event. Whilst the transverse energy at the centre of the jet is still overestimated by the Monte Carlo, the agreement around the pedestal is much better. Conversely, looking at the

resolved-enriched sample, the jet profile (figure 6.6) shows that the discrepancy in the forward region of the pedestal comes almost totally from the resolved-enriched sample, consistent with the hypothesis that there are some MIs in the sample.

Figure 6.7 shows the agreement of the data with HERWIG 5.9 including MI simulation. This agreement is much better than that of figure 6.4, and again supports the hypothesis that MIs, or events which have similar topology to MIs, are to some extent present here. Also shown in figure 6.8 is the corresponding PYTHIA 6.1 profile, recalling that this sample already includes MIs. This sample of Monte Carlo events shows excellent agreement with the data for this sample of photoproduction events. The topology of the final state depends not only on whether MIs are simulated, but also on the hadronisation model of the Monte Carlo in use. Correcting the data using HERWIG without MIs and then using PYTHIA with MIs maximises the effect of the difference between the two Monte Carlo samples to obtain a systematic error on the corrected result which reflects the limits of fluctuation of that corrected result due to model dependence.

According to the model of MIs, their effect reduces as the photon virtuality increases, since the resolved photon contribution to dijet events reduces, and so therefore does the MI effect which occurs only for resolved photon events. Since all Monte Carlo events are reweighted to fit the x_γ^{obs} distribution of the data, this reduces the dependency of the correction procedure on the particular Monte Carlo sample used to correct the data. The choice of Monte Carlo to use for correcting the data for detector effects then becomes a matter of statistics. Since the HERWIG 5.9 sample without MIs is by far the largest sample, this is used for the correction of the data. The PYTHIA 6.1 sample best approximates the data as far as the jet profiles are concerned, and the systematic error arising from the difference between correcting with the PYTHIA 6.1 sample is examined in chapter 7.

The event samples are restricted to be in the y range $0.2 < y < 0.55$. This

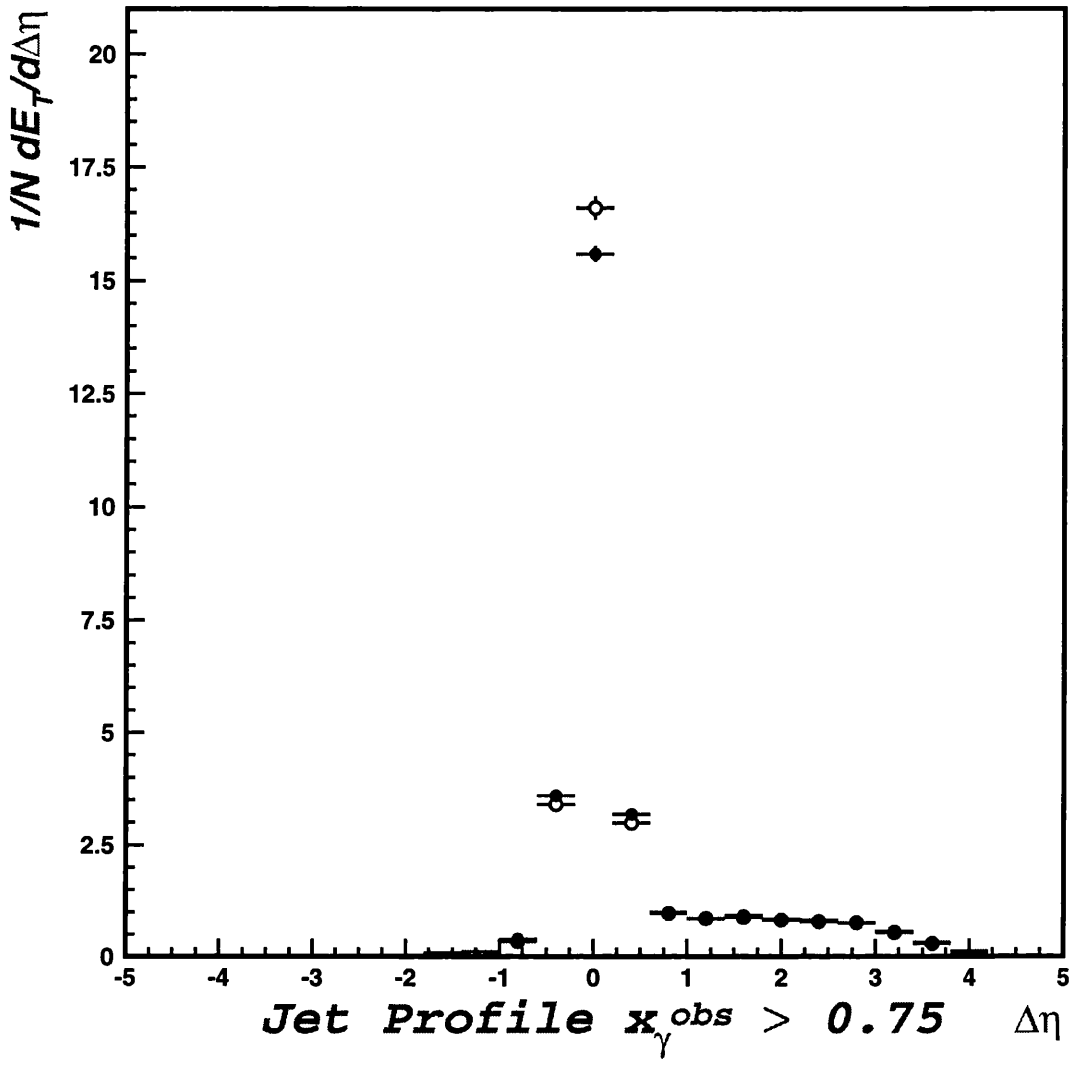

Figure 6.5: Jet profile plot examining the transverse energy flow (in GeV) around the jet centre for the photoproduction sample for events with $x_\gamma^{obs} > 0.75$. The filled circles are the measured data and the open circles are the HERWIG Monte Carlo events after detector simulation.

corresponds to a y_{JB} range of $0.15 < y_{JB} < 0.45$. The comparison of data with Monte Carlo in terms of y_{JB} is shown in figure 6.9 for all three samples (photoproduction, BPC and DIS). The agreement is satisfactory for all three samples. In terms of Q^2, (see figure 6.10) the agreement between data and Monte Carlo is excellent, which is not surprising as the reweighting procedure is Q^2

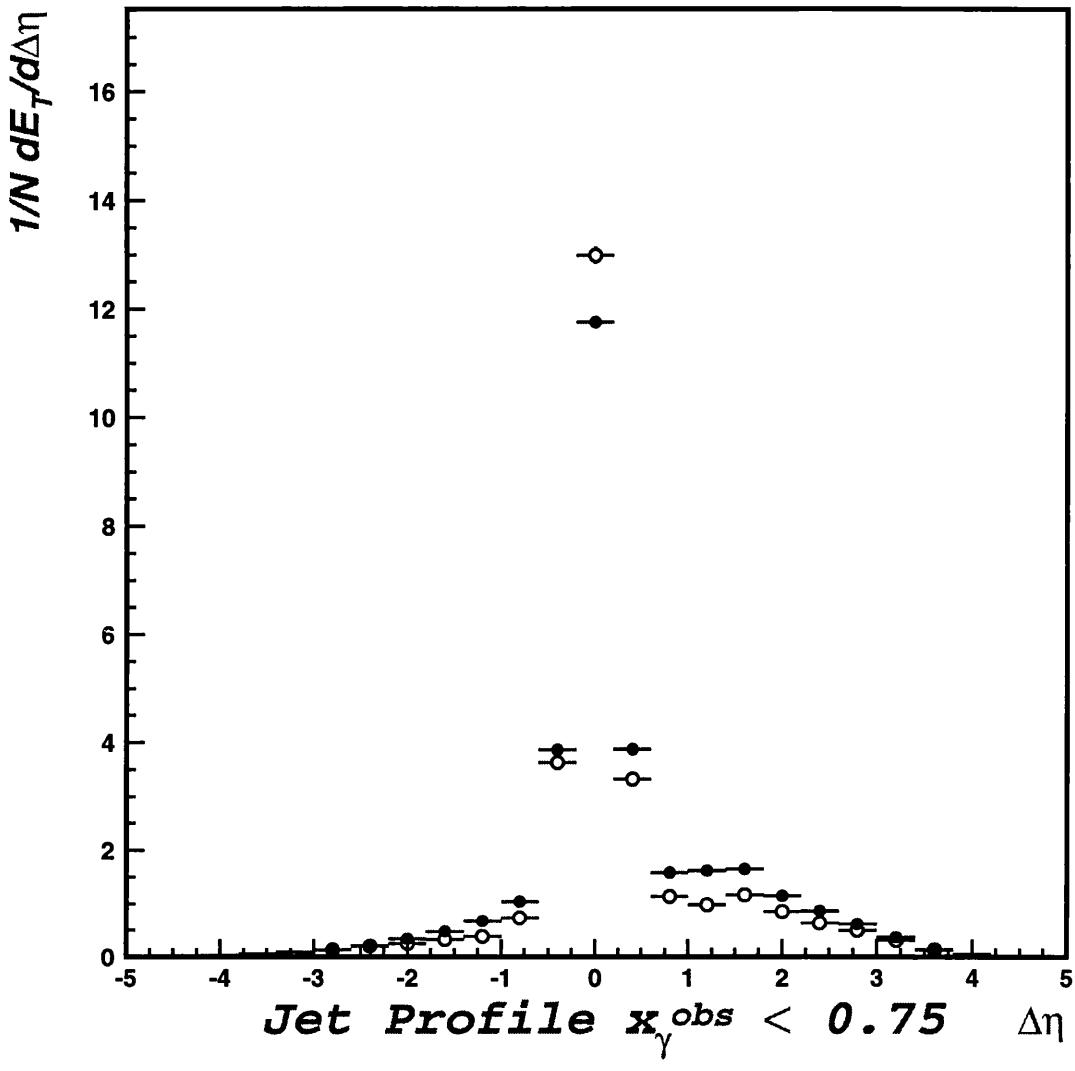

Figure 6.6: Jet profile plot examining the transverse energy flow (in GeV) around the jet centre for the photoproduction sample for events with $x_\gamma^{obs} < 0.75$. The filled circles are the measured data and the open circles are the HERWIG Monte Carlo events after detector simulation.

dependent and the reweight factor is different for each bin in Q^2. The form of the Q^2 distribution does not follow a $1/Q^4$ distribution as might be expected from theory. This is because the data has not been corrected for detector effects yet. In particular the third bin ($1.5 < Q^2 < 4.5$) has noticeably fewer events than the next bin up. This is due to detector acceptance, and the box cut applied

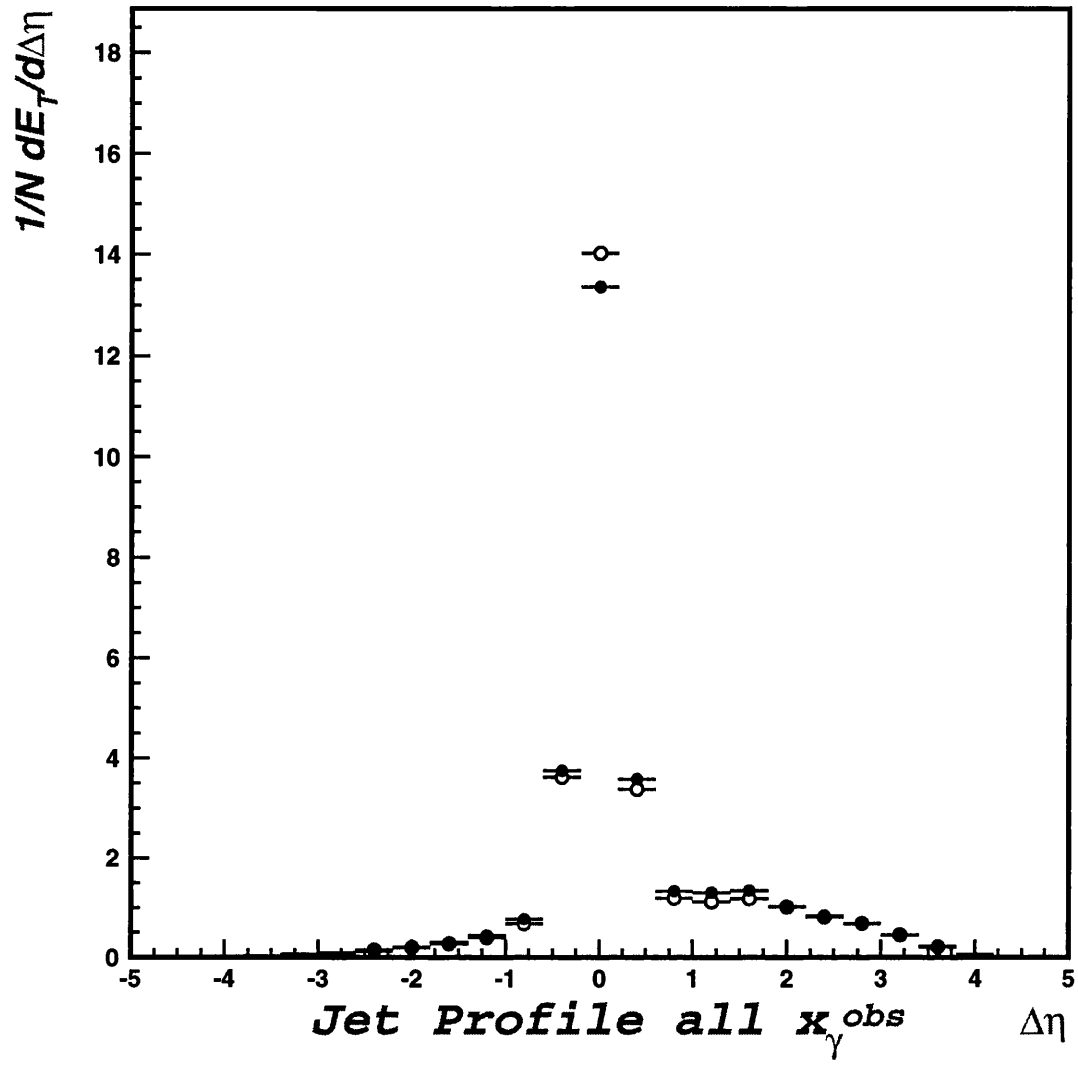

Figure 6.7: Jet profile plot examining the transverse energy flow (in GeV) around the jet centre for the photoproduction sample. The filled circles are the measured data and the open circles are the HERWIG Monte Carlo events, including simulation of multi-parton interactions, after detector simulation.

around the RCAL and SRTD to be sure of a well measured positron. The box cut removes a large number of events which would otherwise have been measured in this bin. The choice of binning in Q^2 is chosen to examine more closely the range where the resolved-enriched sample varies the most, as will be seen later in chapter 8.

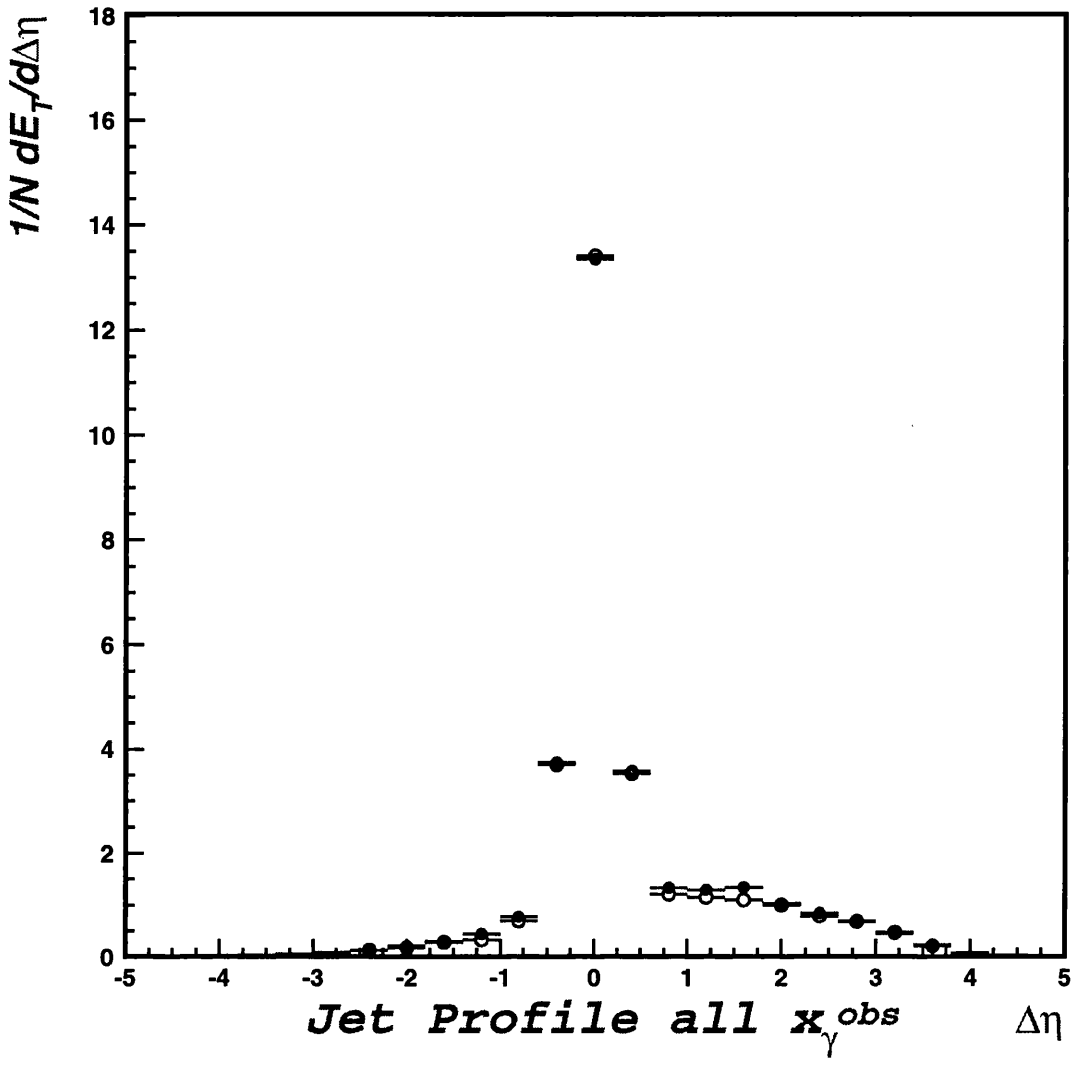

Figure 6.8: Jet profile plot examining the transverse energy flow (in GeV) around the jet centre for the photoproduction sample. The filled circles are the measured data and the open circles are the PYTHIA Monte Carlo events after detector simulation.

The x_γ^{obs} distributions, as already mentioned, have had the Monte Carlo resolved and direct photon samples reweighted to fit the measured data distributions for each of the three samples, and so the agreement between data and Monte Carlo is therefore very good as can be seen in figure 6.11.

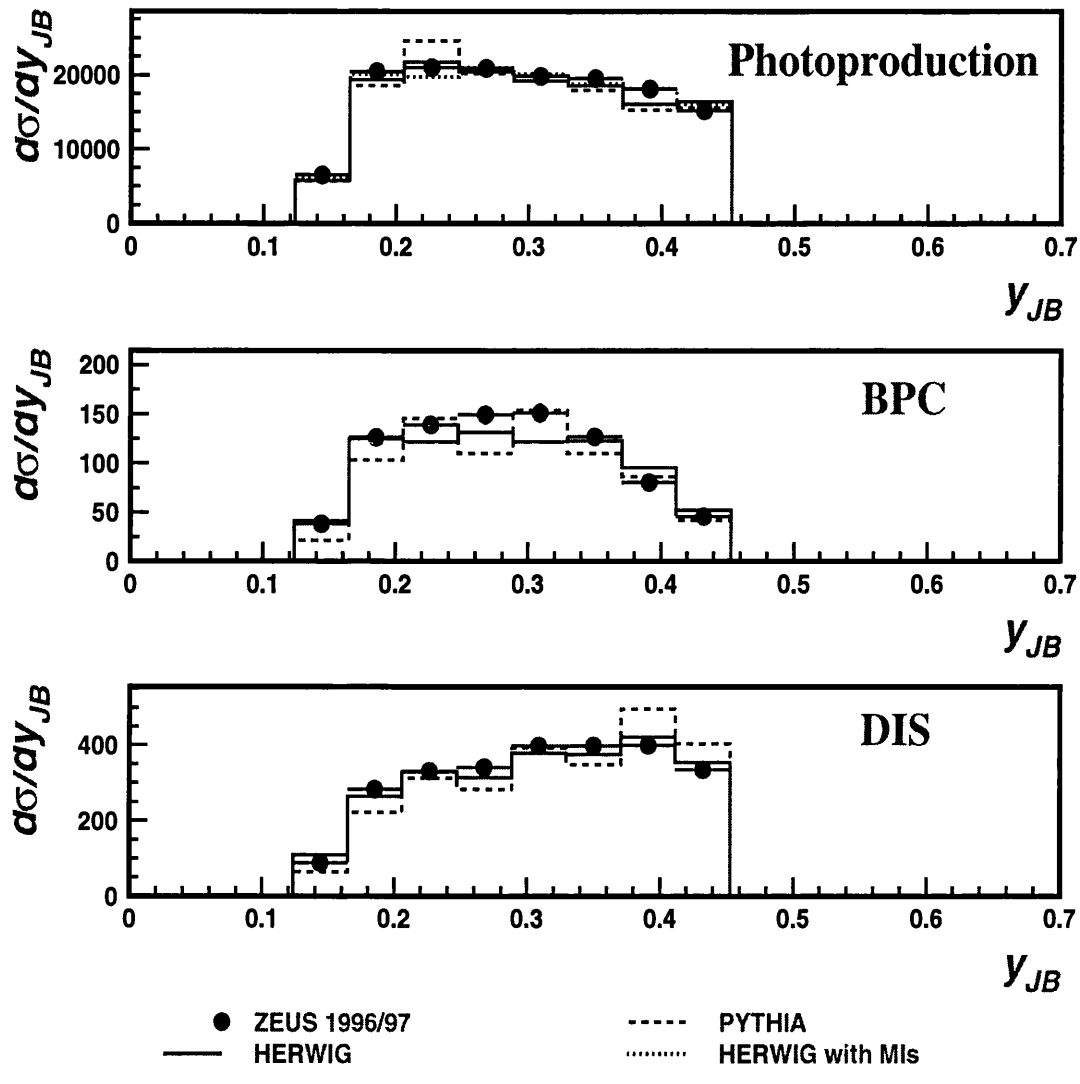

Figure 6.9: y_{JB} distributions for the photoproduction, BPC and DIS samples. The dots are the measured data and the line histograms are the Monte Carlo events after detector simulation. The cross sections are measured in pb.

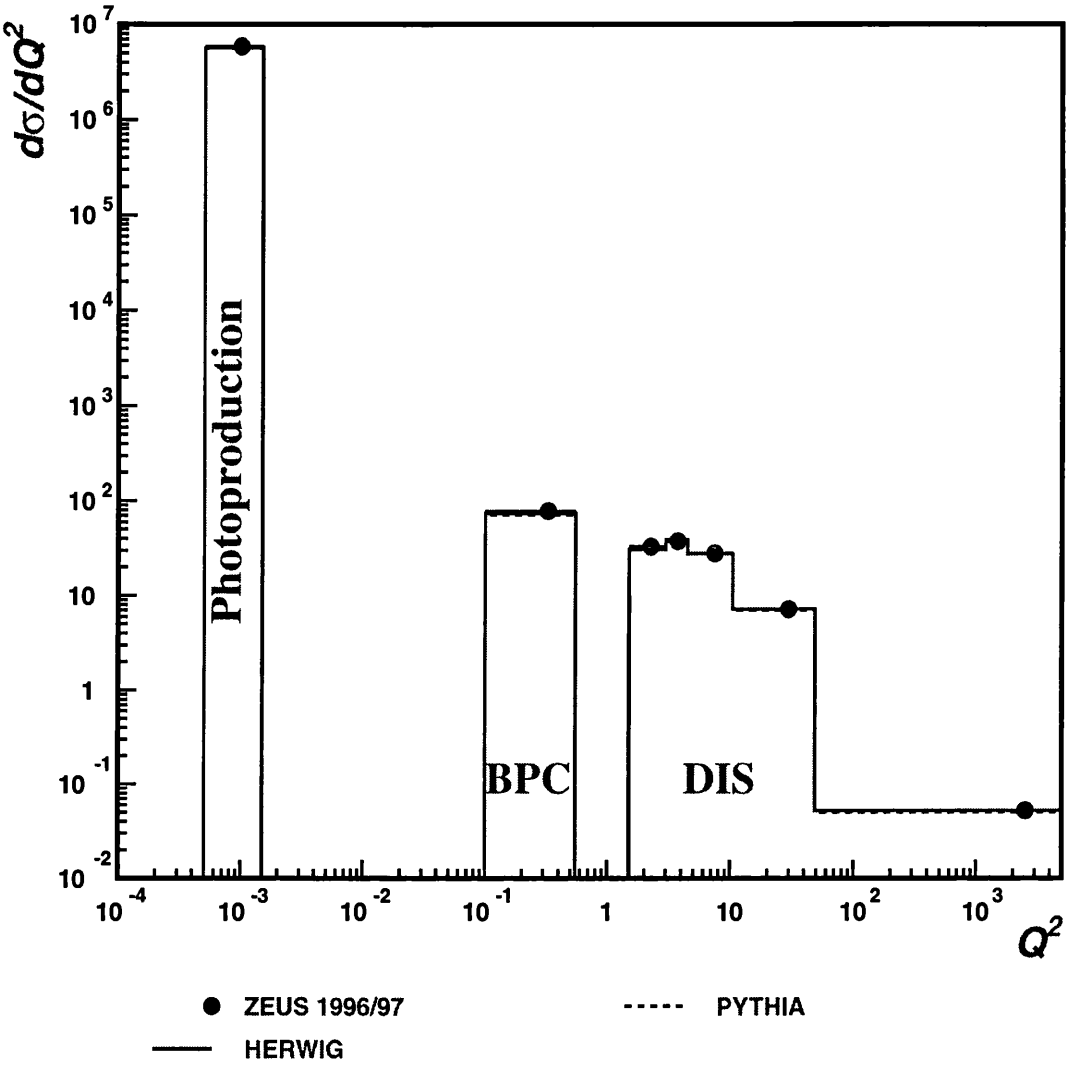

Figure 6.10: The Q^2 distribution across the whole range accessible. The dots are the measured data and the line histograms are the Monte Carlo events after detector simulation. The cross sections are measured in pb.

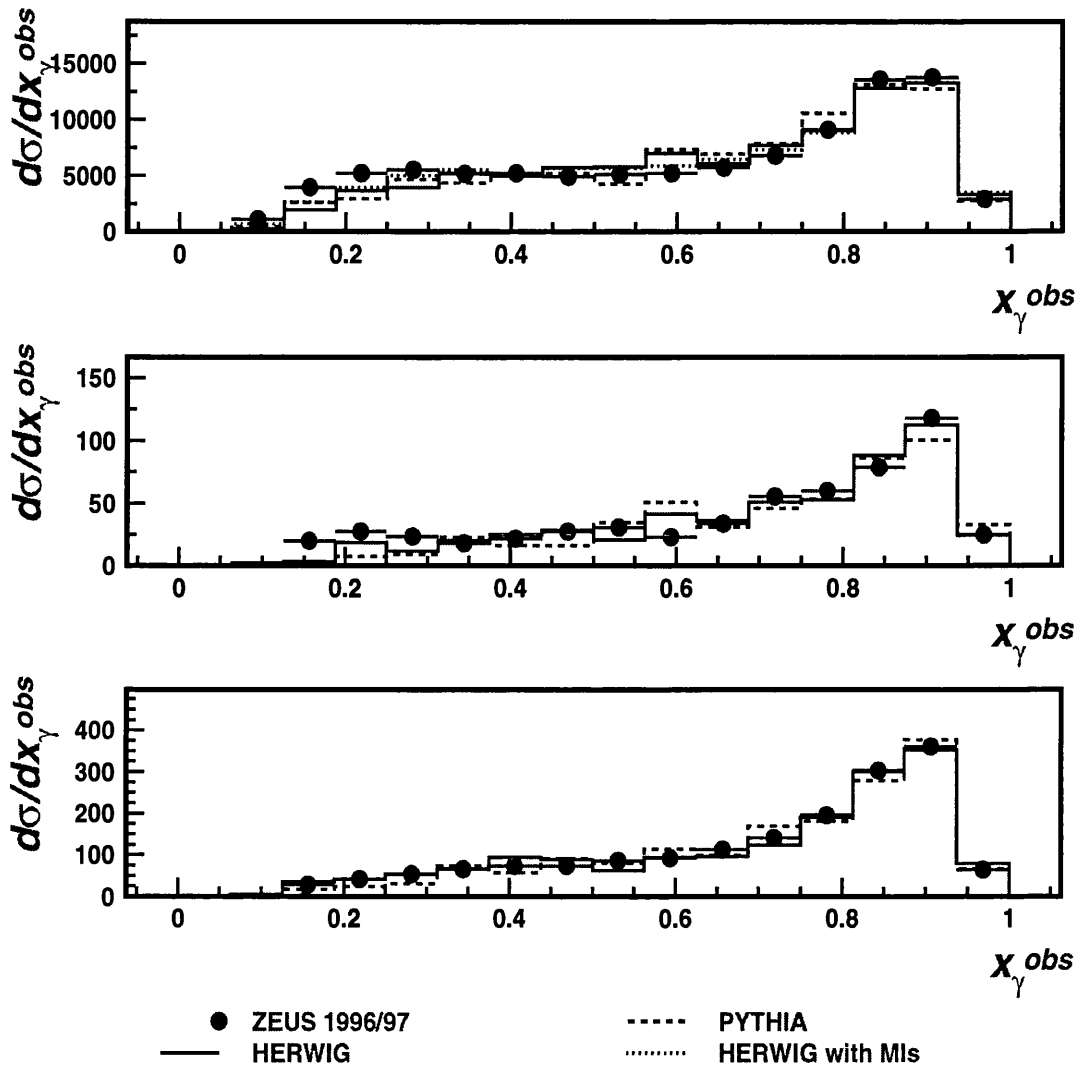

Figure 6.11: x_γ^{obs} distributions for the photoproduction, BPC and DIS samples. The dots are the measured data and the line histograms are the Monte Carlo events after detector simulation. The cross sections are measured in pb.

Chapter 7

Resolutions and Data Correction

The data distributions as measured by the ZEUS detector are not perfectly measured. There is always some mismeasurement which leads to variables having a resolution and a bias. The better the resolution, and the closer the bias is to zero, the more accurate is the measurement. The correction of the data for detector mismeasurement effects therefore depends on the resolution. The error assigned to the corrected data becomes smaller with better resolution on the measurement. Hence it is necessary to examine the resolution of the variables used for event sample selection and for the variables whose distributions are plotted. The Monte Carlo sample used for determination of resolution is HERWIG 5.9 without MIs simulated. This sample has a reasonable description of the data after the relative resolved and direct contributions have been reweighted to fit the data, and good statistics with respect to the other samples considered in this analysis.

7.1 Resolutions

The resolution of a variable is determined from Monte Carlo, since the hadron level variable (that variable which has not undergone the detector simulation and is therefore not mismeasured) can be compared directly with the detector

level variable (that variable which has undergone the detector simulation). The following resolution plots for each dimensionful variable are distributions of

$$\frac{(hadron\ level) - (detector\ level)}{(hadron\ level)}$$

for that variable, whilst dimensionless variables are plotted as distributions of

$$(hadron\ level) - (detector\ level)$$

in order to have all resolution plots in a standard dimensionless format.

The selection of jets is done by cutting on the transverse energy and pseudorapidity of the jet. Resolution plots of these quantities are obtained by comparing jets at both detector and hadron level. Due to the nature of the jet finding algorithm, there is not always a one to one correspondence between detector and hadron level jets. To study the effect of mismeasurement of a jet, it is necessary to select events with detector level jets which can be associated with a corresponding hadron level jet. Jets must therefore be 'matched' between detector and hadron level. This is done by selecting a sample of jets which belong to events that are in the sample required for the analysis, and have a hadron level jet within one unit radius of $\eta - \phi$ space. If two such jets exist (detector and hadron level), those jets are said to be matched, and are used for the jet resolution plots.

Figure 7.1 shows the resolution on the transverse energy of the jets. The mean of the distribution is not centred around zero. This is because the jets lose some energy in the dead material before being measured in the calorimeter.

The distribution is centred around a value of 0.1488. Taking the average of the hadron level jet E_T to be 7 GeV, this shift of the mean from zero implies that a 7 GeV jet has lost approximately 15% of 7 GeV energy. This is then 1 GeV difference in transverse energy between detector and hadron level, which is why the detector level selection cuts on the jet E_T are 6.5 and 5.5 GeV, which corresponds to hadron level jets of 7.5 and 6.5 GeV.

The resolution on the pseudorapidity is shown in figure 7.2. The distribution

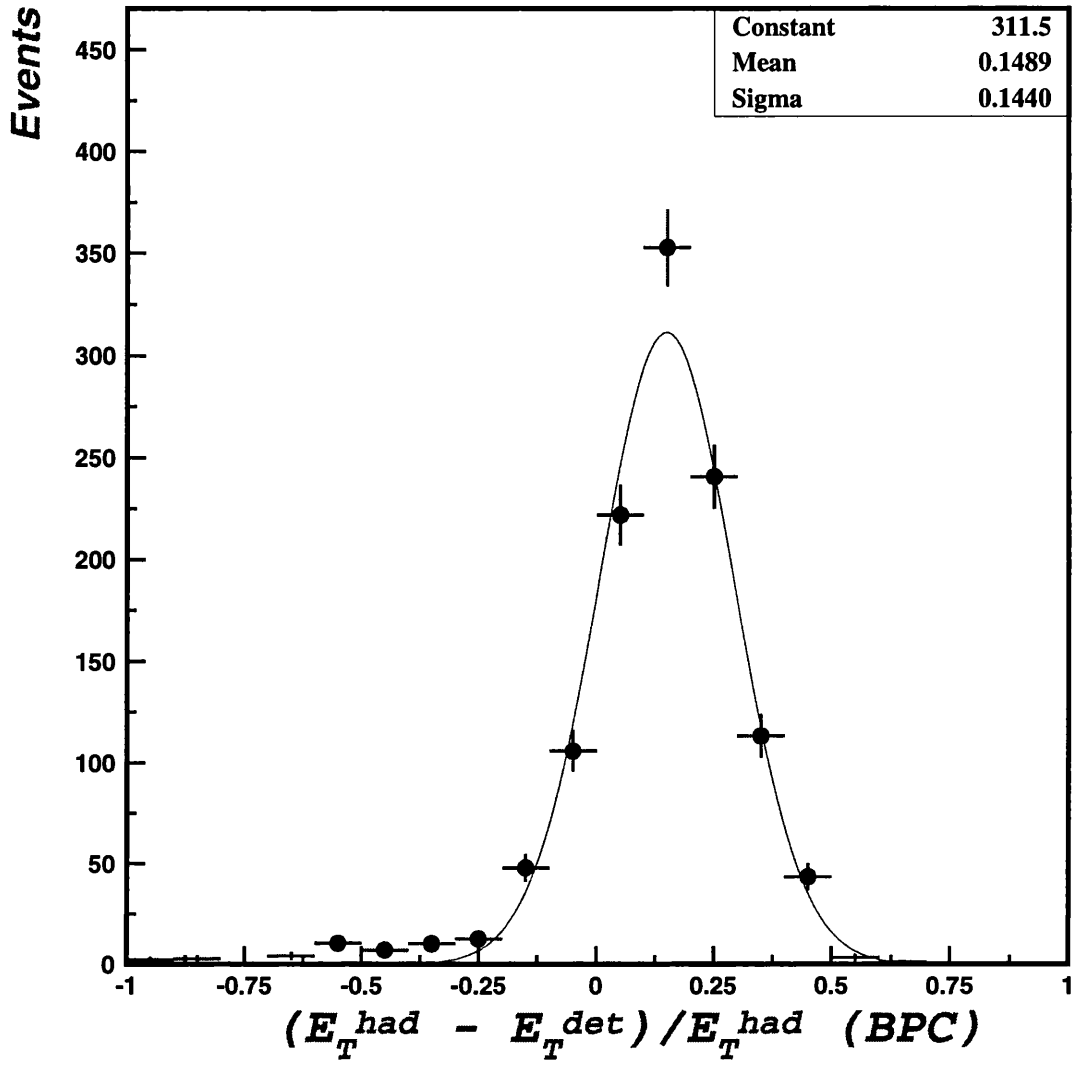

Figure 7.1: Jet transverse energy resolution.

is centred at zero, which means the detector and hadron level selection cuts are equivalent.

The resolution on y_{JB} depends largely on the resolution of the calorimeter. It is therefore approximately independent of the Q^2 of the event, and is similar then for all three samples - photoproduction, BPC and DIS. The y_{JB} resolution plot is shown in figure 7.3. The resolution on y_{JB} is better at lower values of y_{JB} than higher values. The mean shift increases from 0.04 at a hadron level y_{JB} of

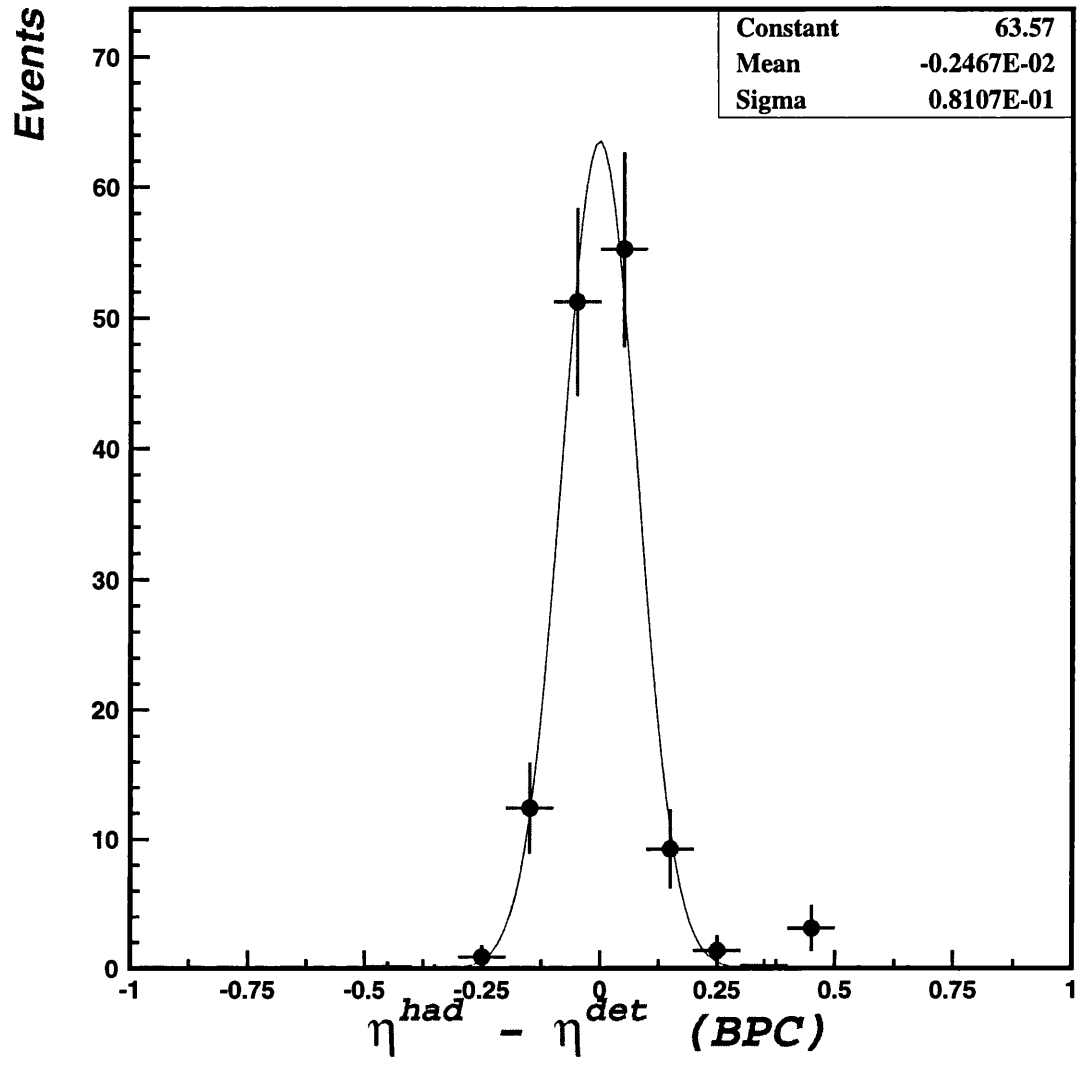

Figure 7.2: Jet pseudorapidity resolution.

0.2, to 0.08 at a hadron level y_{JB} of 0.55. This shift is approximately the same for all three samples of simulated dijet events, and therefore leads to a hadron level range of $0.20 < y_{JB} < 0.55$ whilst the corresponding detector level range is approximately $0.15 < y_{JB} < 0.45$.

The resolution on Q^2 is dependent upon the sample, since Q^2 is measured in different ways for each sample. The photoproduction sample is assumed to have $Q^2 \approx 0$ GeV^2 due to the cross section for quasireal photons dominating the

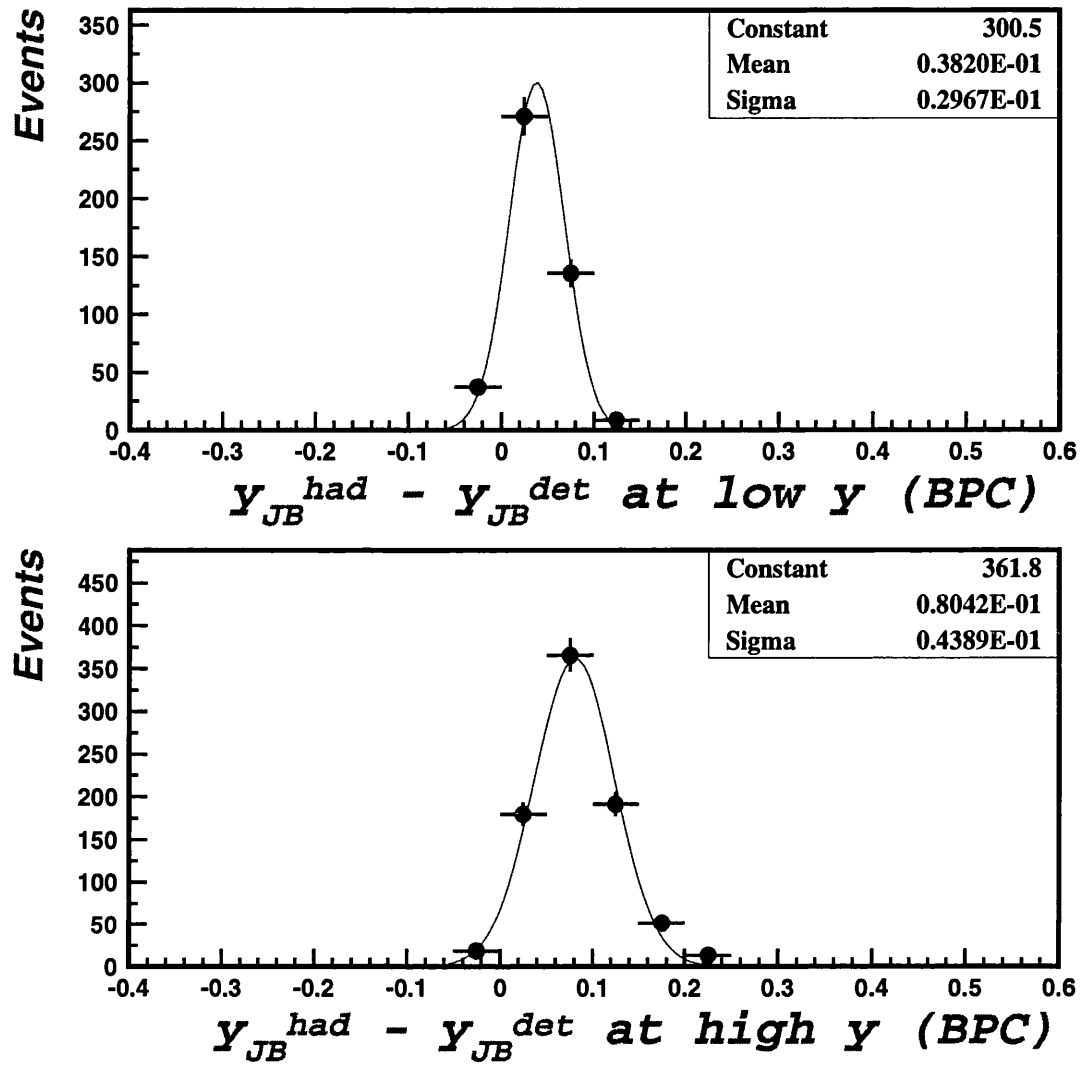

Figure 7.3: y_{JB} resolution for low y_{JB}, where the mean value of y_{JB} is 0.2, and for high y_{JB}, whose mean value of y_{JB} is 0.55.

photoproduction sample. Hence Q^2 is not measured, and a resolution plot does not exist for the photoproduction sample. For the BPC and DIS samples, Q^2 is measured by using the information on the scattered positron's energy and angle of scatter. The BPC sample has the positron measured in the BPC whereas the DIS sample has the positron measured in the main calorimeter. The BPC is specifically designed for good resolution in electron/positron Q^2 measurements

and therefore has a better resolution than the DIS sample. This can be seen by comparing the standard deviation of the Q^2 resolution plot for the BPC sample (figure 7.4) with that for the DIS sample (figure 7.5).

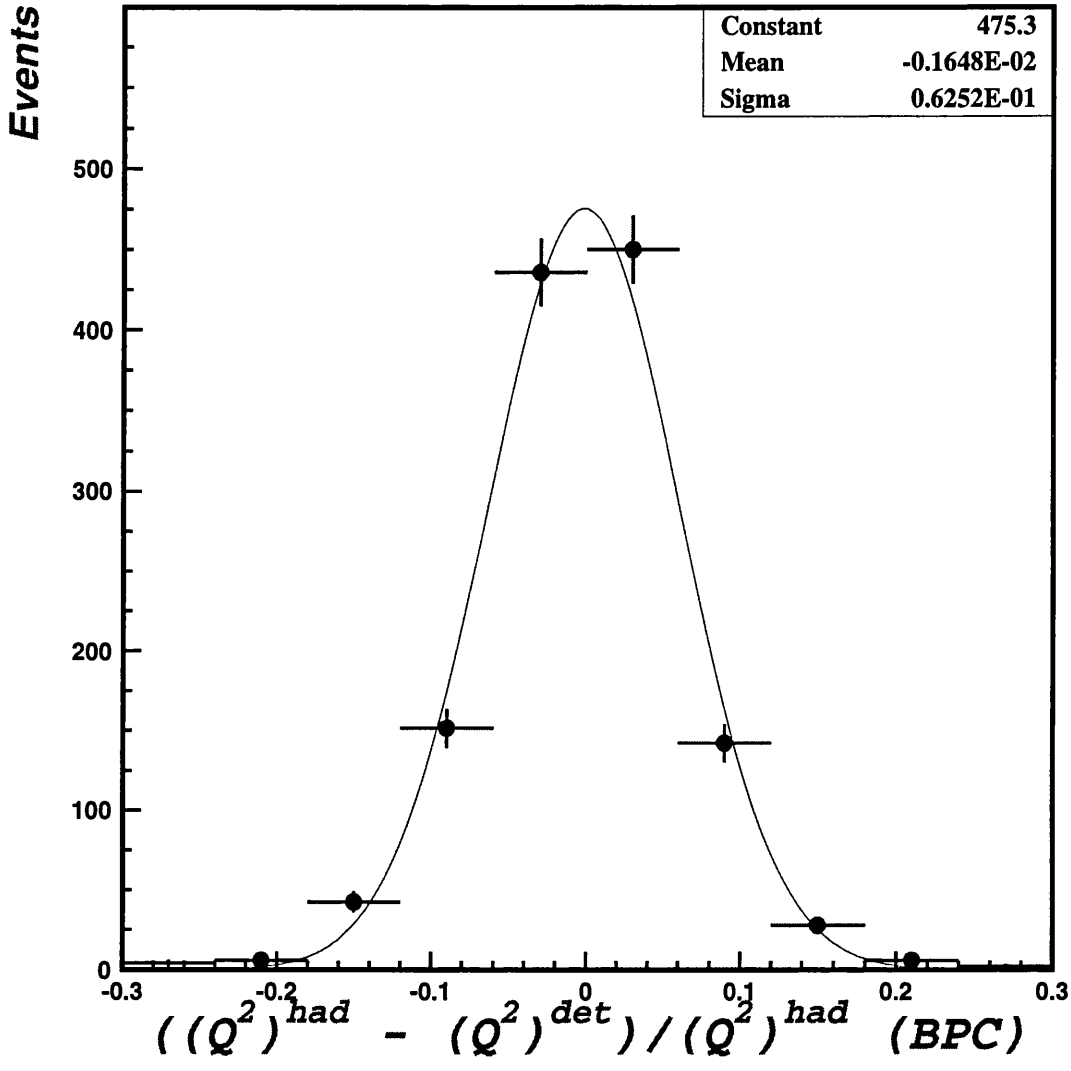

Figure 7.4: Q^2 resolution for the BPC sample.

The measurement of x_γ^{obs} has a different resolution between the three samples. The variation is not large, but does depend on the sample in question. This is because it can be affected by misidentification of the scattered positron. Such misidentification will affect the jets found and the calculation of y_{JB}. For the

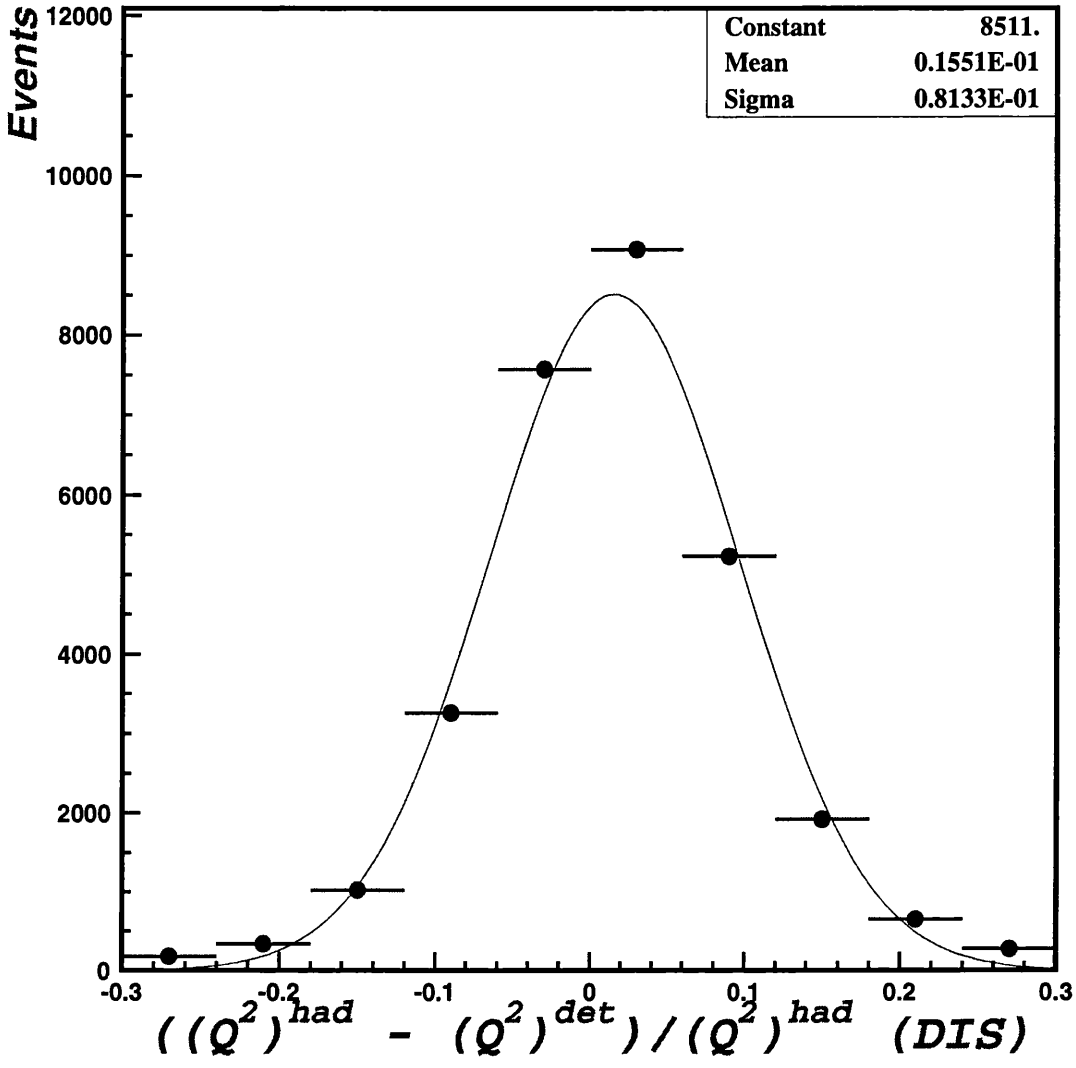

Figure 7.5: Q^2 resolution for the DIS sample.

photoproduction sample, misidentification can lead to the scattered positron depositing energy in the main calorimeter. The BPC sample has the best positron identification, and therefore its sample is purer and not so affected by any misidentified positrons. Finally, the DIS sample relies on identifying a scattered positron in the main calorimeter, and then removing the energy deposited by that positron before any further calculations. Misidentification of the positron or less than perfect removal of its energy deposit will affect the resultant x_γ^{obs}

distribution. However, such effects are not too large, as can be seen from the resolution plots for the three samples in figures 7.6, 7.7 and 7.8.

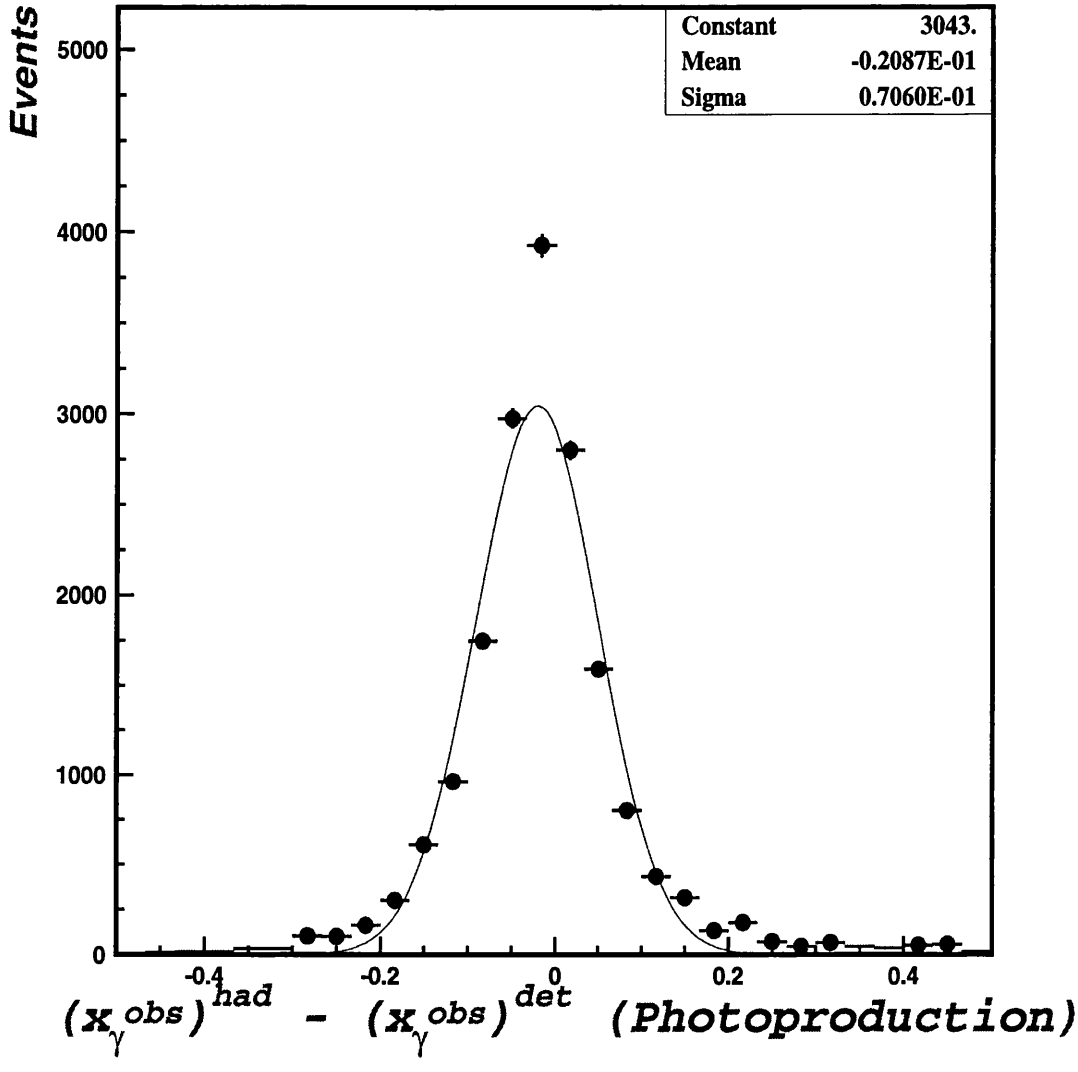

Figure 7.6: x_γ^{obs} resolution for the photoproduction sample.

7.2 Data Correction Method

To determine the hadron level cross section, the data must be corrected for detector effects. The detector level data are subject to mismeasurements due

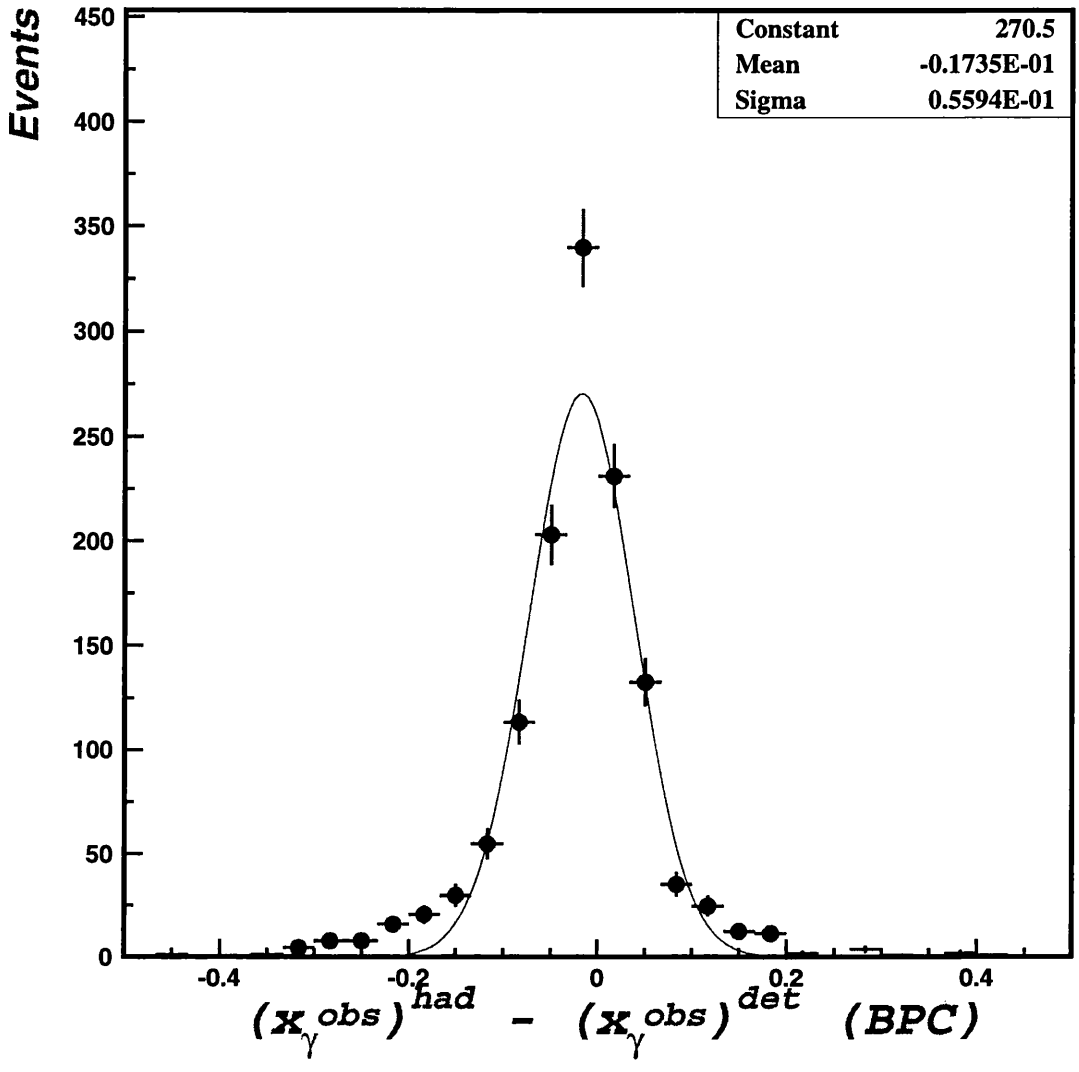

Figure 7.7: x_γ^{obs} resolution for the BPC sample.

to, for example, dead material or granularity of the detector. An example of the uncorrected detector level differential cross section for the BPC sample, with respect to x_γ^{obs}, $d\sigma/dx_\gamma^{obs}$ is shown in figure 7.9.

The uncorrected data are unfolded back to the hadron level by means of a bin-by-bin correction procedure. This involves understanding how many events are measured in each bin of x_γ^{obs} and how many events would have been measured there, given a perfect detector measurement. This is done by using the HERWIG

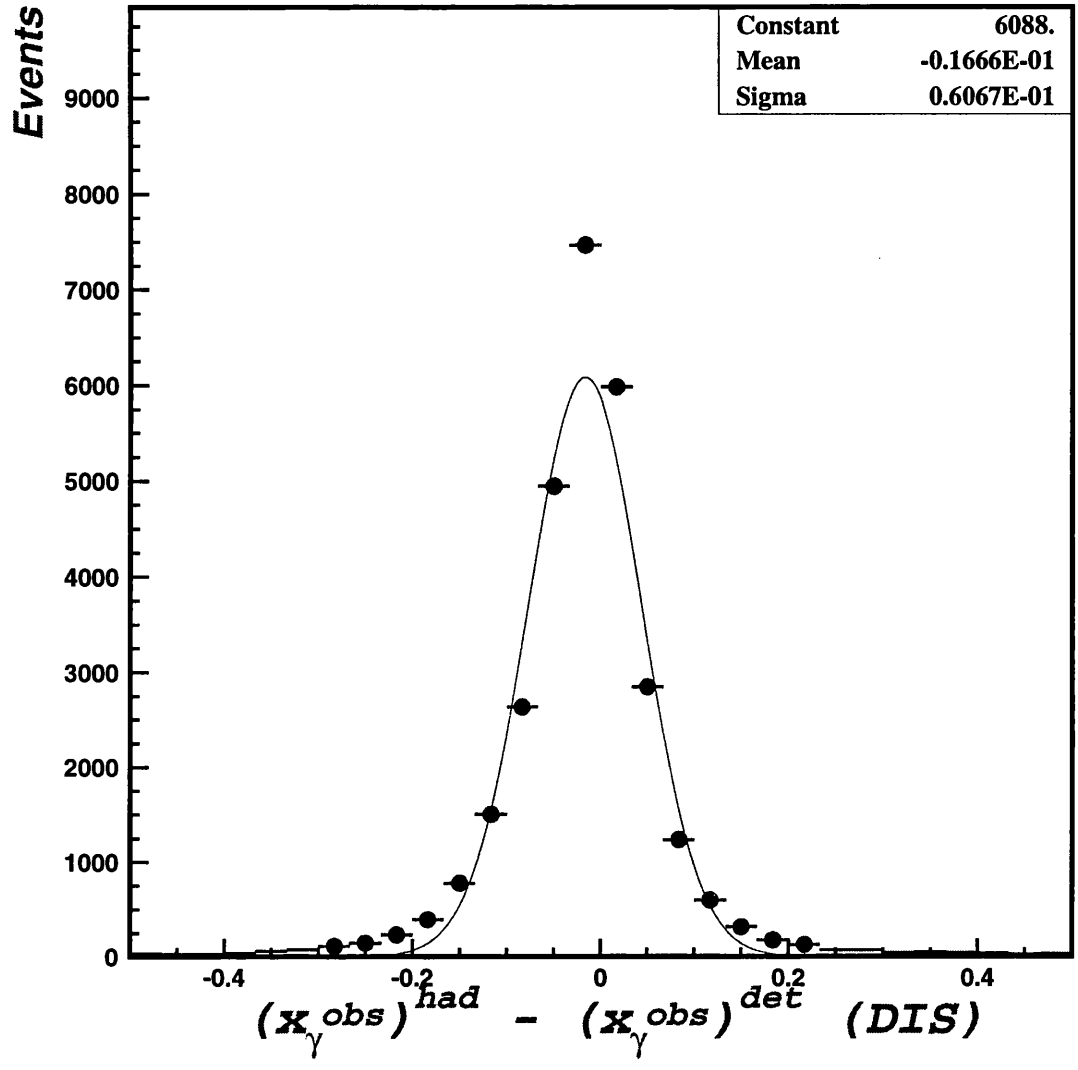

Figure 7.8: x_γ^{obs} resolution for the DIS sample.

Monte Carlo sample to calculate the efficiency, ϵ, purity, p, and correction factor, C, in each bin of x_γ^{obs}. For a given bin, i, in x_γ^{obs}, the efficiency and purity are given by

$$\epsilon(i) = \frac{H(i) \cap D(i)}{H(i)}, \tag{7.1}$$

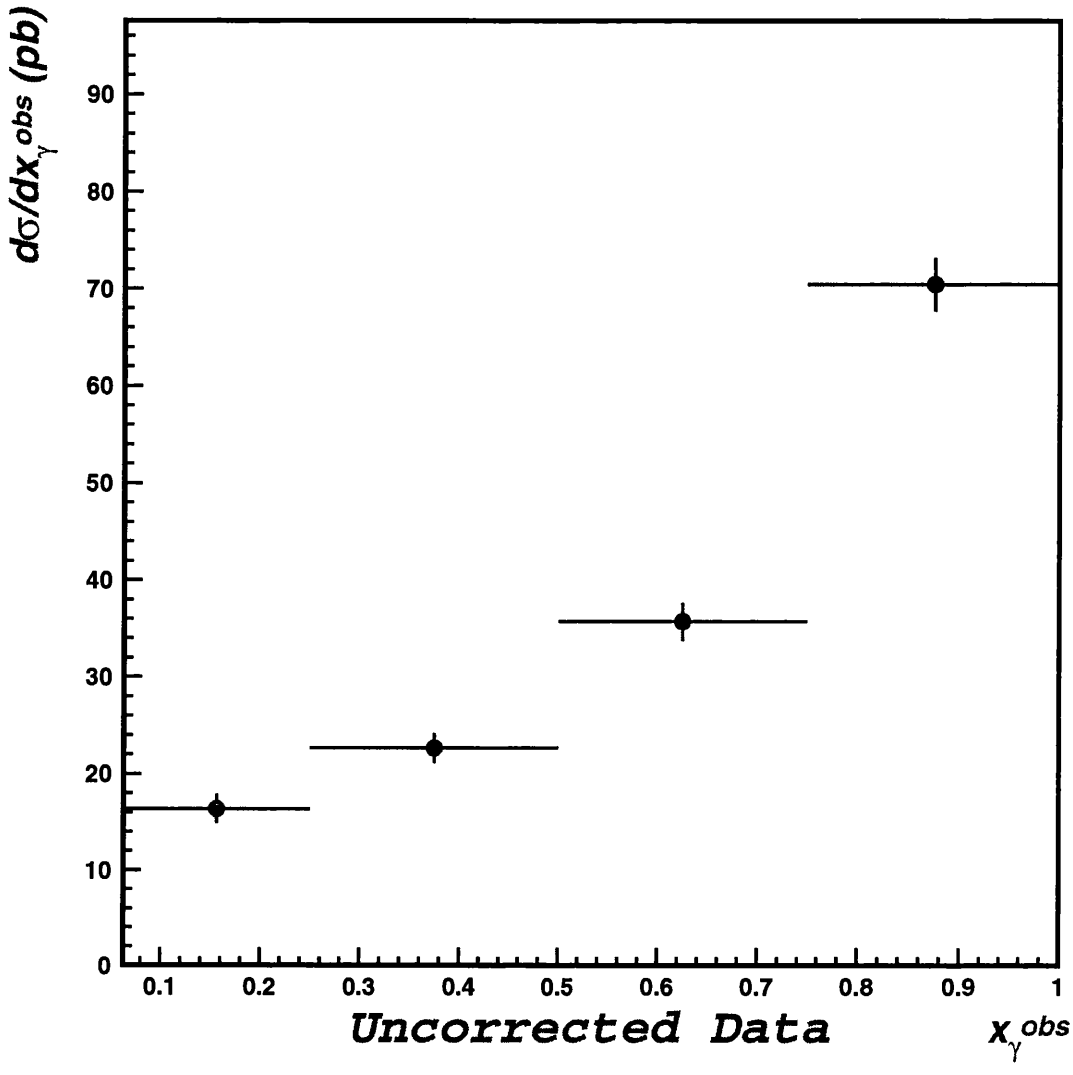

Figure 7.9: Uncorrected detector level $d\sigma/dx_\gamma^{obs}$ for the BPC sample.

$$p(i) = \frac{H(i) \cap D(i)}{D(i)}, \tag{7.2}$$

where $H(i)$ is the number of hadron level events in a given bin i that pass the cross-section cuts. $D(i)$ is the number of detector level events in a given bin i which pass the data selection criteria. The quantity, $H(i) \cap D(i)$ is the number of events which pass the hadron level criteria *and* pass the data selection cuts for bin i. The efficiency is then the fraction of hadron level events in a given

bin which are also measured there at detector level in that bin, and the purity is the fraction of events measured at detector level in a given bin which are also measured there at hadron level in that bin.

The correction factor is related to the purity and efficiency by the following expression

$$C(i) = \frac{p(i)}{\epsilon(i)} = \frac{H(i)}{D(i)} \tag{7.3}$$

Taking the distribution in figure 7.9, the corresponding efficiency, purity and correction factor as a function of x_γ^{obs} is shown in figures 7.10, 7.11 and 7.12 respectively.

Both the efficiency and purity increase for higher x_γ^{obs}. This is due to the fact that higher x_γ^{obs} events have more energy available to the dijet system, and such events are then not so sensitive to the cut on transverse energy, since these events generally have higher transverse energy jets, and are further away from the cut. The correction factors for each bin in x_γ^{obs} reveal the fact that events with high x_γ^{obs} are slightly better measured than for events with lower values of x_γ^{obs}. This is because the jets in high x_γ^{obs} events tend to have more transverse energy than low x_γ^{obs} events. Mismeasurement of a jet's E_T is then less likely to have the event removed from the sample, the deviation from the mean E_T being above the cut on E_T more often than in the case of low x_γ^{obs} events. The correction factors vary between approximately 20 and 35. This is mainly due to the geometric acceptance of the fiducial area of the BPC, which means that there are between 20 and 35 as many events generated in the y and Q^2 range as can be measured with the BPC.

This unfolding procedure then leads to the corrected $d\sigma/dx_\gamma^{obs}$ distribution as shown in figure 7.13. The errors on the corrected data for a particular bin are calculated using the following formula.

For each bin there is a correction factor (A/B). A is the sum of two statistically

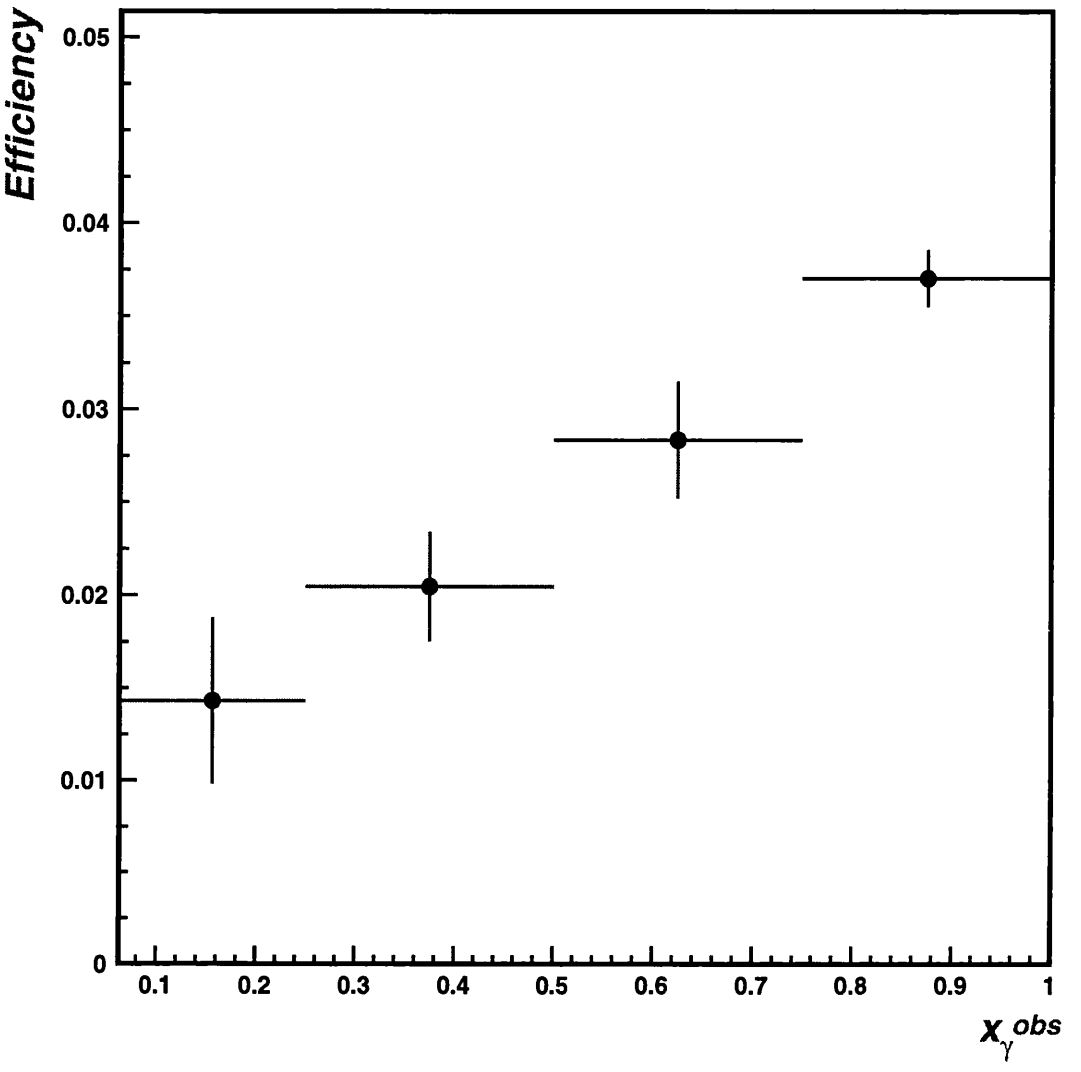

Figure 7.10: Efficiency plot for $d\sigma/dx_\gamma^{obs}$ for the BPC sample.

independent numbers C+D and B is the sum of two statistically independent numbers C+E, where

C is the number of events generated and found in the bin

D is the number of events generated and not found in the bin

E is the number of events not generated but found in the bin

The correction factor is of the form (C+D)/(C+E) with C,D,E statistically

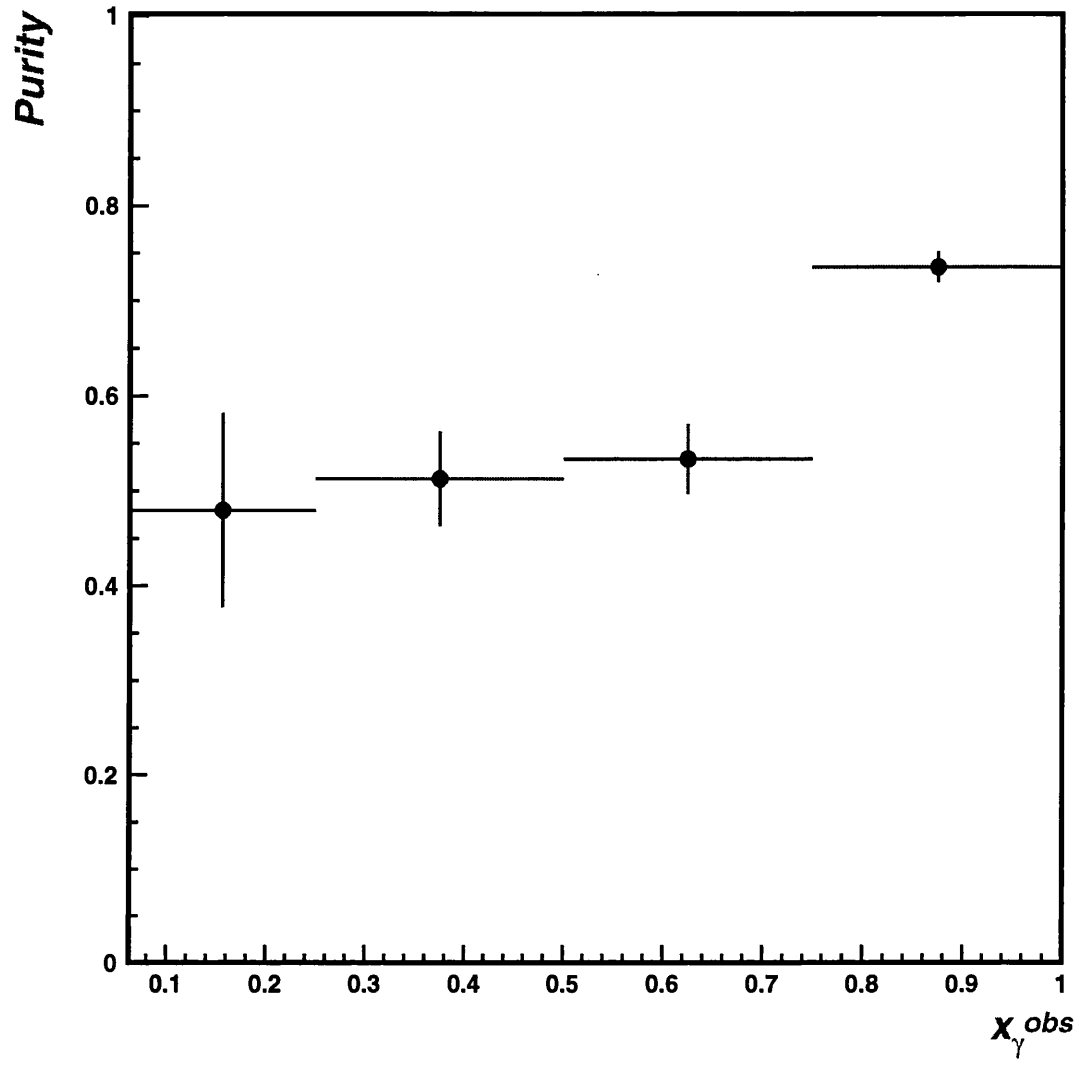

Figure 7.11: Purity plot for $d\sigma/dx_\gamma^{obs}$ for the BPC sample.

independent. The error on this factor is then

$$\Delta\left(\frac{C+D}{C+E}\right) = \frac{1}{(C+E)^2}\{(C+E)^2(V(C)+V(D)) + (C+D)^2(V(C)+V(E)) \\ -2(C+D)(C+E)V(C)\}^{\frac{1}{2}}$$

where the 'number of events' belonging to one of the sets C, D or E is actually the sum of the weights (w_i) of each event in that sample. So for sample C, $C = \Sigma_i w_i(C)$, and $V(C) = \Sigma_i w_i^2(C)$ is the variance of the mean of sample C. The number of events and variance for samples D and E are defined in the same way.

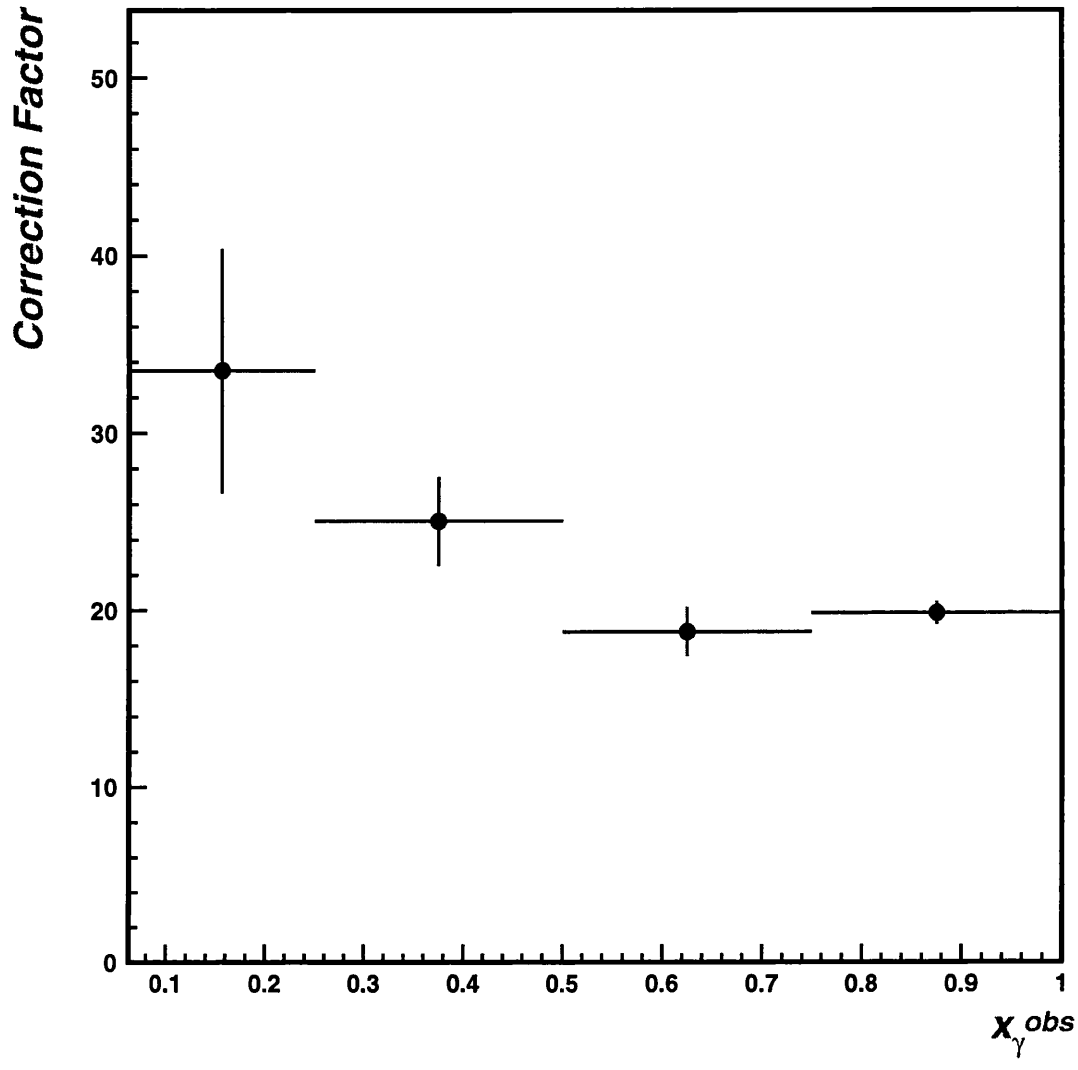

Figure 7.12: Correction factors for $d\sigma/dx_\gamma^{obs}$ for the BPC sample.

The final corrected data is presented as a differential cross section, $d\sigma/dx_\gamma^{obs}$ for different Q^2 ranges, together with the above statistical errors, and is shown in figure 7.14.

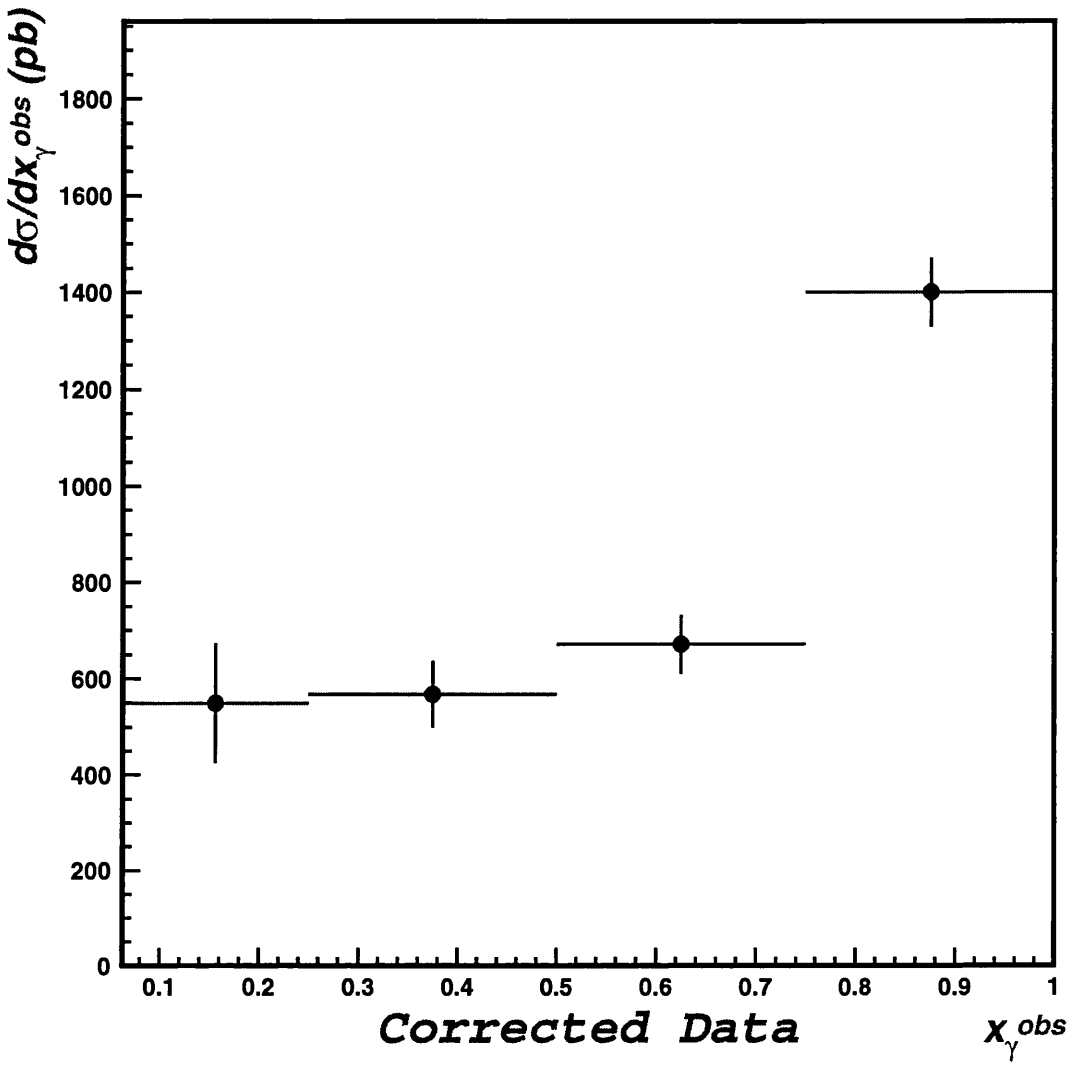

Figure 7.13: Corrected $d\sigma/dx_\gamma^{obs}$ for the BPC sample.

7.3 Systematic Checks

The data can be corrected for mismeasurement due to detector effects, and errors as described above are assigned to the corrected data. These errors are however statistical, and depend on the number of Monte Carlo events available, and the number of data events measured. It is also possible that the measured quantities are systematically mismeasured. To estimate the effect of such systematic mismeasurements, each variable which is cut on to select the data sample has the

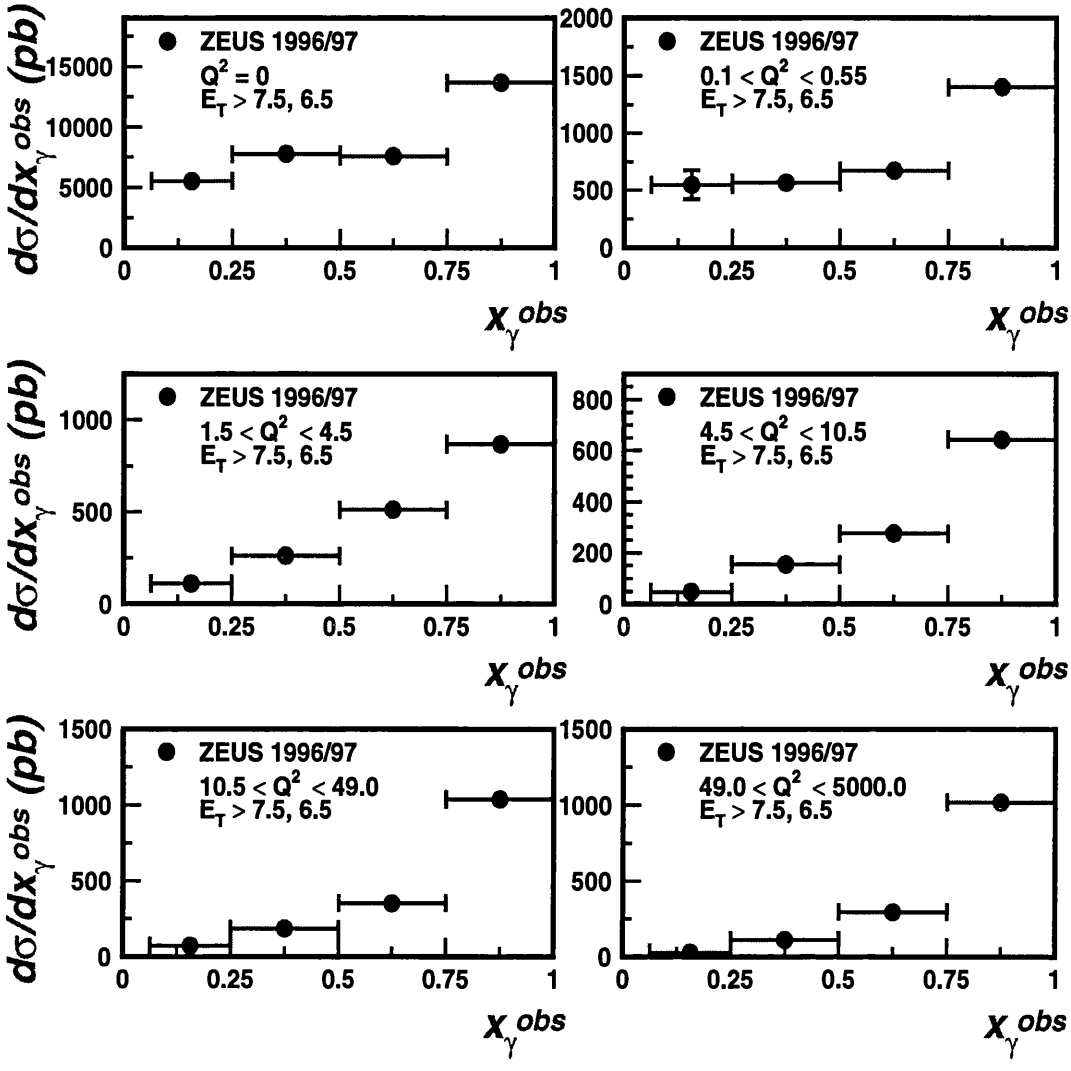

Figure 7.14: Corrected $d\sigma/dx_\gamma^{obs}$ for all ranges in Q^2 accessed in this analysis. Q^2 is measured in units of GeV^2 and transverse energies in GeV.

cut varied by one standard deviation on that variable, as defined by a gaussian fit to the resolution, both up and down. This is a mismeasurement effect at the detector level only, so the detector level cuts are varied, whilst the hadron level cuts remain the same. Most systematic checks lead to some change in the corrected cross sections. These variations of the corrected cross sections are then added in quadrature, and finally the total systematic error is added in quadrature

with the statistical error.

The exception to this is those systematic checks which are correlated between bins. It would be wrong to add correlated systematics in quadrature with uncorrelated ones. Checks such as varying the energy scale of the calorimeter lead to the cross sections increasing everywhere. Such correlated systematics are added in quadrature but shown separately. This is because these systematics affect the overall normalisation of a cross section distribution, rather than the shape.

The following is the list of systematic checks performed, most of them involving the variation by one standard deviation (σ) of the detector level cut for the following variables (some variables such as electron energy and position are not used for the photoproduction sample, and hence do not apply to that sample)

1. Jet transverse energy cut is lowered by one $\sigma(E_T)$.
2. Jet transverse energy cut is raised by one $\sigma(E_T)$.
3. Jet pseudorapidity cuts are lowered by one $\sigma(\eta)$.
4. Jet pseudorapidity cuts are raised by one $\sigma(\eta)$.
5. z vertex cuts are lowered by one $\sigma(z\ vertex)$.
6. z vertex cuts are raised by one $\sigma(z\ vertex)$.
7. y_{JB} cuts are lowered by one $\sigma(y_{JB})$.
8. y_{JB} cuts are raised by one $\sigma(y_{JB})$.
9. x_γ^{obs} cuts are lowered by one $\sigma(x_\gamma^{obs})$. Distributions plotted versus x_γ^{obs} have the data distribution split into four almost equal width bins in x_γ^{obs}. This binning then serves as a set of cuts dividing up the sample into four separate samples. The systematic effect of a mismeasurement of x_γ^{obs} is then

determined by varying all bin separation values by one standard deviation on the x_γ^{obs} resolution.

10. x_γ^{obs} cuts are raised by one $\sigma(x_\gamma^{obs})$.

11. Q^2 cuts are lowered by one $\sigma(Q^2)$. This is also a variable which is split into bins and is treated in a similar fashion to x_γ^{obs}.

12. Q^2 cuts are raised by one $\sigma(Q^2)$.

13. Scattered positron energy cut is lowered by one $\sigma(E'_e)$.

14. Scattered positron energy cut is raised by one $\sigma(E'_e)$.

15. Scattered positron position in x cuts are lowered by one $\sigma(x'_e)$.

16. Scattered positron position in x cuts are raised by one $\sigma(x'_e)$.

17. Scattered positron position in y cuts are lowered by one $\sigma(y'_e)$.

18. Scattered positron position in y cuts are raised by one $\sigma(y'_e)$.

19. Energy scale of the calorimeter is lowered by 5%. The uncertainty in the energy measurements in the calorimeter have been determined using information from the CTD in comparison with the calorimeter information [48]. This uncertainty in the energy scale is at most $\pm 5\%$.

20. Energy scale of the calorimeter is raised by 5%.

21. Luminosity measurement is lowered by 1.5%. There is at present a 1.5% uncertainty in the luminosity calculation.

22. Luminosity measurement is raised by 1.5%.

23. Correcting with a Monte Carlo with different hadronisation model. This means correcting the data with PYTHIA 6.1 instead of HERWIG 5.9, to

see how the correction procedure depends upon the hadronisation model used in the Monte Carlo.

Those systematic checks which fall under the category of correlated systematics are the energy scale of the calorimeter (numbers 19 and 20) and the luminosity uncertainty (numbers 21 and 22). These are then the systematics which are shown separately from the rest. The rest are all uncorrelated and are hence added in quadrature.

A graphical representation of how corrected cross section measurements (including a particular systematic mismeasurement) differ from the nominal result can be seen in figures 7.15 and 7.16, where the former is for a low bin in x_γ^{obs} (a resolved-enriched sample) and the latter is for a high bin in x_γ^{obs} (direct-enriched sample), both as a function of increasing Q^2. The error bars indicate the statistical error on the corrected measurement for each systematic.

7.3.1 Initial State Radiation

Initial state radiation (ISR) of a photon from the incoming positron before it interacts with the proton will affect measurements of Q^2 and y. Typically such a photon travels collinear with the positron beam and effectively reduces the initial lepton beam energy to be less than 27.5 GeV. There is as yet no Monte Carlo generator which simulates resolved photon processes and includes radiative corrections, however, the effect of ISR can be estimated using direct events only. DJANGOH is a recently updated version of DJANGO6 [49], which combines a DIS Monte Carlo generator with a simulation of radiative effects. Using this, for the kinematical range accessed in this analysis, the mean ISR photon energy is determined to be 1.8 GeV. This translates as an effective reduction in lepton beam energy from 27.5 GeV to 25.7 GeV. The effect on Q^2 and y is such that

$$\frac{\Delta Q^2}{Q^2} = \frac{E_\gamma^{ISR}}{E_e} \tag{7.4}$$

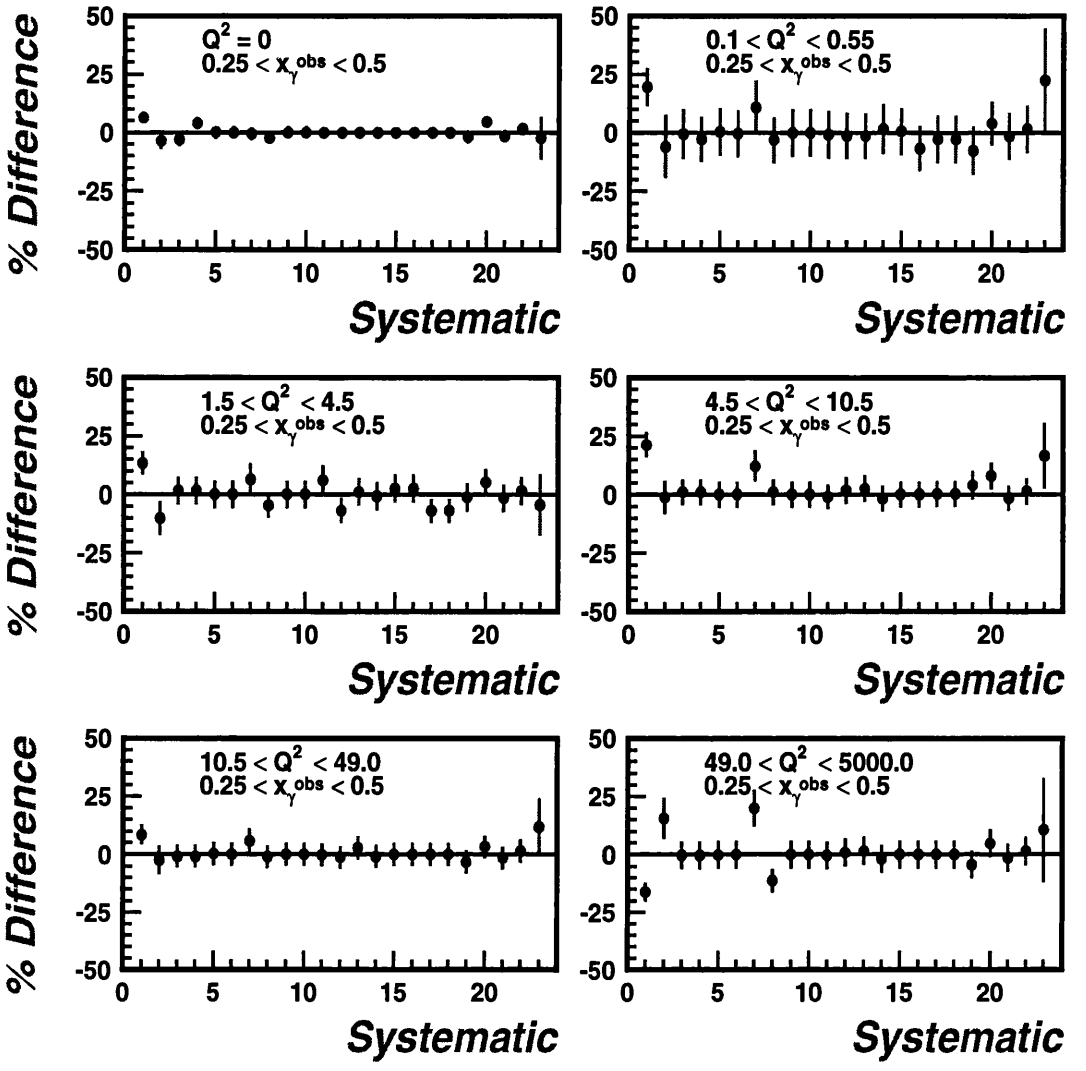

Figure 7.15: The % difference between the corrected cross section as measured including each systematic and that of the nominal result without any systematic effects included, as a function of each systematic number. The x_γ^{obs} bin is chosen such that the events are typically resolved-enriched events. Q^2 is measured in units of GeV^2.

$$\Delta y = \frac{E_\gamma^{ISR}}{E_\gamma^{ISR} - E_e}(1 - y) \tag{7.5}$$

where E_e is the initial energy of the positron before ISR (27.5 GeV), E_γ^{ISR} is the energy of the ISR photon emitted and ΔQ^2 and Δy are obtained by subtracting

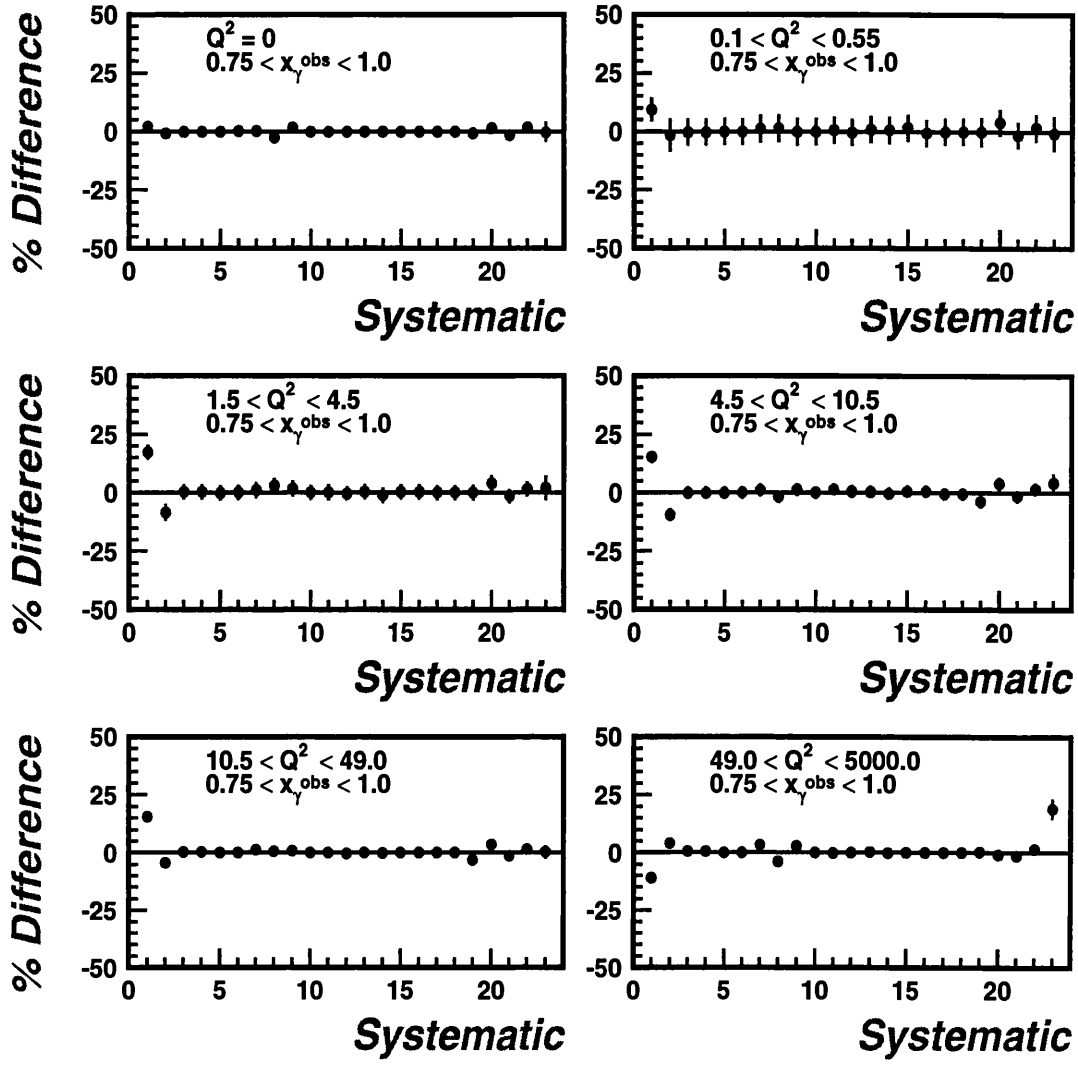

Figure 7.16: The % difference between the corrected cross section as measured including each systematic and that of the nominal result without any systematic effects included, as a function of each systematic number. The x_γ^{obs} bin is chosen such that the events are typically direct-enriched events. Q^2 is measured in units of GeV^2.

the mismeasured variable from the true value. Inserting 1.8 GeV for E_γ^{ISR} and 0.2 for y to obtain the maximal effect, the fractional change in Q^2 is approximately 6.5%, and the absolute change in y is approximately 5.5%. These figures are almost equal to the width of the resolution on these variables as simulated by a Monte Carlo without ISR. The effect of non-simulation of ISR leads to an

overestimation of both Q^2 and y. The effect is comparable to the systematic checks 7 and 11 where the cuts on Q^2 and y are reduced by the width of the resolution. However, a rigorous treatment of the effect on the final measurements would require a simulation of ISR for both resolved and direct photon interactions. Since no such generator exists, the data are not corrected for this effect and it is not included in the systematic error, as in a similar analysis by the H1 collaboration [50].

Chapter 8

Results and Interpretation

8.1 Corrected Differential Cross Sections

The cross sections which are presented in this chapter have all been corrected for detector effects, and both statistical and systematic errors are included. Such distributions provide information on the structure of the virtual photon as measured for different kinematic regions of phase space. These distributions are then also compared with hadron level Monte Carlo predictions which contain both real and virtual photon parton density functions. In this manner it is possible to distinguish between models of the photon which can describe the measured data and those which do not describe the data. Tables of the corrected data including statistical and systematic errors are shown in appendix B.

8.1.1 $d\sigma/dx_\gamma^{obs}$ as a function of Q^2

The corrected data distributions for $d\sigma/dx_\gamma^{obs}$ for different Q^2 bins is shown in figure 8.1. The inner error bars are the statistical uncertainty, the outer error bars are the statistical and uncorrelated systematic errors added in quadrature. The shaded band is the correlated errors added in quadrature. The lower x_γ^{obs} region, or resolved-enriched region ($x_\gamma^{obs} < 0.75$), can be seen to decrease with

increasing Q^2.

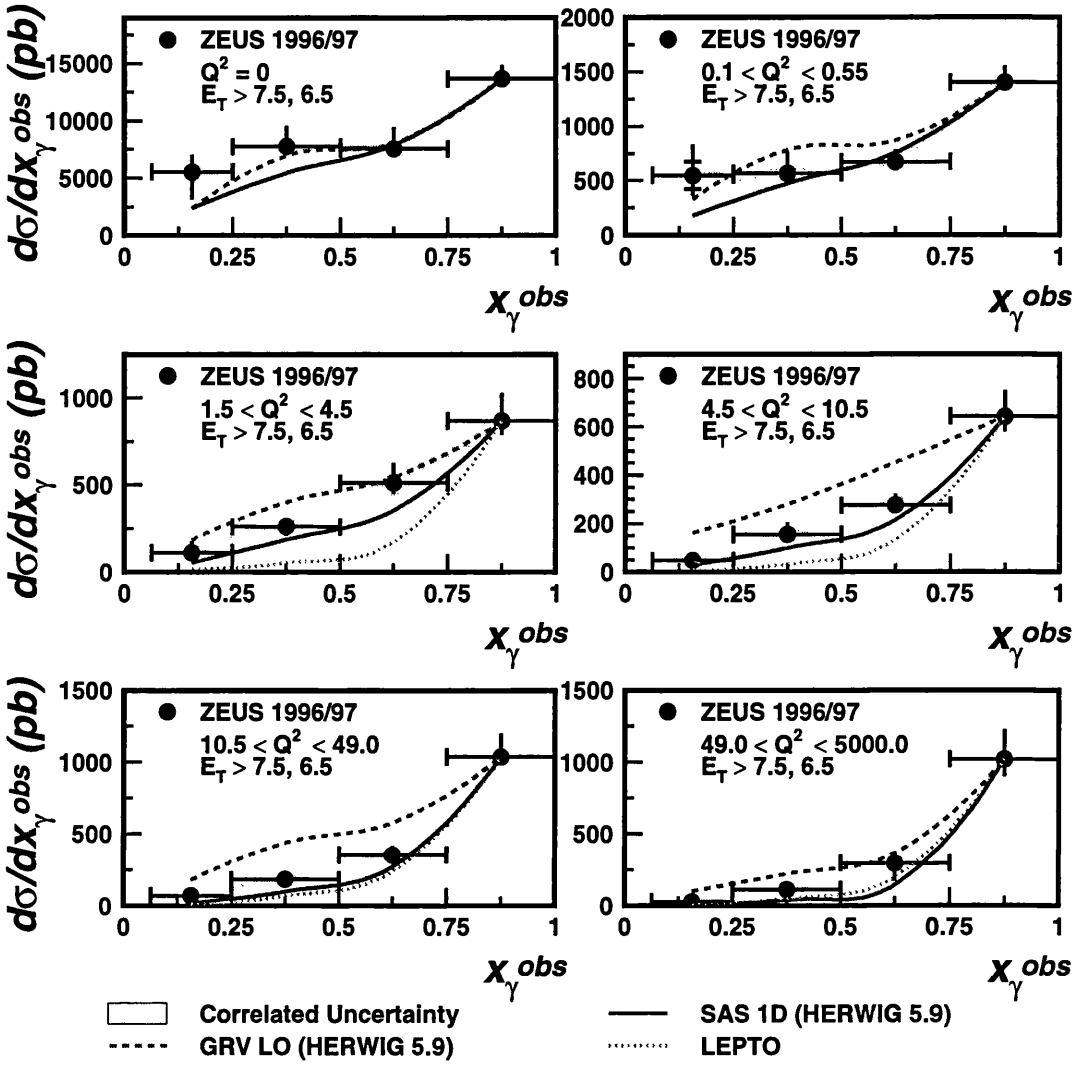

Figure 8.1: $d\sigma/dx_\gamma^{obs}$ for increasing Q^2, starting with the photoproduction regime, then BPC, and continuing into the DIS region. Q^2 is measured in units of GeV^2 and transverse energies in GeV.

Two of the theory curves superimposed on the cross section plots are the cross sections as given by HERWIG 5.9 with GRV LO and SaS1D photon PDFs. GRV LO is a real photon PDF, and is expected to describe the photoproduction data, but *not* expected to describe the virtual photon data, and is presented here only as a means of checking that there is a suppression of the resolved photon as

its virtuality increases. SaS1D, however, does have a relative suppression of the resolved component with increasing Q^2. Both curves (and indeed all following theory curves) have been scaled to fit the direct-enriched peak ($x_\gamma^{obs} > 0.75$) in order to compare shapes, since the raw cross sections do not match the data. Tables of the factors by which these cross sections have been scaled can be found in appendix A, as can the factors for all following theory curves presented below. The data show a decrease in low x_γ^{obs} as Q^2 increases. Apart from the photoproduction region, the GRV LO PDF tends to overestimate the resolved component, whereas the SaS1D PDF typically agrees with or lies below the data. The third curve appears only for the DIS samples and is the prediction of LEPTO 6.5 [53], which is a DIS Monte Carlo only, and has no resolved process simulated. This curve lies below the data, but does show a non-zero cross section for low x_γ^{obs}.

The fall of the resolved photon contribution to the cross section as a function of Q^2 can be more easily seen in a plot of the ratio of $d\sigma/dx_\gamma^{obs}$ for $x_\gamma^{obs} < 0.75$ to that of $d\sigma/dx_\gamma^{obs}$ for $x_\gamma^{obs} > 0.75$, that is the ratio of resolved-enriched over direct-enriched cross sections. This ratio is shown in figure 8.2. Since the absolute normalisation of the HERWIG 5.9 cross sections is known to be different from the data, it is the shape of the theoretical cross sections which indicate whether the PDF is adequate in describing the data. A good match of shape between theory and data would indicate that the PDF is a good model of the data, despite the absolute normalisation. Another advantage of plotting the ratio of cross sections is that the systematic errors are expected to be reduced. The difference in the corrected result (which includes a particular systematic mismeasurement) from the nominal result for this ratio is shown in figure 8.3. This can be compared with the similar plot for the absolute cross section (figures 7.15). It is worth noting that the systematic effects due to varying the jet transverse energy cuts (systematics 1 and 2) and the energy scale (systematics 19 and 20) are generally smaller for the ratio than in the absolute cross section. The luminosity uncertainty (systematics

21 and 22) is applied by multiplying the cross section by a factor, and therefore cancels exactly in a ratio of cross sections. As can be seen, it has no effect on the ratio.

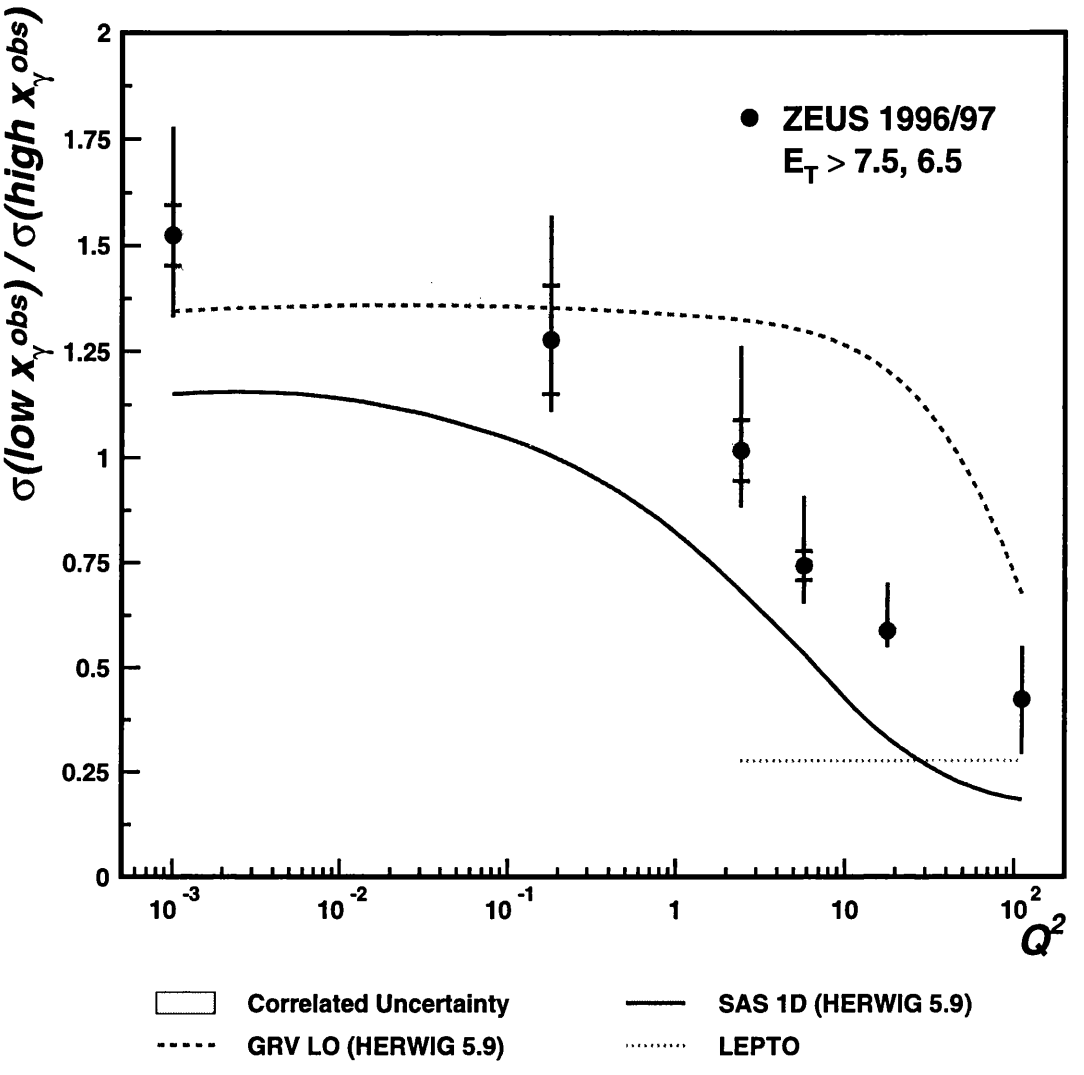

Figure 8.2: Ratio of resolved-enriched to direct-enriched cross sections as a function of photon virtuality, Q^2. Q^2 is measured in units of GeV^2.

The SaS1D PDF appears to better describe the data in shape. The GRV LO PDF is designed for real photons, and is a useful check that the choice of variable, x_γ^{obs}, is a good one, since the ratio of resolved to direct remains constant with

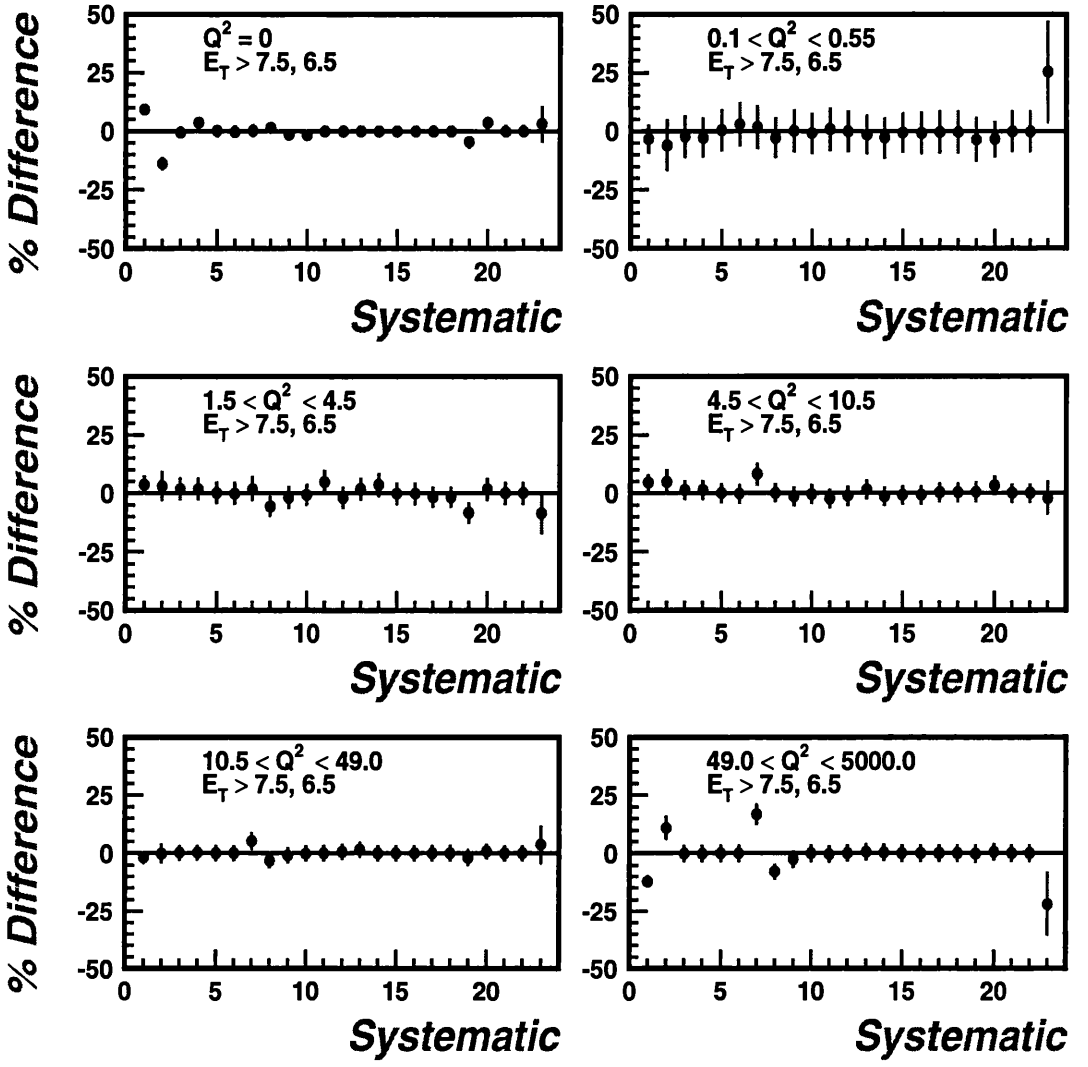

Figure 8.3: The % difference between the corrected cross section as measured including each systematic and that of the nominal result without any systematic effects included, as a function of each systematic number for the ratio of $d\sigma/dx_\gamma^{obs}$ for $x_\gamma^{obs} < 0.75$ to that of $d\sigma/dx_\gamma^{obs}$ for $x_\gamma^{obs} > 0.75$. Q^2 is measured in units of GeV^2 and transverse energies in GeV.

respect to Q^2, except for the highest Q^2 bin which favours more direct events due to the transverse energy boost on the jet system. Hence a non-zero gradient of the ratio up to a Q^2 of 49 GeV^2 implies a reduction in structure as Q^2 increases. The LEPTO curve lies below the data and is flat. This is again a good check

that the gradient of the curve implies a reduction in resolved events with Q^2. Since LEPTO has no resolved component, it is expected to be flat. It lies below the data, which means that the data cannot be described by such a DIS Monte Carlo alone, but rather require a resolved photon process to better approximate the data in this Q^2 region. The fact that the LEPTO ratio curve is not zero, means that there are events which have similar topology to that of a resolved event, even when it is not. This comes mostly from higher order effects such as three-jet events, where the third jet has significant $E - p_z$, and can bring x_γ^{obs} down below the 0.75 separation cut.

These theoretical curves can also have the effect of multi-parton interactions included. The effect of multi-parton interactions (MIs) is to increase the resolved-enriched or lower x_γ^{obs} cross section. This is because the jets now sit on an underlying event and have more transverse energy. More resolved events will then pass the transverse energy cut and lead to a higher cross section for the resolved-enriched cross section. In the ratio plot, this shows up as a normalisation difference for the GRV LO PDF, but does not change the shape of the ratio. The SaS1D PDF is not so sensitive to the effect of MIs. This is partly because the resolved component is suppressed, and consequently so is the effect of MIs, but also the model suppresses the VMD part much quicker than the anomalous part, and the implementation of MIs occurs only for the VMD part, not anomalous. Hence the difference between SaS1D with or without MIs is small.

The hadronisation scheme affects the topology of the final state and hence the final cross sections obtained. HERWIG 5.9 and PYTHIA 6.1 have different hadronisation schemes, but the effect of the different hadronisation is that the jets of one Monte Carlo are more likely to be accepted as jets with high enough E_T to pass the E_T cut. Since this will affect the softer jets more than the harder ones, and the resolved sample generally has softer jets, the resolved part of the cross section will be affected more than the direct part. This shows up best in the ratio plot.

The corresponding differential cross sections and ratio plots are shown in 8.4 and 8.5 respectively. The ratio plot best shows how the different hadronisation effects of including MIs or using a different hadronisation scheme such as implemented in PYTHIA 6.1 enhance the resolved part due to greater acceptance for jets from resolved photon events.

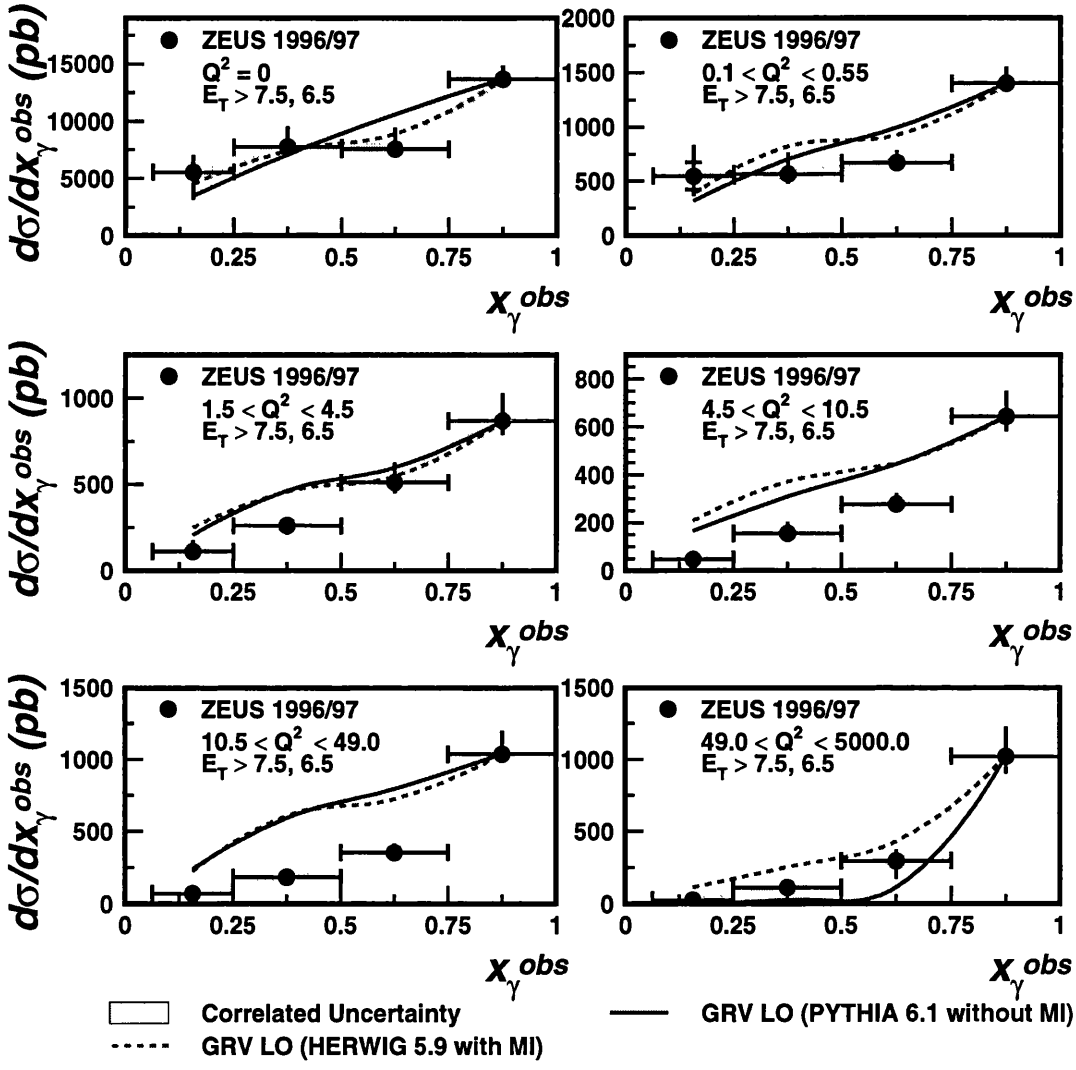

Figure 8.4: $d\sigma/dx_\gamma^{obs}$ for increasing Q^2, starting with the photoproduction regime, then BPC, and continuing into the DIS region. The models now include multi-parton interactions. Q^2 is measured in units of GeV^2 and transverse energies in GeV.

The important feature of the ratio of resolved-enriched to direct-enriched is

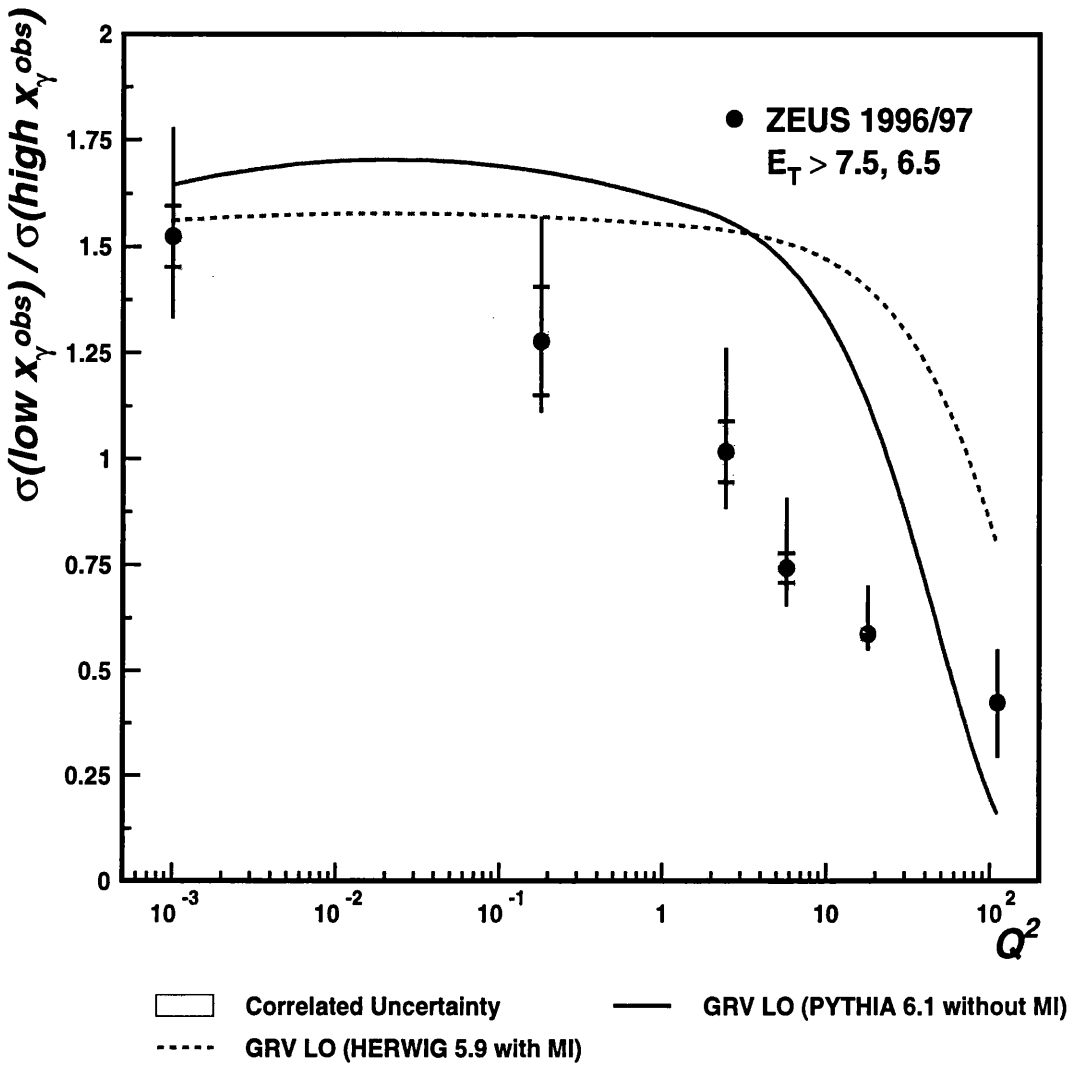

Figure 8.5: Ratio of resolved-enriched to direct-enriched cross sections as a function of photon virtuality, Q^2.The models now include multi-parton interactions. Q^2 is measured in units of GeV^2.

the shape of the curves. Implementing a model with multi-parton interactions, or a different hadronisation scheme changes the magnitude of the curve, but not the shape. The ratio is then more sensitive to the photon PDF (in shape), and can be compared with various models, by comparing shapes, without being very affected by any mismodelling of the data due to the implementation of other hadronisation models.

8.1.2 $d\sigma/dx_\gamma^{obs}$ as a function of Q^2 and E_T^2

The observed structure of the virtual photon does not only depend on its virtuality. The structure may also depend upon the scale of the probe used to probe the structure. The dijets provide the hard scale with which to probe the photon. Whilst in normal DIS it is the virtuality of the photon which provides the scale, Q^2, here the situation is reversed and it is the photon which is being probed, but only if the E_T of the jets is much greater than the virtuality of the photon, which is true for all Q^2 bins except the highest one.

Plotting x_γ^{obs} as a function of E_T of the jets as well as Q^2 has two interesting features. First, there are two scales in the event now. The E_T^2 of the jets and the virtuality of the photon, Q^2. For $E_T^2 >> Q^2$ the dijets are probing the photon structure. As E_T^2 approaches Q^2, it is not possible to say that one system is probing another. Then for $Q^2 >> E_T^2$ the photon is probing the proton. The interplay between these two scales will be apparent by plotting the differential cross section, $d\sigma/dx_\gamma^{obs}$ for a range of Q^2 and E_T^2. The second interesting feature is to observe what happens to the photon structure as the probing scale, E_T^2, increases. One might expect that as the probe scale increases, it will be able to resolve smaller and smaller partons inside the photon. If the direct photon is pointlike, then this is the smallest parton, and the direct peak will increase. If the direct photon has structure, but the probing scale is simply not high enough to resolve this structure, then increasing the probing scale will improve the resolution and lead to a decrease in the direct contribution with a corresponding increase in the relative resolved contribution.

Figures 8.6, 8.7 and 8.8 show these cross sections as a function of x_γ^{obs}, Q^2 for higher cuts on the transverse energy of the jets. Figures 8.9, 8.10 and 8.11 are the corresponding ratios of resolved to direct cross sections.

As before the resolved contribution still decreases with Q^2 for all samples with varying cuts on the jet transverse energies. The effect of increasing the

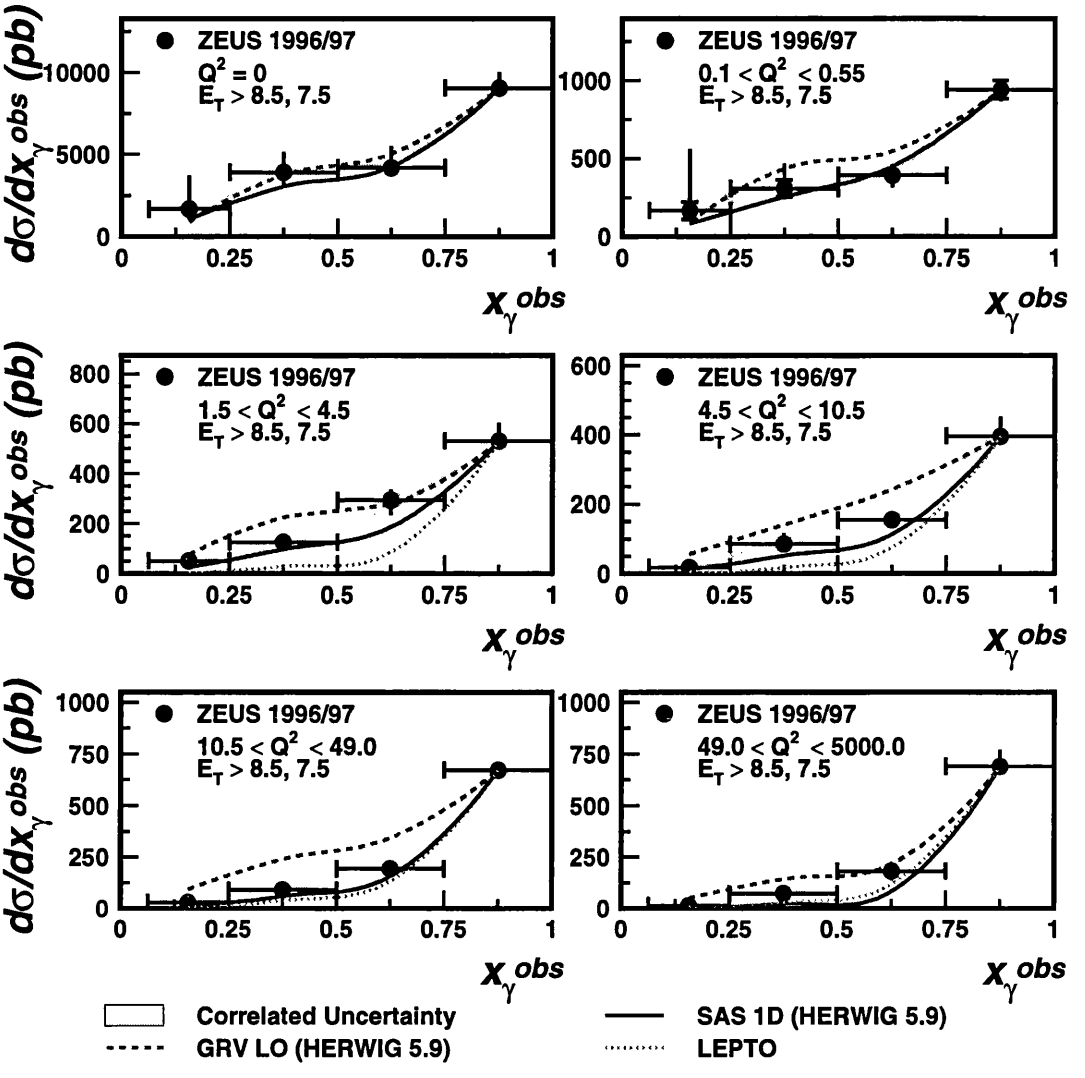

Figure 8.6: The differential cross section $d\sigma/dx_\gamma^{obs}$ for $E_T^{jet} > 8.5, 7.5$ GeV. Q^2 is measured in units of GeV^2.

cut on the jet transverse energies is to increase the average transverse energy of the jets in the sample. This in turn enhances the direct peak in x_γ^{obs} relative to the resolved contribution. It appears that increasing the transverse energy of the jets, and hence the scale of the probe, selects more direct events, suggesting that the direct photon is indeed pointlike, and does not have a structure which is too small for the probe to resolve. However, this is not the entire story. The enhancement of the direct peak is partly due to kinematic effects. In order to

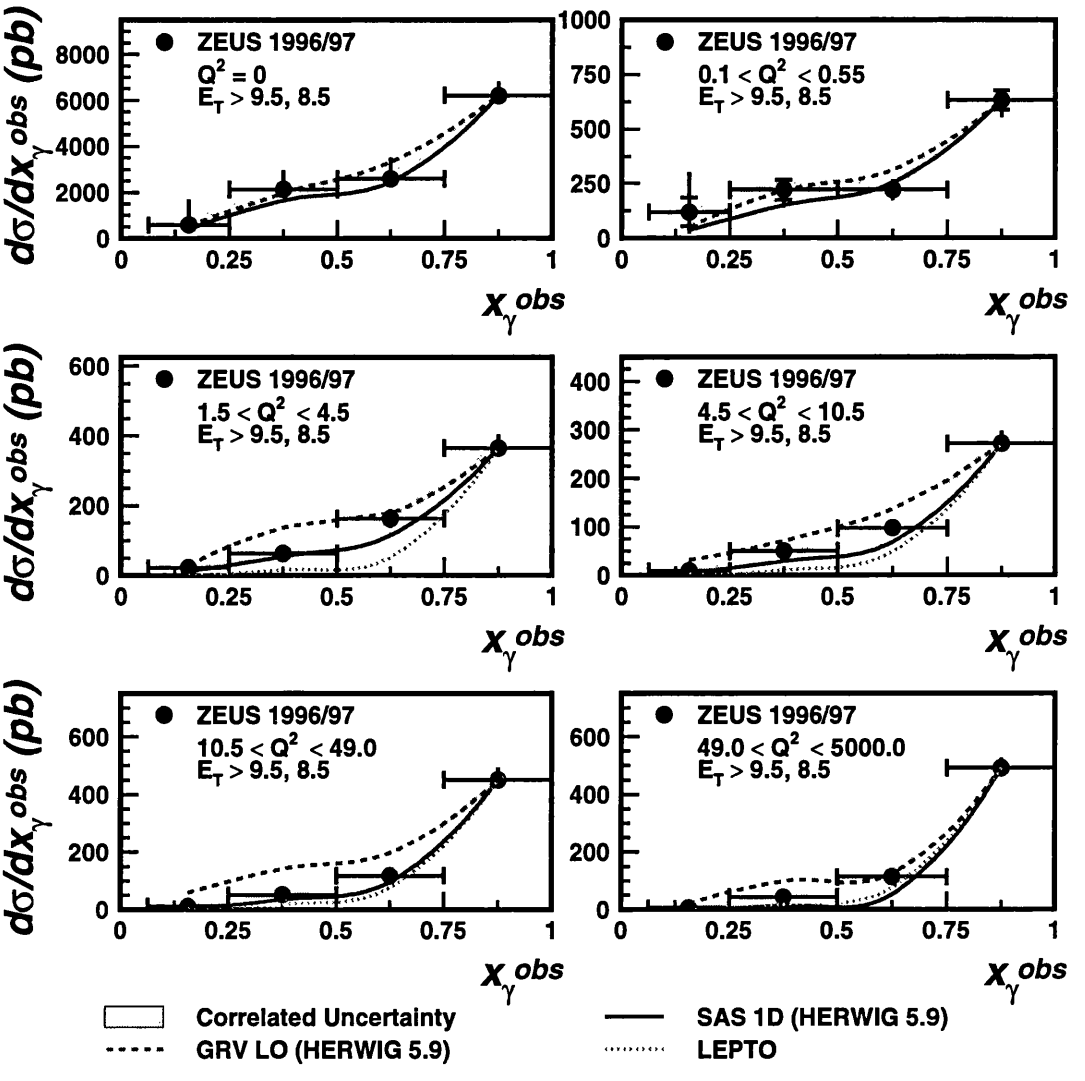

Figure 8.7: The differential cross section $d\sigma/dx_\gamma^{obs}$ for $E_T^{jet} > 9.5, 8.5$ GeV. Q^2 is measured in units of GeV^2.

have higher transverse energy jets, the partons which combine to produce the jets must be more energetic. For a fixed pseudorapidity range, this means an increase in the fractional momentum which the parton from the proton inputs into the dijets, and a corresponding increase in the fractional momentum which the parton from the photon inputs into the dijet system. Consequently, for the same photon energy, x_γ^{obs} must increase.

The ratio of resolved-enriched to direct-enriched cross sections can now be

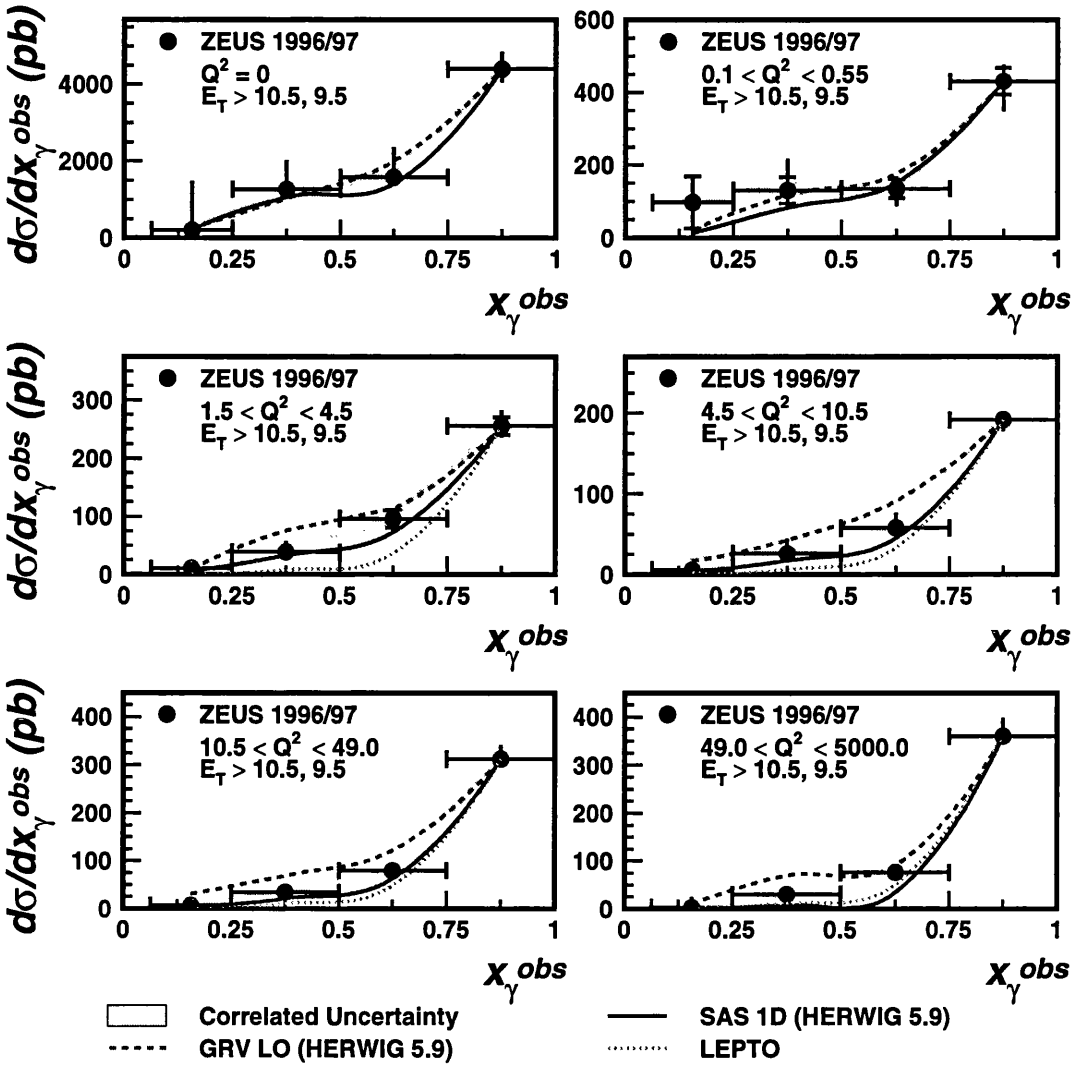

Figure 8.8: The differential cross section $d\sigma/dx_\gamma^{obs}$ for $E_T^{jet} > 10.5, 9.5$ GeV. Q^2 is measured in units of GeV^2.

plotted as a function of $(\overline{E_T^{cut}})^2$, the average of the two cuts on the transverse jet energy. As an example, the sample with cuts at 6.5 and 7.5 GeV would then have an $\overline{E_T^{cut}}$ of 7 GeV, and an $(\overline{E_T^{cut}})^2$ of 49 GeV^2. The plot can be seen in figures 8.12 for the six different Q^2 bins. The GRV LO and SaS1D PDFs convoluted with HERWIG 5.9 are superimposed, as is the curve for LEPTO 6.5. Similarly figure 8.13 has GRV LO convoluted with PYTHIA 6.1 and GRV LO convoluted with HERWIG 5.9 with MIs switched on.

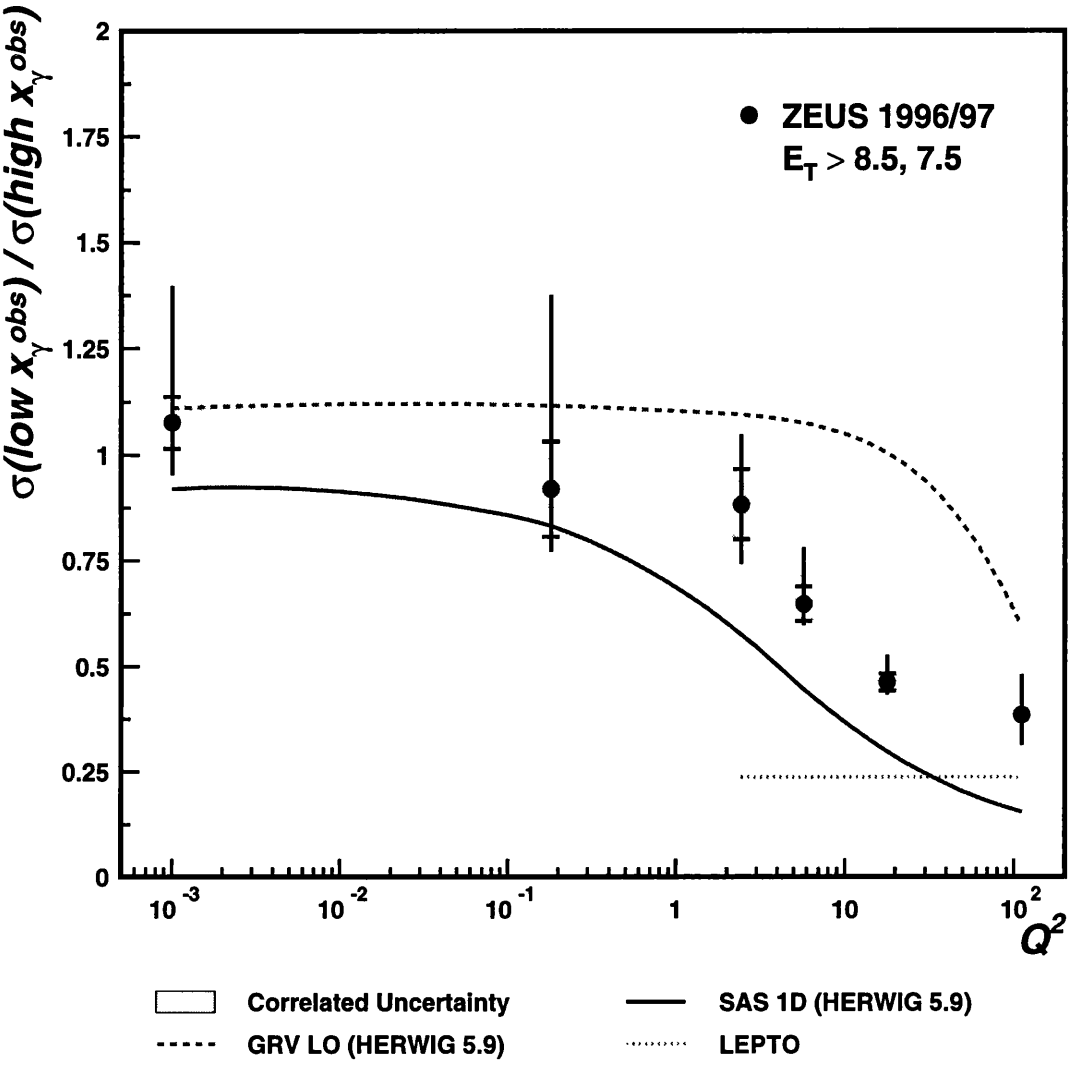

Figure 8.9: The ratio plot for the differential cross section $d\sigma/dx_\gamma^{obs}$ for $E_T^{jet} > 8.5, 7.5$ GeV. Q^2 is measured in units of GeV^2.

Again, it is the shape which is important, not the absolute normalisation of the theoretical models. The dependence of the shape with $(\overline{E_T^{cut}})^2$ is dependent upon the Q^2 region in question. The shapes of all the theoretical models are consistent with the shape of the data except for $Q^2 > 10.5$ GeV^2, where GRV LO has a steeper gradient than that of the data.

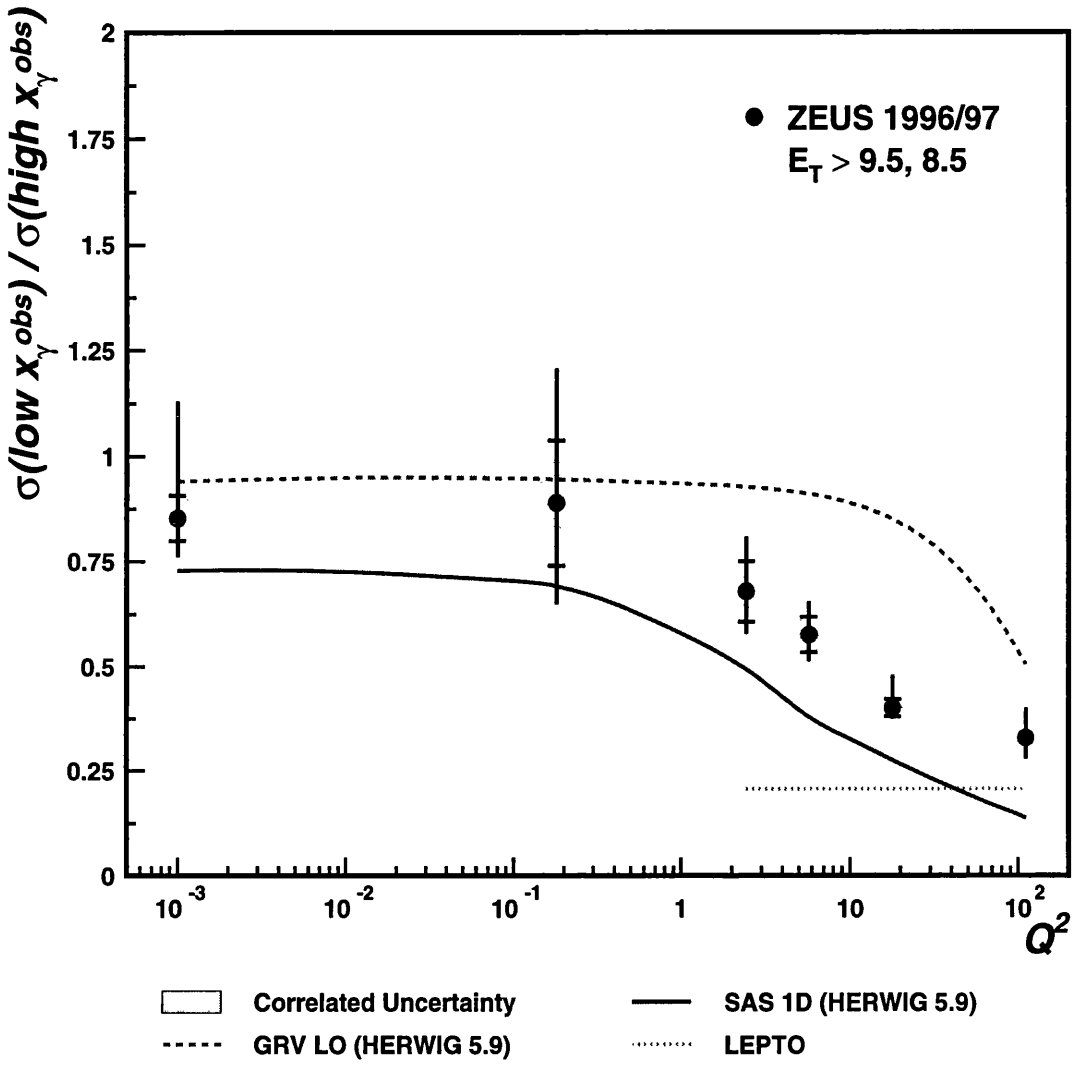

Figure 8.10: The ratio plot for the differential cross section $d\sigma/dx_\gamma^{obs}$ for $E_T^{jet} > 9.5, 8.5$ GeV. Q^2 is measured in units of GeV^2.

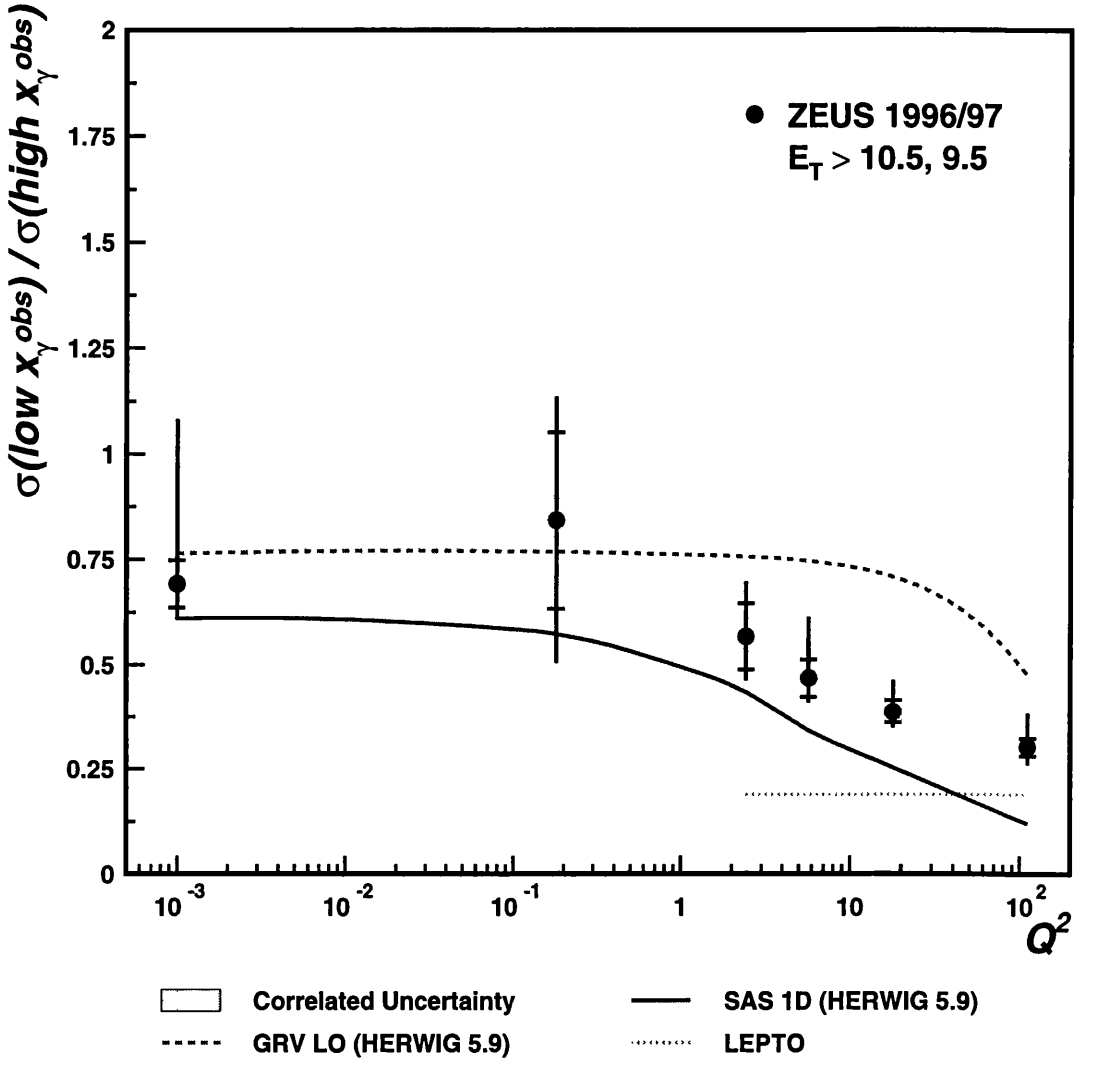

Figure 8.11: The ratio plot for the differential cross section $d\sigma/dx_\gamma^{obs}$ for $E_T^{jet} > 10.5, 9.5$ GeV. Q^2 is measured in units of GeV^2.

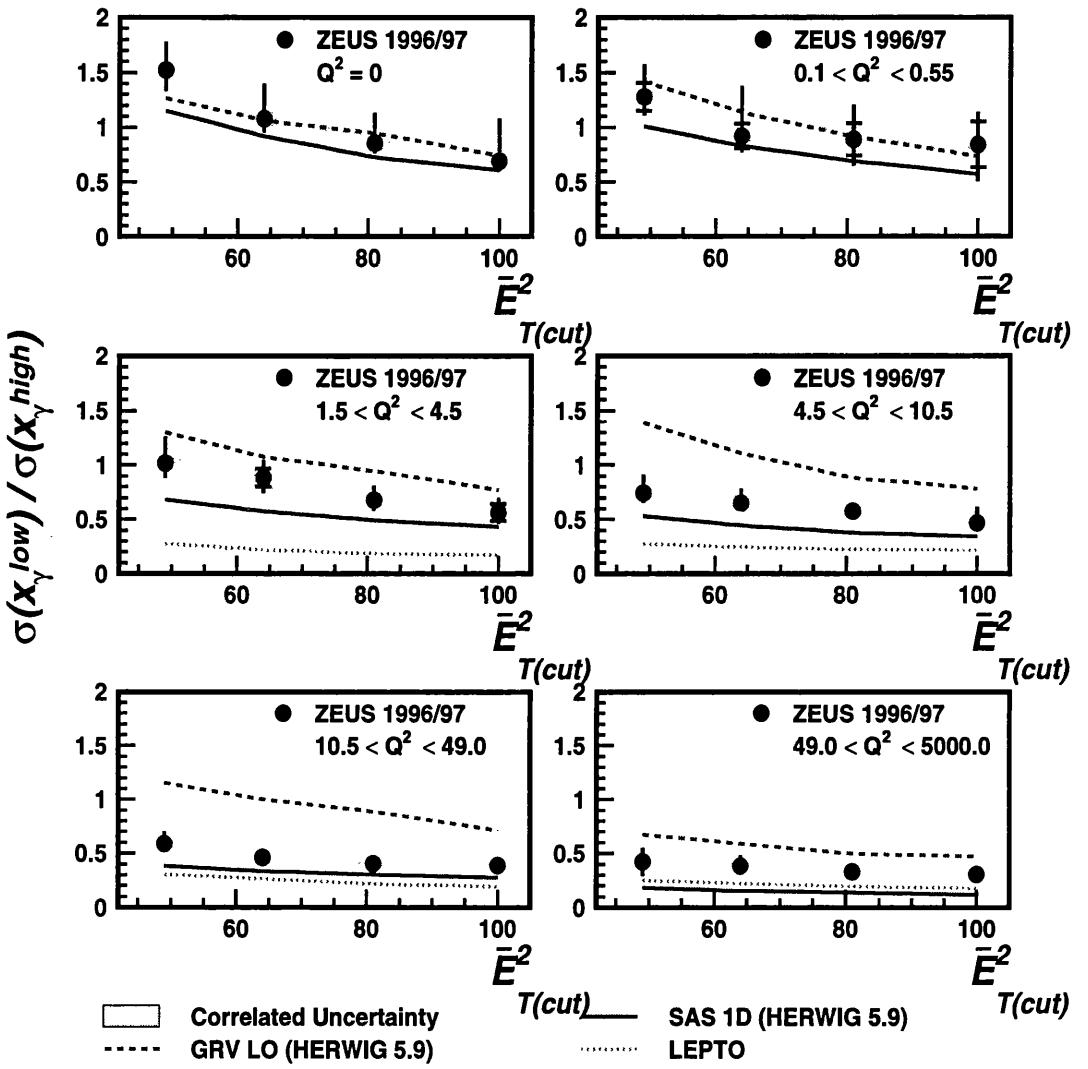

Figure 8.12: The ratio plot for the differential cross section $d\sigma/dx_\gamma^{obs}$ as a function of $(\overline{E_T^{cut}})^2$. Q^2 and $(\overline{E_T^{cut}})^2$ are measured in units of GeV^2.

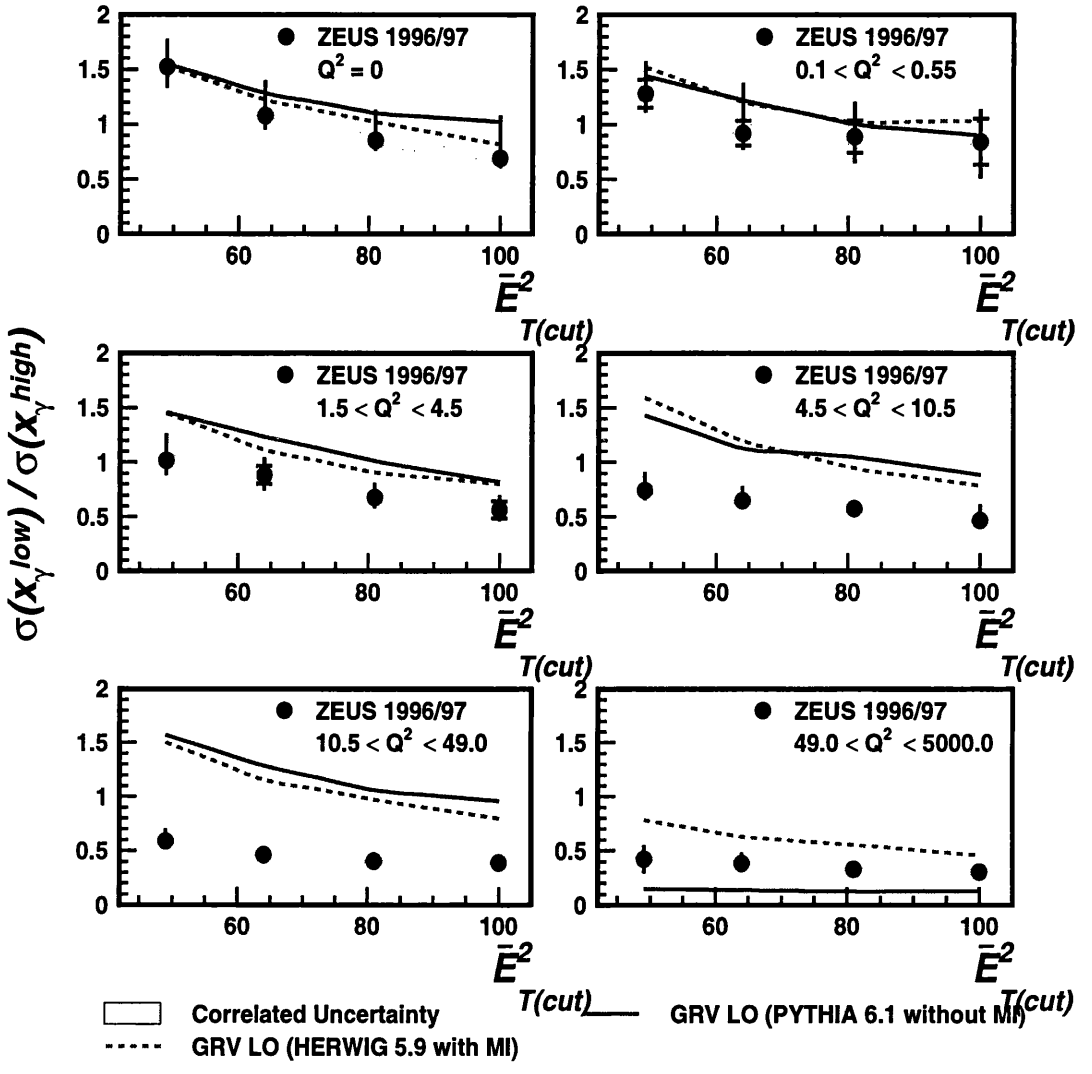

Figure 8.13: The ratio plot for the differential cross section $d\sigma/dx_\gamma^{obs}$ as a function of $(\overline{E_T^{cut}})^2$ with two other Monte Carlo models for comparison. Q^2 and $(\overline{E_T^{cut}})^2$ are measured in units of GeV^2.

Chapter 9

Summary

The photon is a boson and is said to be a pointlike object. At HERA, the scattering of photon and proton shows that the photon can behave like a hadronic object with structure, leading to a hard scatter and a photon remnant, just as the proton has a remnant. So the photon sometimes appears to have structure. The dijet events measured in ZEUS allow us to access information on this apparent structure. There are events where the whole photon enters the dijet system, and those where only part of the photon's momentum enters the dijet system. This is the defining picture.

To separate the two types of events, one depends on the topology of the final state. Using the variable x_γ^{obs} to determine whether the event is resolved or direct is a statement on the topology of the event, rather than on the structure of the photon, which becomes a matter of definition. The resolved photon can be viewed as an unknown sea of partons which have evolved from the initial fluctuation of the photon into a quark-antiquark pair, or as a set of Feynman diagrams which differ from direct diagrams in the transverse momentum separation of the partons which couple to the photon vertex. For this analysis, the procedure is well-defined in terms of x_γ^{obs}, and compared with theory in the same manner, so there is no ambiguity, despite theoretical models being developed in terms of a resolved photon which has structure, and a direct photon which is pointlike.

The partonic content of the virtual photon is expected to decrease with increasing virtuality. A number of theoretical models predict a decrease of the resolved photon contribution with respect to the direct [26, 51, 52], and this can clearly be seen in the ratio plot (figure 8.2) where the resolved contribution decreases with increasing Q^2. The H1 experiment have similar measurements [50] which concur with the measurements presented here. The reduction in the resolved-enriched component with increasing E_T^{jet} is at least partly due to kinematics. The same kinematical effects will apply to the Monte Carlo models, allowing the comparison of theory with data by comparing shapes. All PDFs give a reasonable shape comparison as a function of $(\overline{E_T^{cut}})^2$, except for the GRV LO PDF which disagrees in shape for $Q^2 > 10.5$ GeV^2.

The evolution of the virtual photon structure is towards more direct events with higher Q^2 and higher probing scale E_T. The presence of resolved events implemented in Monte Carlos is needed to describe the topology of the events which are produced by photon-proton scattering up to a Q^2 of at least 10.5 GeV^2. Models of photon structure are inadequately described by real photon PDFs and require PDFs which have a suppression of the resolved component with increasing Q^2.

The precision with which the scattered positron can now be measured makes possible a further study to complement this analysis. It would involve transforming the events to the photon-proton centre of mass frame. This is the frame in which theoretical cross section calculations are performed and the photon and proton are collinear. This means that the dijets should have similar transverse energies, unaffected by high Q^2 events which provide a transverse boost to the dijet system in the lab frame. The jet cuts enforced in the lab frame then correspond to non-uniform cuts in the centre of mass frame. In studying the effect of increasing the E_T of the dijets, it would be better to be independent of the transverse boost from the virtual photon, and hence transforming to such a frame would enable firmer conclusions to be drawn about

the structure of the virtual photon up to the highest Q^2. There is however a disadvantage in transforming to the photon-proton centre of mass frame. At ZEUS, photoproduction measurements are made using an anti-tag requirement, that the scattered positron is not detected in the main calorimeter. To transform to a different frame would require knowledge of the scattered positron's energy, which is not directly measured, but would have to be inferred from y_{JB}. The energy of the positron as derived from y_{JB} has such a large error as to make the Lorentz transformation not viable. The alternative is to make use of the luminosity monitor, which contains an electron calorimeter, and could access low enough photon virtualities for such a measurement, but at present requires further studies into the acceptance of this component. Hence, at present, the lab frame is then the best frame to use for measurements at lower photon virtualities, whereas the photon-proton centre of mass frame is better for higher photon virtualities.

Appendix A

Theory Reweighting Factors

The factors by which all the Monte Carlo theory curves are scaled in order to fit to the direct-enriched peak of the data are presented here in tabular form for different cuts on the jet transverse energies.

The samples are numbered from 1 to 5 as follows

1. HERWIG 5.9 with GRV LO photon PDF and no MIs simulated.
2. HERWIG 5.9 with SaS1D photon PDF and no MIs simulated.
3. LEPTO 6.5 direct process only Monte Carlo.
4. HERWIG 5.9 with GRV LO photon PDF with MIs simulated.
5. PYTHIA 6.1 with GRV LO photon PDF and no MIs simulated.

Reweighting Factors ($E_T > 7.5, 6.5$)					
Q^2 (GeV^2)	Sample 1	Sample 2	Sample 3	Sample 4	Sample 5
≈ 0	1.56	1.65	-	1.67	1.27
0.1 - 0.55	1.66	1.69	-	1.70	1.17
1.5 - 4.5	1.49	1.67	5.12	1.57	1.11
4.5 - 10.5	1.43	1.67	1.70	1.51	1.06
10.5 - 49.0	1.24	1.68	1.63	1.33	0.90
49.0 - 5000.0	9.30	1.43	1.34	0.92	0.29

Table A.1: The reweighting factors applied to the theory samples in order to match the direct-enriched peak in the data for jet transverse energy cuts at 7.5 and 6.5 GeV.

Reweighting Factors ($E_T > 8.5, 7.5$)					
Q^2 (GeV^2)	Sample 1	Sample 2	Sample 3	Sample 4	Sample 5
≈ 0	1.53	1.60	-	1.65	1.29
0.1 - 0.55	1.65	1.67	-	1.68	1.17
1.5 - 4.5	1.34	1.49	4.29	1.40	1.02
4.5 - 10.5	1.29	1.47	1.49	1.35	0.95
10.5 - 49.0	1.29	1.60	1.50	1.28	0.95
49.0 - 5000.0	1.05	1.33	1.26	1.02	0.34

Table A.2: The reweighting factors applied to the theory samples in order to match the direct-enriched peak in the data for jet transverse energy cuts at 8.5 and 7.5 GeV.

Reweighting Factors ($E_T > 9.5, 8.5$)					
Q^2 (GeV^2)	Sample 1	Sample 2	Sample 3	Sample 4	Sample 5
≈ 0	1.53	1.53	-	1.61	1.29
0.1 - 0.55	1.54	1.56	-	1.56	1.14
1.5 - 4.5	1.29	1.45	4.09	1.35	1.09
4.5 - 10.5	1.20	1.43	1.39	1.32	1.01
10.5 - 49.0	1.31	1.52	1.37	1.31	0.96
49.0 - 5000.0	1.08	1.29	1.21	1.11	0.41

Table A.3: The reweighting factors applied to the theory samples in order to match the direct-enriched peak in the data for jet transverse energy cuts at 9.5 and 8.5 GeV.

Reweighting Factors ($E_T > 10.5, 9.5$)					
Q^2 (GeV^2)	Sample 1	Sample 2	Sample 3	Sample 4	Sample 5
≈ 0	1.49	1.49	-	1.56	1.30
0.1 - 0.55	1.47	1.45	-	1.55	1.16
1.5 - 4.5	1.33	1.44	3.88	1.33	1.05
4.5 - 10.5	1.20	1.44	1.34	1.34	1.00
10.5 - 49.0	1.29	1.46	1.35	1.28	0.99
49.0 - 5000.0	1.10	1.26	1.18	1.12	0.50

Table A.4: The reweighting factors applied to the theory samples in order to match the direct-enriched peak in the data for jet transverse energy cuts at 10.5 and 9.5 GeV.

Appendix B

Tables of Data

The corrected measured differential cross sections together with their statistical and systematic errors are presented in tabular form below. The errors in column three are quoted as statistical $\oplus$ systematic, where $\oplus$ means addition in quadrature, and the systematic errors are the uncorrelated errors. The fourth column contains the statistical error only, and the fifth column contains the correlated systematic.

Differential Cross Sections for $Q^2 \approx 0$, $E_T > 7.5, 6.5$				
x_γ^{obs}	$d\sigma/dx_\gamma^{obs}$ (pb)	stat. $\oplus$ syst.	stat. only	corr. syst.
0.0625 - 0.25	5521.9	$^{+1493.0}_{-2366.6}$	$\pm$ 592.6	$^{+322.4}_{-899.2}$
0.25 - 0.50	7740.9	$^{+1784.9}_{-630.1}$	$\pm$ 444.1	$^{+370.1}_{-177.6}$
0.50 - 0.75	7555.6	$^{+1860.7}_{-623.0}$	$\pm$ 345.8	$^{+362.4}_{-162.8}$
0.75 - 1.00	13661.9	$^{+1177.6}_{-495.2}$	$\pm$ 344.8	$^{+272.2}_{-239.6}$

Table B.1: Table of corrected differential cross sections for $Q^2 \approx 0$ GeV^2 and $E_T > 7.5, 6.5$ GeV.

Differential Cross Sections for $0.1 < Q^2 < 0.55$, $E_T > 7.5, 6.5$				
x_γ^{obs}	$d\sigma/dx_\gamma^{obs}$ (pb)	stat. $\oplus$ syst.	stat. only	corr. syst.
0.0625 - 0.25	548.8	$^{+282.7}_{-181.8}$	$\pm$ 123.3	$^{+8.4}_{-40.3}$
0.25 - 0.50	568.4	$^{+191.8}_{-92.3}$	$\pm$ 68.6	$^{+23.2}_{-44.3}$
0.50 - 0.75	671.5	$^{+112.1}_{-67.6}$	$\pm$ 61.1	$^{+25.8}_{-19.1}$
0.75 - 1.00	1399.6	$^{+152.3}_{-75.8}$	$\pm$ 70.6	$^{+57.1}_{-20.8}$

Table B.2: Table of corrected differential cross sections for $0.1 < Q^2 < 0.55$ GeV^2 and $E_T > 7.5, 6.5$ GeV.

Differential Cross Sections for $1.5 < Q^2 < 4.5$, $E_T > 7.5, 6.5$				
x_γ^{obs}	$d\sigma/dx_\gamma^{obs}$ (pb)	stat. $\oplus$ syst.	stat. only	corr. syst.
0.0625 - 0.25	111.1	$^{+64.6}_{-28.0}$	$\pm$ 21.9	$^{+22.8}_{-4.1}$
0.25 - 0.50	259.9	$^{+50.4}_{-50.3}$	$\pm$ 26.0	$^{+14.0}_{-5.0}$
0.50 - 0.75	512.1	$^{+113.3}_{-60.3}$	$\pm$ 40.5	$^{+17.8}_{-66.4}$
0.75 - 1.00	868.6	$^{+158.6}_{-80.6}$	$\pm$ 32.3	$^{+38.2}_{-12.8}$

Table B.3: Table of corrected differential cross sections for $1.5 < Q^2 < 4.5$ GeV^2 and $E_T > 7.5, 6.5$ GeV.

Differential Cross Sections for $4.5 < Q^2 < 10.5$, $E_T > 7.5, 6.5$				
x_γ^{obs}	$d\sigma/dx_\gamma^{obs}$ (pb)	stat. $\oplus$ syst.	stat. only	corr. syst.
0.0625 - 0.25	47.3	$^{+27.3}_{-24.2}$	$\pm$ 6.8	$^{+3.9}_{-0.7}$
0.25 - 0.50	155.0	$^{+47.5}_{-11.6}$	$\pm$ 11.1	$^{+14.0}_{-2.3}$
0.50 - 0.75	276.2	$^{+46.5}_{-22.0}$	$\pm$ 14.4	$^{+20.1}_{-21.5}$
0.75 - 1.00	643.8	$^{+104.4}_{-63.5}$	$\pm$ 15.0	$^{+28.1}_{-25.5}$

Table B.4: Table of corrected differential cross sections for $4.5 < Q^2 < 10.5$ GeV^2 and $E_T > 7.5, 6.5$ GeV.

Differential Cross Sections for $10.5 < Q^2 < 49.0$, $E_T > 7.5, 6.5$				
x_γ^{obs}	$d\sigma/dx_\gamma^{obs}$ (pb)	stat. $\oplus$ syst.	stat. only	corr. syst.
0.0625 - 0.25	70.4	$^{+18.2}_{-17.2}$	$\pm$ 7.8	$^{+6.6}_{-11.2}$
0.25 - 0.50	183.9	$^{+31.0}_{-11.5}$	$\pm$ 9.9	$^{+6.5}_{-6.4}$
0.50 - 0.75	355.0	$^{+61.6}_{-18.8}$	$\pm$ 13.0	$^{+15.8}_{-13.9}$
0.75 - 1.00	1038.0	$^{+163.5}_{-48.5}$	$\pm$ 16.6	$^{+40.5}_{-36.1}$

Table B.5: Table of corrected differential cross sections for $10.5 < Q^2 < 49.0$ GeV^2 and $E_T > 7.5, 6.5$ GeV.

Differential Cross Sections for $49.0 < Q^2 < 5000.0$, $E_T > 7.5, 6.5$				
x_γ^{obs}	$d\sigma/dx_\gamma^{obs}$ (pb)	stat. $\oplus$ syst.	stat. only	corr. syst.
0.0625 - 0.25	25.9	$^{+42.7}_{-3.6}$	$\pm$ 3.5	$^{+0.5}_{-1.6}$
0.25 - 0.50	111.4	$^{+31.5}_{-23.2}$	$\pm$ 7.2	$^{+5.6}_{-5.1}$
0.50 - 0.75	295.6	$^{+77.5}_{-121.0}$	$\pm$ 12.1	$^{+8.1}_{-8.2}$
0.75 - 1.00	1020.4	$^{+204.0}_{-119.9}$	$\pm$ 16.1	$^{+15.9}_{-17.6}$

Table B.6: Table of corrected differential cross sections for $49.0 < Q^2 < 5000.0$ GeV^2 and $E_T > 7.5, 6.5$ GeV.

Differential Cross Sections for $Q^2 \approx 0$, $E_T > 8.5, 7.5$				
x_γ^{obs}	$d\sigma/dx_\gamma^{obs}$ (pb)	stat. $\oplus$ syst.	stat. only	corr. syst.
0.0625 - 0.25	1673.9	$^{+2012.6}_{-618.5}$	$\pm$ 260.4	$^{+435.7}_{-147.7}$
0.25 - 0.50	3896.1	$^{+1248.1}_{-768.0}$	$\pm$ 303.9	$^{+91.7}_{-212.7}$
0.50 - 0.75	4186.6	$^{+1310.7}_{-384.7}$	$\pm$ 245.2	$^{+260.3}_{-95.5}$
0.75 - 1.00	9063.5	$^{+975.4}_{-336.5}$	$\pm$ 277.0	$^{+191.2}_{-133.9}$

Table B.7: Table of corrected differential cross sections for $Q^2 \approx 0$ GeV^2 and $E_T > 8.5, 7.5$ GeV.

Differential Cross Sections for $0.1 < Q^2 < 0.55$, $E_T > 8.5, 7.5$				
x_γ^{obs}	$d\sigma/dx_\gamma^{obs}$ (pb)	stat. $\oplus$ syst.	stat. only	corr. syst.
0.0625 - 0.25	166.6	$^{+389.8}_{-57.6}$	$\pm$ 55.3	$^{+58.1}_{-12.0}$
0.25 - 0.50	308.1	$^{+158.0}_{-69.9}$	$\pm$ 53.7	$^{+25.9}_{-29.0}$
0.50 - 0.75	392.5	$^{+69.2}_{-80.3}$	$\pm$ 48.5	$^{+13.5}_{-6.7}$
0.75 - 1.00	942.8	$^{+64.4}_{-74.6}$	$\pm$ 58.9	$^{+14.4}_{-22.7}$

Table B.8: Table of corrected differential cross sections for $0.1 < Q^2 < 0.55$ GeV^2 and $E_T > 8.5, 7.5$ GeV.

Differential Cross Sections for $1.5 < Q^2 < 4.5$, $E_T > 8.5, 7.5$				
x_γ^{obs}	$d\sigma/dx_\gamma^{obs}$ (pb)	stat. $\oplus$ syst.	stat. only	corr. syst.
0.0625 - 0.25	50.0	$^{+26.3}_{-29.5}$	$\pm$ 15.5	$^{+6.5}_{-5.6}$
0.25 - 0.50	125.4	$^{+33.3}_{-23.6}$	$\pm$ 17.0	$^{+11.8}_{-13.8}$
0.50 - 0.75	294.3	$^{+43.0}_{-60.3}$	$\pm$ 31.0	$^{+4.5}_{-37.1}$
0.75 - 1.00	531.7	$^{+71.3}_{-25.5}$	$\pm$ 24.1	$^{+27.0}_{-7.9}$

Table B.9: Table of corrected differential cross sections for $1.5 < Q^2 < 4.5$ GeV^2 and $E_T > 8.5, 7.5$ GeV.

Differential Cross Sections for $4.5 < Q^2 < 10.5$, $E_T > 8.5, 7.5$				
x_γ^{obs}	$d\sigma/dx_\gamma^{obs}$ (pb)	stat. $\oplus$ syst.	stat. only	corr. syst.
0.0625 - 0.25	17.8	$^{+5.7}_{-6.9}$	$\pm$ 4.2	$^{+1.5}_{-1.3}$
0.25 - 0.50	84.9	$^{+31.0}_{-9.5}$	$\pm$ 8.4	$^{+14.3}_{-1.3}$
0.50 - 0.75	154.3	$^{+21.0}_{-13.8}$	$\pm$ 10.8	$^{+6.3}_{-2.3}$
0.75 - 1.00	396.5	$^{+56.3}_{-12.6}$	$\pm$ 11.2	$^{+16.6}_{-5.9}$

Table B.10: Table of corrected differential cross sections for $4.5 < Q^2 < 10.5$ GeV^2 and $E_T > 8.5, 7.5$ GeV.

Differential Cross Sections for $10.5 < Q^2 < 49.0$, $E_T > 8.5, 7.5$				
x_γ^{obs}	$d\sigma/dx_\gamma^{obs}$ (pb)	stat. $\oplus$ syst.	stat. only	corr. syst.
0.0625 - 0.25	28.4	$^{+7.7}_{-6.7}$	$\pm$ 4.7	$^{+1.8}_{-5.4}$
0.25 - 0.50	89.9	$^{+30.0}_{-7.5}$	$\pm$ 6.6	$^{+5.0}_{-3.6}$
0.50 - 0.75	193.4	$^{+24.0}_{-10.4}$	$\pm$ 9.4	$^{+10.4}_{-2.9}$
0.75 - 1.00	673.6	$^{+37.4}_{-29.8}$	$\pm$ 13.0	$^{+12.6}_{-14.5}$

Table B.11: Table of corrected differential cross sections for $10.5 < Q^2 < 49.0$ GeV^2 and $E_T > 8.5, 7.5$ GeV.

Differential Cross Sections for $49.0 < Q^2 < 5000.0$, $E_T > 8.5, 7.5$				
x_γ^{obs}	$d\sigma/dx_\gamma^{obs}$ (pb)	stat. $\oplus$ syst.	stat. only	corr. syst.
0.0625 - 0.25	13.2	$^{+23.9}_{-3.0}$	$\pm$ 2.5	$^{+0.2}_{-1.1}$
0.25 - 0.50	71.4	$^{+38.2}_{-14.8}$	$\pm$ 6.3	$^{+3.7}_{-1.1}$
0.50 - 0.75	181.6	$^{+36.1}_{-45.7}$	$\pm$ 9.4	$^{+6.1}_{-2.7}$
0.75 - 1.00	690.7	$^{+79.1}_{-32.5}$	$\pm$ 12.7	$^{+10.8}_{-10.4}$

Table B.12: Table of corrected differential cross sections for $49.0 < Q^2 < 5000.0$ GeV^2 and $E_T > 8.5, 7.5$ GeV.

Differential Cross Sections for $Q^2 \approx 0$, $E_T > 9.5, 8.5$				
x_γ^{obs}	$d\sigma/dx_\gamma^{obs}$ (pb)	stat. $\oplus$ syst.	stat. only	corr. syst.
0.0625 - 0.25	583.9	$^{+1092.6}_{-230.1}$	$\pm$ 112.4	$^{+186.3}_{-33.9}$
0.25 - 0.50	2129.2	$^{+804.5}_{-359.1}$	$\pm$ 192.4	$^{+105.8}_{-238.7}$
0.50 - 0.75	2589.3	$^{+911.3}_{-305.8}$	$\pm$ 175.6	$^{+114.7}_{-54.2}$
0.75 - 1.00	6213.7	$^{+605.0}_{-261.7}$	$\pm$ 213.4	$^{+94.6}_{-152.2}$

Table B.13: Table of corrected differential cross sections for $Q^2 \approx 0$ GeV^2 and $E_T > 9.5, 8.5$ GeV.

Differential Cross Sections for $0.1 < Q^2 < 0.55$, $E_T > 9.5, 8.5$				
x_γ^{obs}	$d\sigma/dx_\gamma^{obs}$ (pb)	stat. $\oplus$ syst.	stat. only	corr. syst.
0.0625 - 0.25	119.5	$^{+181.1}_{-98.4}$	$\pm$ 64.7	$^{+1.8}_{-48.0}$
0.25 - 0.50	220.5	$^{+53.7}_{-78.9}$	$\pm$ 45.0	$^{+47.6}_{-41.2}$
0.50 - 0.75	221.3	$^{+48.2}_{-48.3}$	$\pm$ 31.8	$^{+24.1}_{-7.8}$
0.75 - 1.00	631.4	$^{+52.0}_{-77.5}$	$\pm$ 44.1	$^{+37.4}_{-9.3}$

Table B.14: Table of corrected differential cross sections for $0.1 < Q^2 < 0.55$ GeV^2 and $E_T > 9.5, 8.5$ GeV.

Differential Cross Sections for $1.5 < Q^2 < 4.5$, $E_T > 9.5, 8.5$				
x_γ^{obs}	$d\sigma/dx_\gamma^{obs}$ (pb)	stat. $\oplus$ syst.	stat. only	corr. syst.
0.0625 - 0.25	21.6	$^{+15.7}_{-14.8}$	$\pm$ 7.2	$^{+4.0}_{-0.3}$
0.25 - 0.50	63.4	$^{+24.0}_{-13.9}$	$\pm$ 9.9	$^{+3.7}_{-6.2}$
0.50 - 0.75	162.9	$^{+27.7}_{-26.1}$	$\pm$ 19.7	$^{+2.5}_{-10.3}$
0.75 - 1.00	365.2	$^{+38.3}_{-23.1}$	$\pm$ 18.2	$^{+12.9}_{-5.4}$

Table B.15: Table of corrected differential cross sections for $1.5 < Q^2 < 4.5$ GeV^2 and $E_T > 9.5, 8.5$ GeV.

Differential Cross Sections for $4.5 < Q^2 < 10.5$, $E_T > 9.5, 8.5$				
x_γ^{obs}	$d\sigma/dx_\gamma^{obs}$ (pb)	stat. $\oplus$ syst.	stat. only	corr. syst.
0.0625 - 0.25	8.7	$^{+3.2}_{-4.5}$	$\pm$ 2.6	$^{+0.2}_{-0.7}$
0.25 - 0.50	50.2	$^{+9.3}_{-9.5}$	$\pm$ 6.3	$^{+0.8}_{-2.5}$
0.50 - 0.75	97.3	$^{+11.7}_{-12.5}$	$\pm$ 8.0	$^{+2.1}_{-5.9}$
0.75 - 1.00	271.3	$^{+25.4}_{-9.8}$	$\pm$ 8.4	$^{+10.3}_{-4.0}$

Table B.16: Table of corrected differential cross sections for $4.5 < Q^2 < 10.5$ GeV^2 and $E_T > 9.5, 8.5$ GeV.

Differential Cross Sections for $10.5 < Q^2 < 49.0$, $E_T > 9.5, 8.5$				
x_γ^{obs}	$d\sigma/dx_\gamma^{obs}$ (pb)	stat. $\oplus$ syst.	stat. only	corr. syst.
0.0625 - 0.25	11.5	$^{+5.3}_{-2.5}$	$\pm$ 2.4	$^{+2.1}_{-0.2}$
0.25 - 0.50	51.2	$^{+24.8}_{-4.6}$	$\pm$ 4.5	$^{+3.1}_{-0.8}$
0.50 - 0.75	118.2	$^{+18.3}_{-8.0}$	$\pm$ 6.8	$^{+3.4}_{-1.7}$
0.75 - 1.00	451.1	$^{+41.6}_{-17.0}$	$\pm$ 9.5	$^{+9.9}_{-7.6}$

Table B.17: Table of corrected differential cross sections for $10.5 < Q^2 < 49.0$ GeV^2 and $E_T > 9.5, 8.5$ GeV.

Differential Cross Sections for $49.0 < Q^2 < 5000.0$, $E_T > 9.5, 8.5$				
x_γ^{obs}	$d\sigma/dx_\gamma^{obs}$ (pb)	stat. $\oplus$ syst.	stat. only	corr. syst.
0.0625 - 0.25	5.1	$^{+19.4}_{-1.2}$	$\pm$ 1.2	$^{+0.9}_{-0.1}$
0.25 - 0.50	42.7	$^{+20.2}_{-8.9}$	$\pm$ 4.4	$^{+3.5}_{-0.6}$
0.50 - 0.75	113.5	$^{+19.1}_{-22.1}$	$\pm$ 6.8	$^{+3.0}_{-4.2}$
0.75 - 1.00	491.4	$^{+34.0}_{-12.4}$	$\pm$ 9.7	$^{+8.3}_{-7.3}$

Table B.18: Table of corrected differential cross sections for $49.0 < Q^2 < 5000.0$ GeV^2 and $E_T > 9.5, 8.5$ GeV.

Differential Cross Sections for $Q^2 \approx 0$, $E_T > 10.5, 9.5$				
x_γ^{obs}	$d\sigma/dx_\gamma^{obs}$ (pb)	stat. $\oplus$ syst.	stat. only	corr. syst.
0.0625 - 0.25	203.7	$^{+1288.9}_{-58.1}$	$\pm$ 58.1	$^{+75.7}_{-3.0}$
0.25 - 0.50	1266.5	$^{+748.9}_{-206.8}$	$\pm$ 153.2	$^{+32.1}_{-18.7}$
0.50 - 0.75	1581.6	$^{+789.9}_{-183.0}$	$\pm$ 135.6	$^{+131.4}_{-77.0}$
0.75 - 1.00	4408.2	$^{+451.8}_{-352.9}$	$\pm$ 179.3	$^{+84.1}_{-78.5}$

Table B.19: Table of corrected differential cross sections for $Q^2 \approx 0$ GeV^2 and $E_T > 10.5, 9.5$ GeV.

Differential Cross Sections for $0.1 < Q^2 < 0.55$, $E_T > 10.5, 9.5$				
x_γ^{obs}	$d\sigma/dx_\gamma^{obs}$ (pb)	stat. $\oplus$ syst.	stat. only	corr. syst.
0.0625 - 0.25	97.2	$^{+76.5}_{-110.0}$	$\pm$ 71.6	$^{+17.1}_{-1.4}$
0.25 - 0.50	130.5	$^{+85.9}_{-44.8}$	$\pm$ 36.2	$^{+17.6}_{-6.5}$
0.50 - 0.75	134.8	$^{+32.8}_{-46.7}$	$\pm$ 25.9	$^{+2.1}_{-13.0}$
0.75 - 1.00	430.2	$^{+46.2}_{-81.5}$	$\pm$ 37.0	$^{+8.0}_{-6.5}$

Table B.20: Table of corrected differential cross sections for $0.1 < Q^2 < 0.55$ GeV^2 and $E_T > 10.5, 9.5$ GeV.

Differential Cross Sections for $1.5 < Q^2 < 4.5$, $E_T > 10.5, 9.5$				
x_γ^{obs}	$d\sigma/dx_\gamma^{obs}$ (pb)	stat. $\oplus$ syst.	stat. only	corr. syst.
0.0625 - 0.25	10.2	$^{+14.3}_{-5.8}$	$\pm$ 5.1	$^{+1.0}_{-0.6}$
0.25 - 0.50	38.6	$^{+18.4}_{-11.0}$	$\pm$ 8.2	$^{+7.6}_{-0.6}$
0.50 - 0.75	96.1	$^{+18.1}_{-20.6}$	$\pm$ 15.5	$^{+2.4}_{-7.9}$
0.75 - 1.00	255.7	$^{+27.2}_{-20.0}$	$\pm$ 15.3	$^{+14.4}_{-3.8}$

Table B.21: Table of corrected differential cross sections for $1.5 < Q^2 < 4.5$ GeV^2 and $E_T > 10.5, 9.5$ GeV.

Differential Cross Sections for $4.5 < Q^2 < 10.5$, $E_T > 10.5, 9.5$				
x_γ^{obs}	$d\sigma/dx_\gamma^{obs}$ (pb)	stat. $\oplus$ syst.	stat. only	corr. syst.
0.0625 - 0.25	5.6	$^{+8.1}_{-5.0}$	$\pm$ 2.6	$^{+15.6}_{-1.0}$
0.25 - 0.50	26.3	$^{+18.3}_{-4.3}$	$\pm$ 4.2	$^{+3.7}_{-0.4}$
0.50 - 0.75	57.6	$^{+18.9}_{-6.4}$	$\pm$ 6.1	$^{+2.6}_{-0.9}$
0.75 - 1.00	191.5	$^{+10.7}_{-13.8}$	$\pm$ 7.2	$^{+5.7}_{-3.1}$

Table B.22: Table of corrected differential cross sections for $4.5 < Q^2 < 10.5$ GeV^2 and $E_T > 10.5, 9.5$ GeV.

Differential Cross Sections for $10.5 < Q^2 < 49.0$, $E_T > 10.5, 9.5$				
x_γ^{obs}	$d\sigma/dx_\gamma^{obs}$ (pb)	stat. $\oplus$ syst.	stat. only	corr. syst.
0.0625 - 0.25	7.1	$^{+13.4}_{-2.5}$	$\pm$ 2.2	$^{+3.5}_{-0.6}$
0.25 - 0.50	34.2	$^{+11.6}_{-5.5}$	$\pm$ 4.0	$^{+0.6}_{-1.9}$
0.50 - 0.75	79.8	$^{+11.0}_{-9.5}$	$\pm$ 6.0	$^{+1.3}_{-3.4}$
0.75 - 1.00	312.5	$^{+28.4}_{-8.4}$	$\pm$ 7.9	$^{+6.7}_{-5.9}$

Table B.23: Table of corrected differential cross sections for $10.5 < Q^2 < 49.0$ GeV^2 and $E_T > 10.5, 9.5$ GeV.

Differential Cross Sections for $49.0 < Q^2 < 5000.0$, $E_T > 10.5, 9.5$				
x_γ^{obs}	$d\sigma/dx_\gamma^{obs}$ (pb)	stat. $\oplus$ syst.	stat. only	corr. syst.
0.0625 - 0.25	2.5	$^{+22.1}_{-1.1}$	$\pm$ 0.9	$^{+1.2}_{-0.0}$
0.25 - 0.50	30.3	$^{+12.1}_{-6.3}$	$\pm$ 3.9	$^{+0.6}_{-1.1}$
0.50 - 0.75	76.1	$^{+9.4}_{-13.3}$	$\pm$ 5.9	$^{+4.1}_{-3.2}$
0.75 - 1.00	359.6	$^{+38.0}_{-10.2}$	$\pm$ 8.3	$^{+5.5}_{-6.6}$

Table B.24: Table of corrected differential cross sections for $49.0 < Q^2 < 5000.0$ GeV^2 and $E_T > 10.5, 9.5$ GeV.

Appendix C

Contribution to the DIS '99 Conference

The results presented here include measurements of the structure of both the real and the virtual photon, although the author's input has been mainly concerned with the virtual photon results. This contribution has now been published in Nuclear Physics B (Proc. Suppl.) 79 (1999) 505-507.

Structure of Real and Virtual Photons from ZEUS

N. Macdonald[a]

[a] Dept. of Physics and Astronomy, University of Glasgow, Glasgow, U.K.

Measurements sensitive to the structure of both real and virtual photons are presented and compared to theoretical models with various photon parton distribution functions (PDFs). Measurements for real photons show a tendency for the available photon PDFs to be too small to describe the data. For virtual photons, the photon PDF is seen to decrease with increasing photon virtuality.

In order to describe the data, resolved photon processes are required up to a photon virtuality of at least 4.5 GeV^2.

C.1 Introduction

Experimental information on the partonic structure of the photon can be obtained from the data taken at the HERA ep collider experiments. Leading order (LO) QCD predicts that photon interactions have a two-component nature. In direct photon processes the entire momentum of the photon takes part in the hard subprocess with a parton from the proton whereas in resolved photon processes the photon acts as a source of partons and one of these enters the hard subprocess. By measuring inclusive dijet events (two or more jets) information on the structure of the real photon can be extracted. By also measuring the scattered electron, information can be obtained on the evolution of this structure as a function of the virtuality of the photon, Q^2.

The fraction of the photon's four momentum which enters the hard subprocess at leading order, denoted by x_γ^{LO}, is equal to unity for direct processes, and less than unity for resolved processes. Experimentally it is not possible to measure x_γ^{LO} directly. Instead, an observable quantity x_γ^{obs} is defined which is calculable and well-defined to all orders of perturbation theory. x_γ^{obs} is the fraction of the photon momentum manifest in the two highest transverse energy jets and is defined by the equation

$$x_\gamma^{obs} = \frac{\sum E_{Tj} e^{-\eta_j}}{2E_e y}$$

where E_{Tj} is the transverse energy of jet j, η_j is the pseudorapidity of the jet measured in the lab frame, and y is the inelasticity of the event.

"Direct enriched" events are defined as being those with $x_\gamma^{obs} > 0.75$ and "resolved enriched" events as those with $x_\gamma^{obs} < 0.75$. This value gives the optimal separation of the leading order direct and resolved event classes.

C.2 Dijets in Photoproduction and Real Photon Structure

The kinematic selection cuts made in order to examine the structure of the real photon are

- Two or more jets (k_T clustering algorithm)
- $Q^2 \simeq 0$ GeV^2
- $E_{T\ leading}^{jet} > 14$ GeV, $E_{T\ second}^{jet} > 11$ GeV
- $-1 < \eta^{jet} < 2$
- $0.20 < y < 0.85$

The advantages of using high E_T dijets are that they provide a hard scale where perturbative QCD (pQCD) is expected to work, the hadronisation corrections are small, and the effect of underlying events is small. Given these assumptions, the data can be compared directly to NLO pQCD calculations without the need to simulate some hadronisation model. This analysis concentrates on the high x_γ^{obs} region where the quark densities in the photon are not strongly constrained by e^+e^- experiments.

The measured ZEUS data is compared to NLO pQCD calculations for three photon PDFs, GRV-HO [57], AFG-HO [59] and GS96-HO [58]. The NLO calculations have been performed by three groups of theorists, Harris et al. [54], Klasen et al. [55] and Frixione et al. [56]. Since the agreement between the calculations is excellent only one of the calculations is plotted.

Figure C.1 shows the differential dijet cross section as a function of $E_{T\ leading}^{jet}$ for $0.20 < y < 0.85$. There is an excess in the data above theory for central jets ($0 < \eta^{jet} < 1$) below an E_T of 25 GeV. The assumption that the hadronisation corrections are negligible is not true for backward jets ($-1 < \eta^{jet} < 0$), so no

conclusions are drawn about the backward region, rather the discrepancy between data and theory is ascribed to a theoretical uncertainty.

Figure C.2 shows the cross section for a narrower range in y. This provides a better sensitivity to the photon structure since the cross section is no longer averaged over the broader y range. There is an excess in the data seen for central ($0 < \eta^{jet} < 1$) and forward ($1 < \eta^{jet} < 2$) jets, both for the whole x_γ^{obs} range and the high x_γ^{obs} range.

The excess in the data above theory for jets with $E_T < 25$ GeV and for central and forward rapidities suggests that the available photon PDF parametrisations, based on e^+e^- F_2^γ data, are too small in this kinematic regime.

C.3 Ratio of Dijet Cross Sections vs Q^2

The kinematic selection cuts made for the analysis of virtual photons are

- Two or more jets (k_T clustering algorithm)
- $Q^2 \simeq 0$, $0.1 < Q^2 < 0.55$, $1.5 < Q^2 < 4.5$ (GeV^2)
- $0.20 < y < 0.55$
- $E_T^{jets} > 5.5$ GeV
- $-1.125 < \eta^{jets} < 2.2$

Three different Q^2 regions are available for measurement. $Q^2 \simeq 1.0$ GeV^2 corresponds to quasi-real photons, where the electron is not measured, and the large bulk of such events lead to a median Q^2 of 0.001 GeV^2. ZEUS has a small angle electron detector for tagging events in the transition region between photoproduction and DIS ($0.1 < Q^2 < 0.55$ GeV^2). For $1.5 < Q^2 < 4.5$ GeV^2 the electron is detected in the ZEUS main calorimeter.

Figure C.3 shows the ratio of the resolved to the direct dijet cross sections as a function of Q^2. Since some of the systematic uncertainties cancel in the ratio,

this is a more precise measurement than an absolute differential cross section. The data fall with increasing Q^2. This is compared to the dijet ratio obtained with HERWIG 5.9 [43] using a photon PDF which does not evolve with Q^2 (GRV LO [47]) and one which does (SaS1D [26]). The HERWIG ratio with GRV LO is flat, while that obtained with SaS 1D falls with increasing Q^2. Therefore the fall of the ratio with Q^2 observed in the data indicates that the data require a virtual photon PDF which evolves with photon virtuality. The LEPTO 6.5.1 [53] curve shows the prediction for leading order direct processes in DIS only. Note that this ratio is non-zero as may be understood given that LEPTO contains higher-order processes in the approximation of parton-showering and hadronization. The data approach this direct only limit, however resolved processes are still required in order to describe the data up to at least $Q^2 = 4.5$ GeV^2.

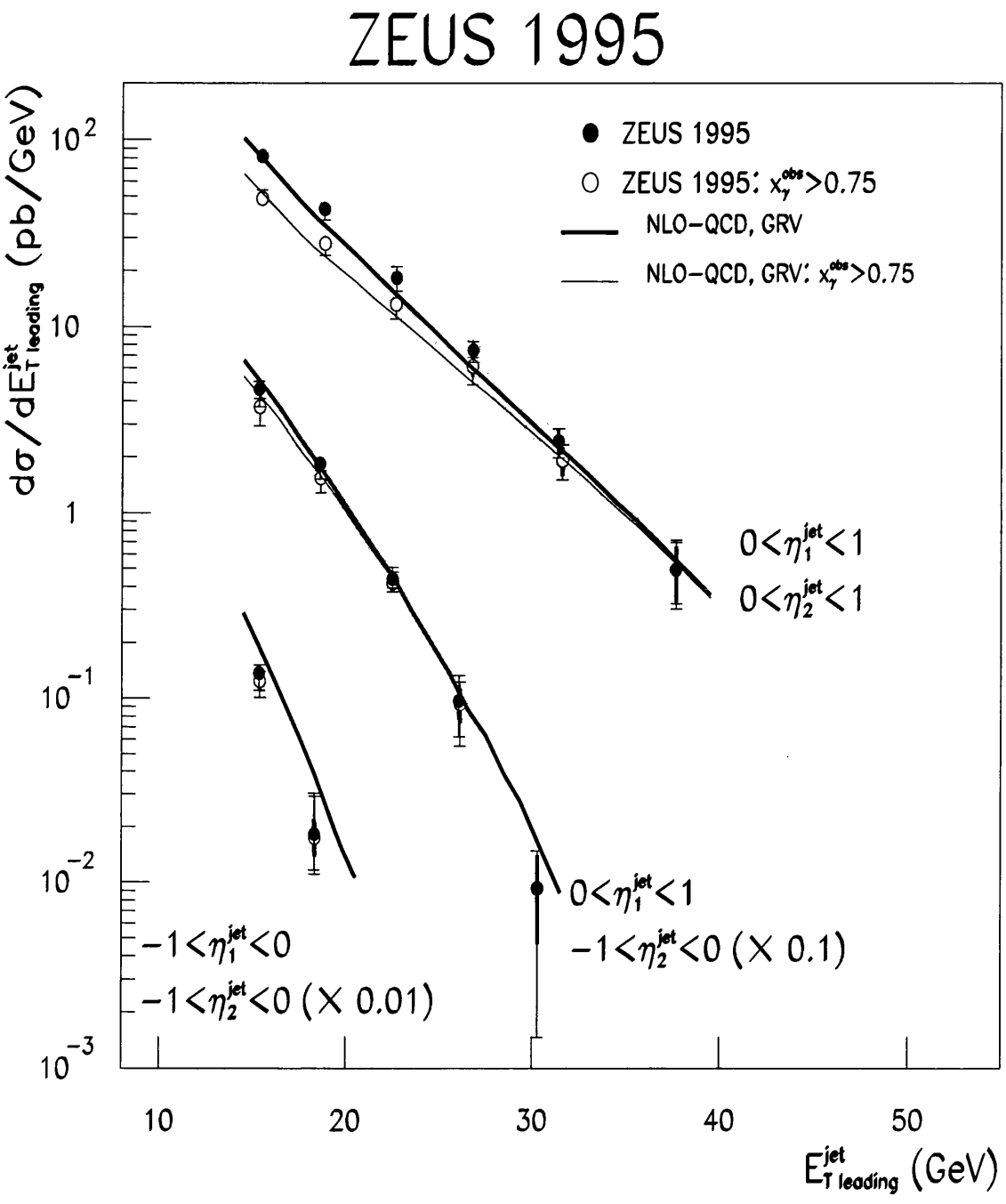

Figure C.1: Differential dijet cross section as a function of $E_{T\ leading}^{jet}$ for 0.20 $< y <$ 0.85.

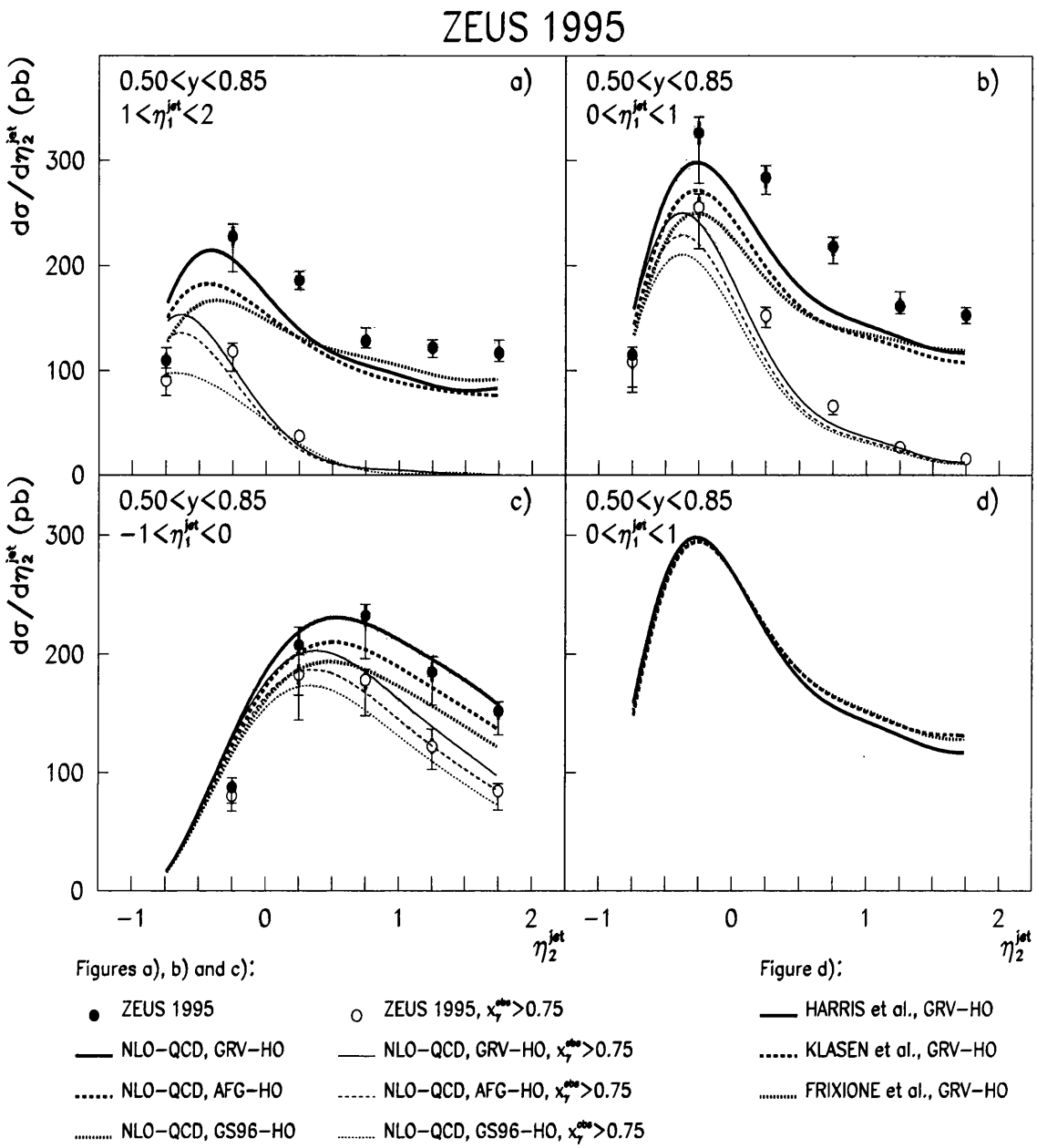

Figure C.2: Differential dijet cross section as a function of η_2^{jet} in bins of η_1^{jet} for $0.50 < y < 0.85$.

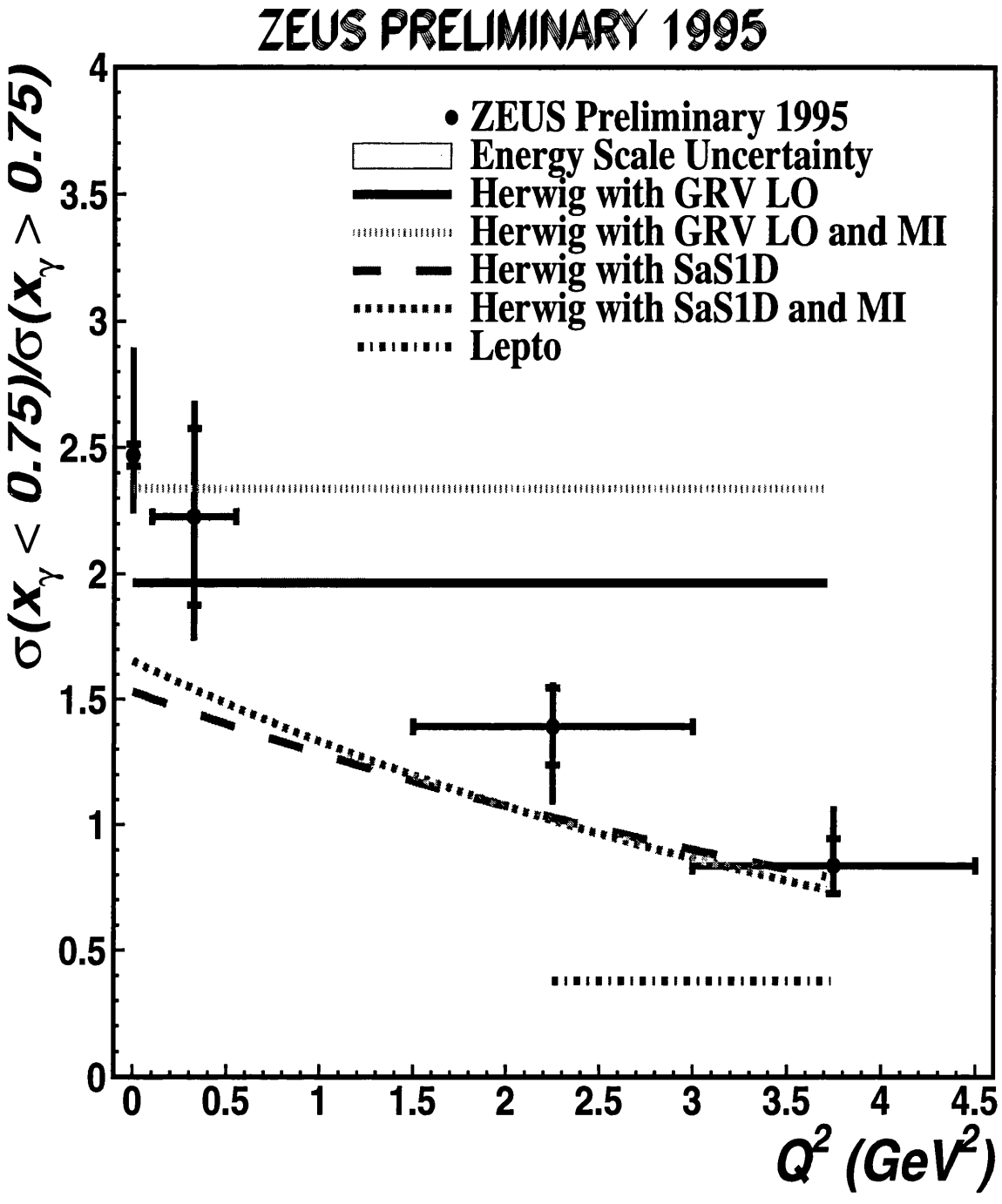

Figure C.3: Ratio of resolved enriched to direct enriched dijet cross sections vs Q^2

Bibliography

[1] F. Halzen & A. Martin, *"Quarks & Leptons"*, John Wiley & Sons, 1984.

[2] ZEUS Collaboration, *Phys. Rev. Lett.* **75** (1995) 1006.

[3] S. Weinberg, *Phys. Rev. Lett.* **19** (1967) 1264;
S. L. Glashow, *Nucl. Phys.* **22** (1961) 579;
A. Salam, "Weak and electromagnetic interactions", Proceedings of the Nobel Symposium held in 1968, 1968.

[4] Yu. L. Dokshitzer, D. I. D'Yakonov and S. I. Troyan, *Phys. Rep.* **C58** (1980) 271.

[5] H. D. Politzer, *Phys. Rev. Lett.* **30** (1973) 1346;
D. J. Gross and F. Wilczek, *Phys. Rev.* **D8** (1973) 3633.

[6] E. D. Bloom et al., *Phys. Rev. Lett.* **23** (1969) 930;
M. Breidenbach et al., *Phys. Rev. Lett.* **23** (1969) 935.

[7] R. P. Feynman, *Phys. Rev. Lett.* **23** (1969) 1415.

[8] M. Gell-Mann, *Phys. Lett.* **8** (1964) 214;
G. Zweig, CERN-8192/TH 401 (1964);
G. Zweig, CERN-8192/TH 412 (1964).

[9] R. Brandelik et al., *Phys. Lett.* **B97** (1980) 453;
S. L. Wu., *Phys. Rep.* **107** (1984) 59.

[10] B. R. Martin, G. Shaw, "Particle Physics", Wiley 1992.

[11] H1 Collab., T. Ahmed et al., *Phys. Lett.* **B297** (1992) 205;
ZEUS Collab., M. Derrick et al., *Phys. Lett.* **B297** (1992) 404.

[12] C. F. Weizsäcker, *Zeits. f. Phys.* **88** 612;
E. J. Williams, Proc. Roy. Soc. London **A139** (1933) 163;
E. J. Williams, *Phys. Rev.* **45** (1934) 729.

[13] B. Burow, "A Measurement of the Total Photon-Proton Cross Section in the Centre of Mass Range 167 to 194 GeV", DESY F35D-94-01.

[14] P. J. Bussey, *Phys. Lett.* **B382** (1996) 426.

[15] J. J. Sakurai and D. Schildknecht, *Phys. Lett.* **B41** (1972) 489.

[16] L. Feld, Ph.D. thesis BONN-IR-96-17, Bonn University, December 1996.

[17] A. Levy, *Phys. Lett.* **B404** (1997) 369.

[18] R. J. DeWitt, L. M. Jones, J. D. Sullivan, D. E. Willen and H. W. Wyld Jr, *Phys. Rev.* **D19** (1979) 2046.

[19] A. Martin, *Cont. Phys.* **36** (1995) 335.

[20] C. G. Callan and D. G. Gross, *Phys. Rev. Lett.* **22** (1969) 156.

[21] J. D. Bjorken, Proceedings of the Enrico Fermi International School of Physics, ed. J. Steinberger, Course XLI, 1968.

[22] T. Eichten et al., *Phys. Lett.* **B46** (1973) 274.

[23] V. N. Gribov and L. N. Lipatov, *Sov. J. Nucl. Phys.* **15** (1972) 438;
L. N. Lipatov, *Sov. J. Nucl. Phys.* **20** (1975) 96;
Yu. L. Dokshitzer, *Sov. Phys. JETP* **46** (1977) 641;
G. Altarelli and G. Parisi, *Nucl. Phys.* **126** (1977) 298.

[24] H. Abramowicz et al., *Int. J. Mod. Phys.* **A8** (1993) 1005.

[25] ZEUS Collab., M. Derrick et al., *Phys. Lett.* **B342** (1995) 417;
ZEUS Collab., M. Derrick et al., *Phys. Lett.* **B348** (1995) 665;
H1 Collab., T. Ahmed et al., *Z. Phys.* **C70** (1996) 17.

[26] G. Schuler and T. Sjöstrand, *Phys. Lett.* **B376** (1996) 193.

[27] PLUTO Collab., Ch. Berger et al., *Phys. Lett.* **B142** (1984) 119.

[28] L3 Collab., M. Acciarri et al., *Phys. Lett.* **B436** (1998) 403.

[29] OPAL Collab., K. Ackerstaff et al., *Phys. Lett.* **B411** (1997) 387.

[30] ZEUS Collab., "ZEUS Detector Status Report 1993", DESY, 1993.

[31] H. Bethe and W. Heitler, Proc. Roy. Soc., **A146** (1934) 83.

[32] S. Catani, Yu. L. Dokshitzer and B. R. Webber, *Phys. Lett.* **B285** (1992) 291.

[33] J. M. Butterworth, L. Feld and R. L. Saunders, "Measurement of Dijet Cross Sections in Photoproduction at HERA", ZEUS Note 97-057.

[34] J. Huth et al., Proc. of the 1990 DPF Summer Study on High Energy Physics, Snowmass, Colorado, edited by E. L. Berger (World Scientific Singapore, 1992) p.134.

[35] S. D. Ellis and D. E. Soper, *Phys. Rev.* **D48** (1993) 3160.

[36] S. Catani, Yu. L. Dokshitzer, M. H. Seymour and B. R. Webber, *Nucl. Phys.* **B406** (1993) 187.

[37] A. Savin, "Study of Calorimeter Noise in the 1996 Data", ZEUS Note 98-07.

[38] J. Repond, "Jet Energy Corrections", ZEUS Note 96-133.

[39] H. Abramowicz, A. Caldwell and R. Sinkus, "Neural Network Based Electron Identification in the ZEUS calorimeter", DESY 95-054.
R. Sinkus, *Nucl. Instrum. Methods* **A361** (1995) 290.

[40] A. Quadt, Ph.D. Thesis, University of Oxford (1998).

[41] B. W. Harris and J. F. Owens, *Phys. Rev.* **D56** (1997) 4007.

[42] GEANT 3.13, R. Brun, CERN DD/EE/84-1 (1987).

[43] G. Marchesini, B. R. Webber, I. G. Knowles, M. H. Seymour and L. Stanco, *Computer Phys. Commun.* **67** (1992) 465.

[44] T. Sjöstrand, *Computer Phys. Commun.* **82** (1994) 74.

[45] J. M. Butterworth, J. R. Forshaw and M. H. Seymour, *Z. Phys.* **C72** (1996) 637.

[46] A. Martin et al., *Phys. Rev.* **D50** (1994) 6734.

[47] M. Glück, E. Reya and A. Vogt, *Phys. Rev.* **D46** (1992) 1973.

[48] C. Glasman, Ph.D. Thesis, Weizmann Institute of Science (1995).

[49] K. Charchula, G. A. Schuler and H. Spiesberger, *Computer Phys. Commun.* **81** (1994) 381.

[50] H1 Collab., C. Adloff et al., "Measurement of Dijet Cross-Sections at Low Q^2 and the Extraction of an Effective Parton Density for the Virtual Photon", DESY 98-205 (1998), submitted to Eur. Phys. J. C.

[51] M. Drees and R. Godbole, *Phys. Rev.* **D50** (1994) 3124.

[52] M. Gluck, E. Reya and M. Stratmann, *Phys. Rev.* **D54** (1996) 5515.

[53] G.Ingelman, A. Edin and J. Rathsman, *Computer Phys. Commun.* **101** (1997) 108-134.

[54] B.W. Harris and J.F. Owens, *Phys. Rev.* **D56** (1997) 4007.

[55] M. Klasen and G. Kramer, *Z. Phys* **C76** (1997) 67;
M. Klasen, T. Kleinwort and G. Kramer, *Eur. Phys. J.* **C1** (1998) 1.

[56] S. Frixione and G. Ridolfi, *Nucl. Phys.* **B507** (1997) 315;
S. Frixione, *Nucl. Phys.* **B507** (1997) 295.

[57] M. Glück, E. Reya and A. Vogt,*Phys. Rev.* **D45** (1992) 3986.

[58] L.E. Gordon and J.K. Storrow, *Nucl. Phys.* **B489** (1997) 405.

[59] P. Aurenche, J. Guillet and M. Fontannaz, *Z. Phys* **C64** (1994) 621.